分类号__________ 密级__________

U D C__________ 编号__________

华中师范大学

博 士 学 位 论 文

相对论重离子碰撞中的间歇分析

学位申请人姓名: 吴锦

申请学位学生类别: 全日制博士

申请学位学科专业: 粒子物理与原子核物理

指 导 教 师 姓 名: 吴元芳 教授

罗晓峰 教授

李治明 副教授

忠诚博雅，朴实刚毅

博士学位论文

论文题目：相对论重离子碰撞中的间歇分析

论文作者：吴锦

指导教师：吴元芳, 罗晓峰, 李治明

学科专业：粒子物理与原子核物理

研究方向：相对论重离子碰撞

华中师范大学物理科学与技术学院

2023 年 6 月

Dissertation

Intermittency Analysis in Relativistic Heavy Ion Collisions

By

Jin Wu

Supervisor: Yuanfang Wu, Xiaofeng Luo, Zhiming Li

Specialty: Particle Physics and Nuclear Physics

Research Area: Physics of Relativistic Heavy Ion Collision

College of Physical Science and Technology

Central China Normal University

June, 2023

华中师范大学学位论文原创性声明和使用授权说明

原创性声明

本人郑重声明：所呈交的学位论文，是本人在导师指导下，独立进行研究工作所取得的研究成果。除文中已经标明引用的内容外，本论文不包含任何其他个人或集体已经发表或撰写过的研究成果。对本文的研究做出贡献的个人和集体，均已在文中以明确方式标明。本声明的法律结果由本人承担。

作者签名： 日期：2023 年 6 月 日

学位论文版权使用授权书

学位论文作者完全了解华中师范大学有关保留、使用学位论文的规定，即：研究生在校攻读学位期间论文工作的知识产权单位属华中师范大学。学校有权保留并向国家有关部门或机构送交论文的复印件和电子版，允许学位论文被查阅和借阅；学校可以公布学位论文的全部或部分内容，可以允许采用影印、缩印或其它复制手段保存、汇编学位论文。（保密的学位论文在解密后遵守此规定）保密论文注释：本学位论文属于保密，在______ 年解密后适用本授权书。非保密论文注释：本学位论文不属于保密范围，适用本授权书。

作者签名： 导师签名：

日期：2023 年 6 月 日 日期：2023 年 6 月 日

本人已经认真阅读“CALIS 高校学位论文全文数据库发布章程”，同意将本人的学位论文提交“CALIS 高校学位论文全文数据库”中全文发布，并可按“章程”中的规定享受相关权益。同意论文提交后滞后：□半年；□一年；□二年发布。

作者签名： 导师签名：

日期：2023 年 6 月 日 日期：2023 年 6 月 日

Abstract

Quantum Chromodynamics (QCD), the fundamental theory that governs strong interaction, has predicted the existence of the Quark-Gluon Plasma (QGP). The QGP is a state of the strongly interacting matter in which quarks and gluons are no longer confined to volumes of hadron. Experiments at the Relativistic Heavy Ion Collider (RHIC) and Large Hadron Collider (LHC), have provided evidences for the creation of QGP matter in the early 21st century. Since the discovery of the QGP, physicists have been investigating the phase transition between hadronic phase and QGP phase, and the corresponding QCD phase diagram which can be mapped and displayed into a two dimensional plane of temperature (T) versus baryon chemical potential (μ_B). Lattice QCD calculations predicted a crossover transition from hadronic matter to QGP at vanishing μ_B. At large μ_B, QCD-based model calculations suggested that the phase transition is of the first-order. One essential feature of the QCD phase diagram is the critical point (CP), where the first-order phase transition boundary terminates. Nowadays, many researches worldwide are working towards finding the the possible CP in heavy-ion collisions, especially the Beam Energy Scan (BES) program at the RHIC-STAR.

Within the framework of intermittency analysis, a search for critical density fluctuations is ongoing to locate the possible CP in the QCD phase diagram. Based on the Ising-QCD calculations, the density-density function has a power-law, or self-similar, structure which gives rise to large density fluctuations in heavy-ion collisions. Such fluctuations can be probed via an intermittency analysis by utilizing the scaled factorial moments (SFMs). The intermittency termed as big bursts from small region (cells) of the phase space, appears as a power-law (scal-

ing) behavior of SFMs. The strength of intermittency can be quantified by the intermittency index (ϕ_q) extracted from the power-law behavior of SFMs on the number of partitioned cells (M), and by the scaling exponents (ν) obtained from the power-law behavior of higher-order SFMs on the second-order one. Over the last decade, the NA49 and and the NA61/SHINE experiments have been searching for the critical point by performing intermittency analysis in heavy-ion reactions of various sizes and collision energies. Meanwhile, various models have investigated the intermittency under various fundamental mechanisms in heavy-ion collisions, such as the UrQMD (ultra-relativistic quantum molecular dynamics) model with hadronic potentials.

In this thesis, we present the first measurement of intermittency in heavy-ion collisions at RHIC, and show the collision energy and centrality dependence of SFMs and intermittency exponents for identified charged hadrons in Au+Au collisions from the STAR experiment. The data presented here have been obtained from Au+Au collisions at $\sqrt{s_{\mathrm{NN}}}$ = 7.7, 11.5, 14.5, 19.6, 27, 39, 54.4, 62.4, and 200 GeV, recorded by the Solenoidal Tracker at RHIC (STAR) experiment from 2010 to 2017. These energies correspond to baryon chemical potential ranging from 20 to 420 MeV at chemical freeze-out in the QCD phase diagram. The mixed event method is applied to eliminate background contributions, and the cell-by-cell method is proposed to the application of efficiency corrections on SFMs. The SFMS of identified charged hadrons are analyzed at mid-rapidity and within the transverse momentum phase space, and can be calculated up to the sixth order with the range of number of cells $M^2 = 1 - 100^2$. We observe a power-law behavior of scaled factorial moments in Au+Au collisions and a decrease in the extracted scaling exponent (ν) from peripheral to central collisions. The ν is consistent with a constant for different collisions energies in the mid-central (10-40%) collisions. Moreover, the ν in the 0-5% most central Au+Au collisions exhibits a non-monotonic energy dependence that reaches a possible minimum around $\sqrt{s_{\mathrm{NN}}}$ = 27 GeV. The non-monotonic energy dependence of ν agrees with those from other several measurements, such as, the net-proton kurtosis, the slope of directed flow for net-proton, and the ratio of light nuclei production.

We use the cascade UrQMD model to estimate the contributions from non-critical fluctua-

tions on SFMs and intermittency exponents. It is found that the power-law behavior is not valid when the background contributions are subtracted, in the original UrQMD model. Moreover, a Critical Monte Carlo (CMC) model which can simulate critical intermittency driven by density fluctuations, is used to study the property of intermittency in heavy-ion collisions. Critical fluctuations from the CMC model have been incorporated into the UrQMD model to describe and understand the intermittency measured in experiments. By comparing the UrQMD+CMC model results with those from the STAR data, it is found that the value of a calculated scaling exponent falls in the range of the experimental measurement when 1-2 % signal of intermittency fluctuations is added into the UrQMD sample.

The thesis is organized as follows. Chapter 1 is an introduction of the QCD phase diagram and the critical point, and the framework of intermittency analysis. In chapter 2, we describe the methods of background subtraction and efficiency correction for the experimental analysis. We shortly introduce the STAR experiment at RHIC in chapter 3. The analysis detail of the STAR data is given in chapter 4. The results from the STAR data are discussed in chapter 5. In chapter 6, we show the result of intermittency from the UrQMD, CMC, and hybrid UrQMD+CMC models, respectively. Finally, a summary and outlook is given in chapter 7.

Keywords: QCD phase diagram, Critical point, Relativistic heavy-ion collision, Intermittency, Scaled factorial moment, Scaling exponent.

摘　要

量子色动力学 (Quantum Chromodynamics，QCD) 是描述夸克/胶子之间强相互作用的基本理论。QCD 理论预言, 在高温和高密度条件下，夸克和胶子将摆脱强相互作用力的束缚，解除禁闭，形成由自由夸克和胶子组成的新物质形态——夸克胶子等离子体（QGP）。现代物理学认为 QGP 广泛存在于宇宙的最早期，之后由于宇宙的膨胀和冷却而消失了。在现今的世界中，科学家预期通过相对论重离子碰撞实验来产生 QGP。21 世纪初，BNL 相对论重离子对撞机（RHIC）和 CERN 大型强子对撞机（LHC）实验，都已经发现了 QGP 物质存在的信号。随后，科学家一直在探索 QGP 新物质到普通强子物质的相变及其相结构。强相互作用物质的相图（QCD 相图），通常用温度（T）与重子化学势（μ_B）的二维图来描述，重离子碰撞实验中的能量点可以一一对应到相图中。基于第一性原理出发的格点 QCD 理论表明，在低重子化学势和高温度时，QGP 相和强子物质相的转变是一种平滑的过渡。基于 QCD 理论的模型预测，在高重子化学势和低温度时，QGP 相到强子相的转变属于一级相变。在 QCD 相图上，一级相变边界的终结点为 QCD 临界点。当前，在全球范围内，多个重大科学实验都在研究 QCD 相结构和寻找可能存在的 QCD 临界点，特别是 RHIC-STAR 能量扫描实验。

理论上认为，重离子碰撞系统在接近或者处于临界点时，将会出现很强的密度涨落。我们可以通过寻找和研究重离子碰撞产生的密度涨落来确定 QCD 临界点的位置，间歇分析是寻找和观察密度涨落的一种方法。基于三维 Ising-QCD 的理论计算，碰撞系统处于临界状态时，体系的密度分布函数具有一种幂律，或者自相似的结构，这使得动量空间里出现很强的密度涨落。这种密度涨落表现为间歇现象，即在相空间中的小区域（单元）内，物质的密度分布出现较大的起伏。实验上，我们可以用阶乘矩（Scaled

Factorial Moment，SFM）来测量碰撞系统产生的密度涨落，即它的表现形式——间歇。如果碰撞系统存在着间歇，系统的阶乘矩将表现出幂律行为，或者标度行为。间歇的强度大小通过间歇指数 (ϕ_q)，或者标度指数 (ν) 来表示。间歇指数可以通过计算 SFM 和对相空间所分割的格子数（M）的标度关系得到，标度指数则可以通过计算高阶 SFMs 和二阶 SFM 的标度关系来得到。2010 年以来，位于 CERN 的 NA49 和 NA61/SHINE 合作组已经开展了不同能量以及不同种类的重离子碰撞实验，通过间歇分析来寻找 QCD 临界点。同时，模型方面的分析也已经开展，比如，当把强子势机制加入到 UrQMD（超相对论量子动力学）模型后，该模型的 Ar+Sc 体系表现出间歇行为。

在本篇论文中，我们首次测量了 RHIC 重离子碰撞实验中的间歇。我们通过分析 RHIC-STAR 实验中的 Au+Au 数据，计算不同碰撞能量下的带电强子的阶乘矩，得到阶乘矩和标度指数的能量依赖，以及中心度依赖。从 2010 到 2017 年，RHIC-STAR 实验已经采集第一期 Au+Au 对撞的实验数据。这些实验数据的对撞质心能量点（$\sqrt{s_{\rm NN}}$）有九个，分别是 7.7，11.5，14.5，19.6，27，39，54.4，62.4 和 200 GeV。这九个能量点对应到 QCD 相图中的重子化学式（μ_B）范围为 20 到 420 MeV。实验数据主要由 STAR 实验中的时间投影室和飞行时间探测器记录。在分析中，我们采用混合事件（mixed event）方法消除背景对观测量的影响。同时，对于阶乘矩的效率修正，我们提出并采用了逐格子（cell-by-cell) 的方法。我们计算了横动量空间（p_x, p_y）中，中心快度区间（$|\eta| < 0.5$）的带电强子的阶乘矩。在目前的事件统计量下，阶乘矩的阶数（q）可以计算到六阶（$q = 2-6$），格式数（M）可以计算到 100 ($M = 1-100$)。我们发现，扣除背景后的阶乘矩随着格子数的增大而增大，并且高阶的 SFMs 和二阶的 SFM 之间满足标度行为。通过分析阶乘矩的标度行为，我们得到标度指数的中心度和能量依赖。研究发现，从边缘碰撞到中心碰撞，标度指数在逐渐变小。在最中心 Au+Au 碰撞（0-5%）中，标度指数表现出非单调的能量依赖，并且在 $\sqrt{s_{\rm NN}}$ = 27 GeV 左右可能存在最小值。目前，其它观察量也表现出非单调的能量依赖，比如净质子数的峰度（$\kappa\sigma^2$）和直接流（v_1），轻核的产额比（$N_t \times N_p/N_d^2$），标度指数的结果类似于这些观测量的结果。

我们通过强子输运 UrQMD 模型，研究非临界现象所引起的涨落对阶乘矩和间歇指数的影响。对于所有能量和中心度，UrMQD 模型的阶乘矩和对应混合事件的阶乘矩，这二者的大小基本一致。当扣除来自背景的贡献后，阶乘矩的数值基本为零，阶乘矩

的标度行为不再存在，即 UrQMD 模型不表现出任何与间歇有关的标度行为。由于临界蒙特卡洛（CMC）模型可以模拟具有临界涨落的动量分布，我们用它来研究间歇的自相似性质，以及间歇指数和相对密度涨落系数之间的关系。为了解释 STAR 实验中观察到的间歇，我们将 CMC 模型产生的临界涨落加入到 UrQMD 模型中。通过比较 UrQMD+CMC 模型的结果和 STAR 实验数据的结果，我们发现当 UrQMD 事件样本加入 CMC 模型中的 1-2％临界涨落信号时，UrQMD+CMC 模型的标度指数和 STAR 实验测量得到的，在数值范围内相符合。

本论文结构如下：第一章介绍 QCD 相图和临界点，以及介绍重离子碰撞中的间歇和观测量。第二章介绍实验分析中用来背景扣除和效率修正的方法。在第三章中，我们简要介绍 RHIC-STAR 实验, 以及 TPC 和 TOF 探测器。第四章给出 STAR 实验数据的具体分析步骤和细节。在第五章中, 我们讨论 STAR 实验中间歇分析的结果。第六章展示来自模型的间歇分析的结果，包括 UrQMD、CMC 和 UrQMD+CMC 模型的结果。最后的章节是本文的总结和展望。

关键词：QCD 相图、临界点、相对论重离子碰撞、间歇、阶乘矩、标度指数

Contents

Chapter 1

Introduction

1.1 Quantum Chromodynamics

What is the universe made of and how it works? This has always been a fundamental interest of science. Nowadays, the best theory to describe the most basic building blocks of the universe, is the Standard Model [1, 2, 3, 4] which explains how elementary particles make up all known matter and how they interact. It encompasses three of the four fundamental forces in nature: the strong force, the weak force, the electromagnetic force. The strong force binds quarks together to form protons and neutrons, and also binds protons and neutrons together inside atomic nuclei. Quantum chromodynamics is the quantum field theory that describes the strong interactions [5, 6, 7]. The QCD was developed by Harald Fritzsch and Heinrich Leutwyler, together with Murray Gell-Mannover over a brief period from 1972-1973 [5, 6].

A quark is a fundamental constituent of matter and there are six types of quark fields of varying masses in QCD [5, 6, 8]. They are known as three light quarks: up (u), down (d) and strange (s), as well as three heavy quarks: charm (c), top (t) and bottom (b). In analogue to photon, the carrier of the electromagnetic force between two charged particle, gluon is the carrier for the strong force between quarks. Gluons bind quarks together to form hadrons, e.g, proton and neutron. Color, a new quantum number, was introduced to label the states of quark (anti-quark) which allowed allows two otherwise identical quarks to exist in the same particle. In QCD, colors can be transformed by the color group $SU(3)_C$, and have three values: red, greed and blue, provided that a quark's color can only take any one of three values.

The QCD has two salient features: asymptotic freedom and color confinement.

1.1.1 Asymptotic Freedom

The nuclear force is not a constant, but varies with the distance between the quarks. The force between quarks, or strong force, becomes vanishingly small at short distance, while enhances at large distances. Equivalently, the force becomes weak and quark become a free particle at high-energy scales. This property is called the asymptotic freedom [6, 9, 9, 10], discovered by David Gross and Frank Wilczek [9], as well as independently by David Politzer in 1973 [11].

The coupling constant, or gauge coupling parameter, is a number that determines the strength of the force exerted in an interaction. In QCD, the coupling constant of strong interaction, α_s, is introduced by a scale parameter Λ [6, 12]:

$$\alpha_s(Q^2) = \frac{g_s^2(Q)}{4\pi} \approx \frac{4\pi}{(11 - \frac{2}{3}n_f)ln(\frac{Q^2}{\Lambda^2})} \tag{1.1}$$

where Q is the energy scale, n_f is the number of the different quark flavors. The value of $\Lambda = (133 \pm 17)$ MeV measured by experiments [6, 12]. Eq. 1.1 reveals that strong coupling constant decreases with increasing energy scale, and the strong force becomes smaller at large energy scale accordingly.

The scale dependence of the coupling constant has measured by many experiments. Figure 1.1 shows the experimental measurements of the coupling constant as a function of the energy scale. The solid line represent the QCD prediction, and different marks shows the values from experimental data. For α_s, its clearly seen that experimental data agreed very well with theoretical prediction.

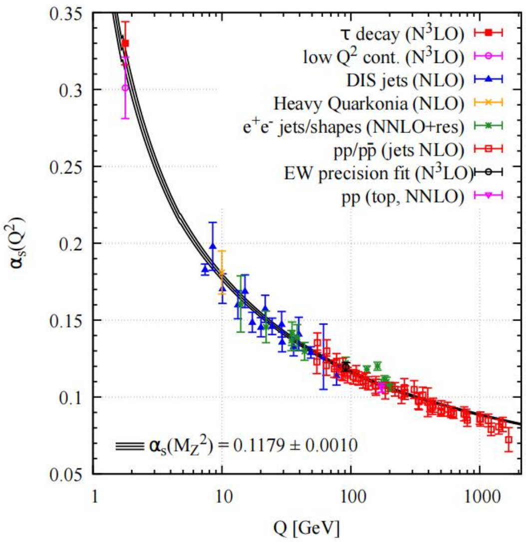

Figure 1.1: Summary of measurements of the coupling constant (α_s) as a function of the energy scale (Q). Figure taken from Ref. [12].

1.1.2 Color Confinement

Electrons can move around freely and be separated from the atom, and hadrons also can be isolated. However, unlike electrons and hadrons, quarks and gluons cannot be separated macroscopically from hadron and cannot be directly observed in isolation. Color confinement is defined as that objects with color charge, e.g, quarks and gluons, do not exist as independent physical objects in the QCD vacuum [6]. In quark potential model, quarks are point-like and confined inside hadron by a binding potential $V_0(r)$ defined as follows [6, 13]:

$$V_0(r) \sim \sigma r, \tag{1.2}$$

where r is the separation distance between quarks, and σ is the string tension that measures the energy per unit separation distance. Eq. (1.2) indicates that an infinite amount of energy would be needed to isolate a quark. However, at sufficiently high density, or high energy scale, the color charge is expected to become screened, and the binding potential will become as [13]:

$$V(r) \simeq \sigma r[\frac{1-exp(-ur)}{ur}] \tag{1.3}$$

where $u = r^{-1}$ is the color screening mass. Figure 1.2 shows the $V(r)$ as a function of the r according to Eq. (1.3). Its shown that $V(r)$ increase with increasing at first but saturates at a finite value, for the case $u \neq 0$. As the energy density of the nuclear substance becomes sufficiently high, color deconfinement will occur, leading to quarks and gluons become de-confined and can move freely in a larger volume than the size of hadron.

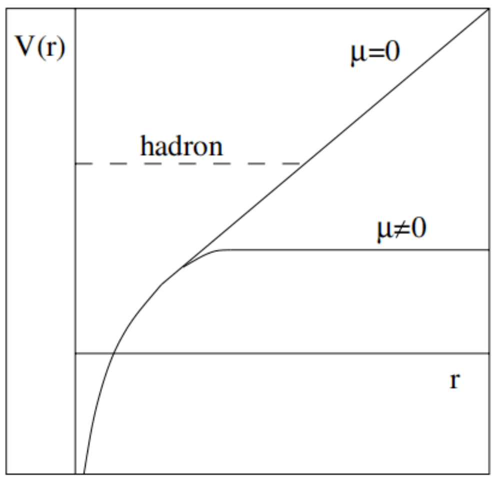

Figure 1.2: The binding potential, $V(r)$, as a function of the separation distance, r. Figure taken from Ref. [13].

1.2 Quark-Gluon Plasma (QGP)

The normal world we live in, is at low densities and temperatures where quark and gluons are confined to the size of hadrons. However, as a consequence of de-confined quarks and gluons when temperatures or densities become very high, quarks and gluons will become free and transform themselves into a new phase of matter, called 'quark–gluon plasma' (QGP) [14]. Its believed that 10 picoseconds after the Big Bang the early universe was filled with incredibly hot quark-gluon plasma [14, 15], as shown in Fig. 1.3. Since the beginning of the century, physicist have been able to recreate QGP experimentally by colliding heavy atomic nuclei (called heavy ions as in an accelerator atoms are ionized) at relativistic energy [16, 17, 18, 19, 20]. At CERN Large Hadron Collider (LHC) and BNL Relativistic Heavy Ion Collider (RHIC), lead and gold nuclei were accelerated to ultrarelativistic speeds and directed towards each other (Au+Au and Pb+Pb). In these heavy-ion collisions, the hundreds of protons and neutrons in two collider nuclei smash into one another at high energies. Such collisions will create a "fireball" called "Litte Bang", in which neutrons, protons and other hadrons melt into QGP. Striking evidences for the existence of QGP have been collected by high-energy experiments at RHIC and LHC. These include the suppression of non-prompt J/ψ [19, 20], strong collective flow [18, 21], jet quenching [18, 22], enhanced strangeness production [23, 24] and so on.

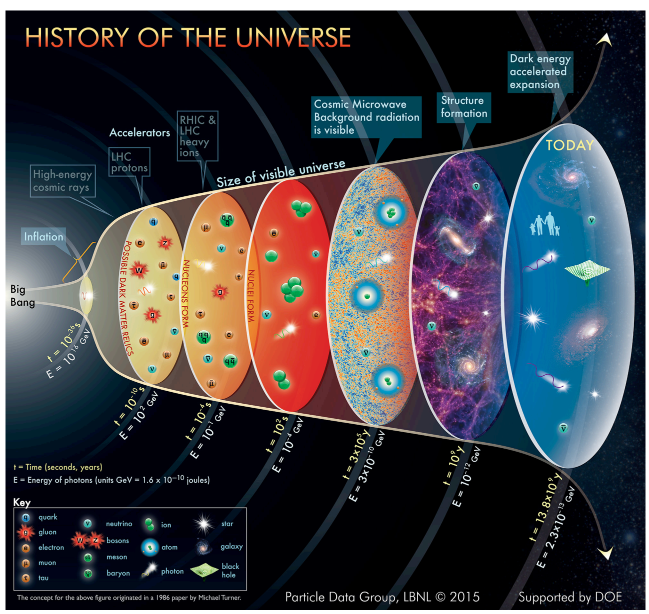

Figure 1.3: Artist's conception of the evolution of the Big Bang. Figure taken from Ref. [25].

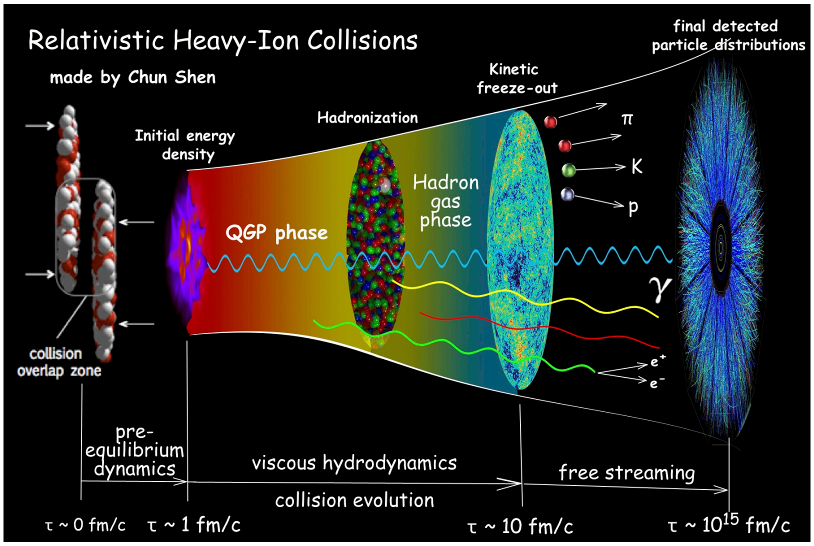

Figure 1.4: The space time evolution of Little Bangs in relativistic heavy-ion collisions. Figure taken from Ref. [26].

Figure 1.4 schematically depicts the evolution process of high energy nucleus-nucleus collision (Little Bangs) in relativistic heavy-ion collisions. At first, two coming nuclei consisting a large number of protons and neutrons, moved in opposite directions and traveled at 99.995% the speed of light. These two nuclei looked flat as a pancake due to the Lorentz contraction along the beam direction. Then they collided and smashed through each other, creating a fireball when the collision energy is high enough [14, 27]. At this moment, quark and gluon were not long confined inside the hadron and moved free in a limited volume, leading to the creation of QGP in the laboratory. Consequently, the collision was very quick and lasting around 10^{-25} s [14]. The resulting QGP matter instantly expanded and cooled over the next few 10^{-24} s, and quarks and gluons recombined to form a hadron gas, called hadronization. Then, hadron gas underwent the chemical freeze-out when the inelastic scatterings ceased and particle yields got fixed, followed by kinetic freeze-out when elastic scattering stopped and the particle momentum spectra were frozen. At last, produced particles flew out from the collision space and moved towards detectors. The information of particles, such as momentum and mass, will be recorded by the detectors.

1.3 QCD Phase Transition and the Critical Point (CP)

In nature world, matter can occur in various states, or phases. What we know best is the different phases of water (solid, liquid and gas). Fig. 1.5 shows the phase diagram of water which identifies the physical state of a sample of water under specified conditions of pressure (P) and temperature (T). In Fig. 1.5, a pressure of 50 kPa and a temperature of -10 $^{\circ}C$ correspond to the region of the diagram labeled "ice". And a pressure of 50 kPa and a temperature of 50 $^{\circ}C$ correspond to the "water". In addition, at $P = 25$ kPa and $T = 200$ $^{\circ}C$, water exists only in the gaseous state. Its important note that there is a critical point which is the end of first-order transition between the liquid and gas phases, when $P = 22089$ kPa and $T = 374$ $^{\circ}C$. Above the critical point, there is no distinct change from the liquid phase to the vapor phase. The physical properties of water change dramatically near the critical point, such as divergence of the specific head (C_v) and correlation length ξ.

The QCD theory suggested a phase transition from the ordinary nuclear mater, which consists of hadrons inside which quarks and gluons are confined, to the QGP, a state of matter in which quarks and gluons are no longer confined inside hadron. In analogue to the phase transition of water, a obvious question for the QCD matter arise that what is the phase structure of this matter if it exhibits different phases under different circumstance? Indeed, with the discovery of the QGP at the RHIC [16, 17, 18], physicist have been investigating the phase structure of the QCD matter over the last two decades.

1.3.1 QCD Phase Diagram and the QCD Critical Point

By tuning the collision energies in heavy-ion collisions, the phase diagram of QCD can be mapped and displayed into a two dimensional plane of temperature (T) versus baryon chemical potential (μ_b) [30, 31, 32, 33]. Figure 1.6 shows the QCD phase diagram in the two-dimensional

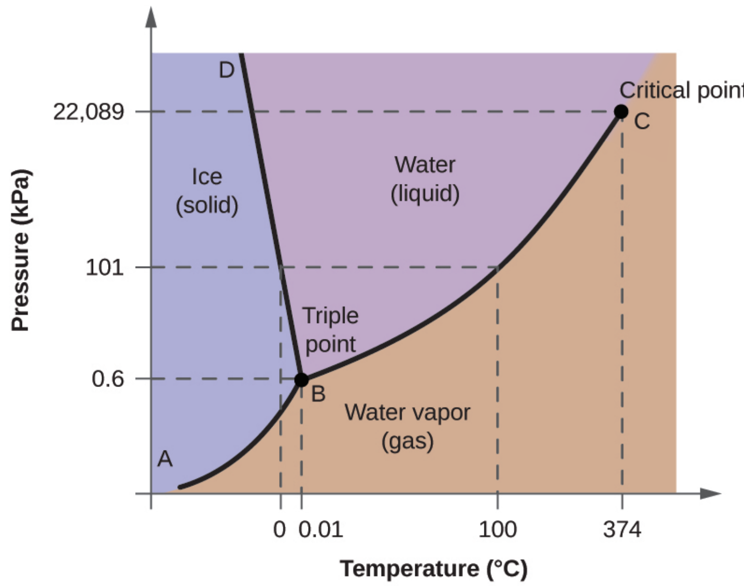

Figure 1.5: The phase digram of water [28].

space of T and μ_B. In this diagram, we can see that there has at least two distinct phases: a QGP phase at higher T (yellow area) and a hadronic phase at lower T (green area). Lattice QCD calculations predict a crossover transition from hadronic matter to a plasma of de-confined quarks and gluons (QGP) at vanishing μ_B [34]. At large μ_B, QCD-based model calculations suggest that the phase transition is of first-order [35, 36], shown as a black solid-line.

An important landmark of the QCD phase diagram is the critical end point (CP), where the first-order phase transition boundary terminates [35, 36, 37]. There must has a critical point if the smooth crossover and the first-order phase boundary exist. So far, many efforts have been made to search for the possible CP in heavy-ion collisions [30, 31, 38, 39, 40]. Experiments at RHIC (US) [30, 31, 38] and CERN SPS (EU) [39, 41] are ongoing to search for possible CP. In a few years, experiments at NICA (Russia) [42], FAIR (Germany) [40] as well as the HIAF (China) [43] will join in this research activity worldwide.

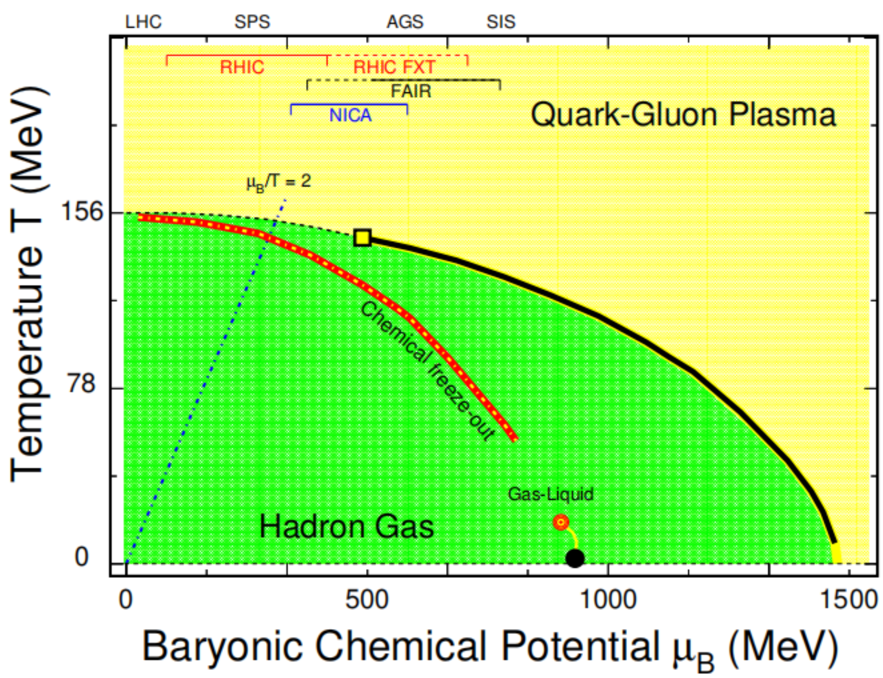

Figure 1.6: Schematic Quantum Chromdynamics (QCD) phase diagram in the thermodynamic parameter space spanned by the temperature T and baryonic-chemical potential μ_b. The solid black line denotes the first-order phase boundary between QGP and hadron phase. Solid square at the end of boundary, denotes the QCD critical point. Figure taken from Ref. [29].

1.3.2 Non-monotonic Energy Dependence of Observables in Heavy-ion Collisions

To locate the possible CP in the QCD phase diagram, researchers have attempted to vary the collision energy which covers a wide range of T and μ_B in heavy-ion collisions. When the critical point is passed by the thermodynamic condition of the QGP matter, the expected signature is the non-monotonic variation of the observable with the collision energy [33, 44, 45]. Several measurements from the BES program at RHIC have showed a non-monotonic variation with collision energy ($\sqrt{s_{_{\rm NN}}}$). These include the net-proton kurtosis [32, 46], the slope of directed flow for protons and net-protons [47], the Hanbury-Brown–Twiss (HBT) radii [48, 49], and yield ratio of light nuclei production [50].

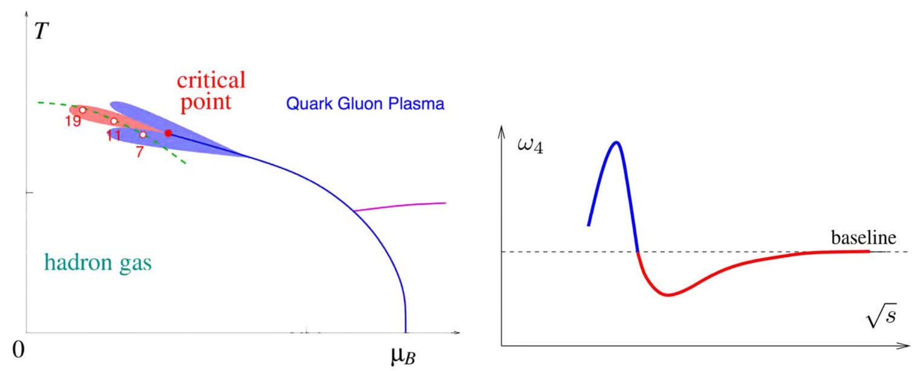

Figure 1.7: (Left) The sketch of the QCD phase diagram with sign of the fourth-order cumulants from calculations of the σ model. The red region represents negative values and the blue region represents positive values. The green dashed line is the chemical freeze-out lines in heavy-ion collisions. Figure taken from Refs. [33, 44]

.

The non-monotonic variation with collision energy was predicted by many model calculations. An most important calculations was from the σ field model that first time qualitatively discussed the universal critical behavior of the fourth order (kurtosis) of multiplicity fluctuations near the QCD critical point [33, 44]. The kurtosis is calculated by: $\kappa =< (\delta N)^4 >$

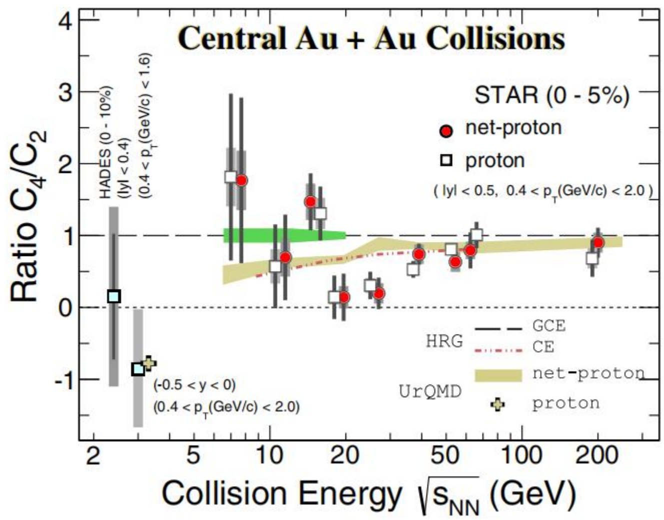

Figure 1.8: Collision energy dependence of the ratios of cumulants (C_4/C_2), for proton (squares) and net-protons (red circles) in the Au+Au collisions from the STAR experiment. Figure taken from Ref. [51].

$/\sigma^4 - 3$, where $\delta N = N - <N>$ and $\sigma^2 =< (\delta N)^2 >$, N is the multiplicity in a given and $<>$ denote the average over all events. In addition, the $\kappa\sigma^2$ is related to cumulant (C_n) by $\kappa\sigma^2 = C_4/C_2$, where $C_4 =< (\delta N)^4 > -3 < (\delta N)^2 >^2$ and $C_2 =< (\delta N)^2 >= \sigma^2$.

The C_4/C_2 for the net-baryon number is related to the ratio of susceptibilities λ_B^4/λ_B^2 which has different values for the hadronic and QGP phases [52]. Figure. 1.8 shows the C_4/C_2 as a function of collision energy ($\sqrt{s_{\mathrm{NN}}}$) in Au+Au collision from the STAR experiment at RHIC [32, 51], and it was found that C_4/C_2 for proton (squares) and net-protons (red circles) exhibit a non-monotonic energy dependence. This result was consistent with the prediction from QCD-inspired models [44, 45, 46].

In the meantime, the study of light nuclei production also showed a non-monotonic energy dependence from the STAR experiment [50, 53]. Based on the deduction of coalescence formula, the yield ratio $N_t \times N_p/N_d^2$ of triton (N_t), deuteron (N_d) and proton (N_p), was predicted to be sensitive to the neutron density fluctuations in heavy-ion collisions, and was expected to

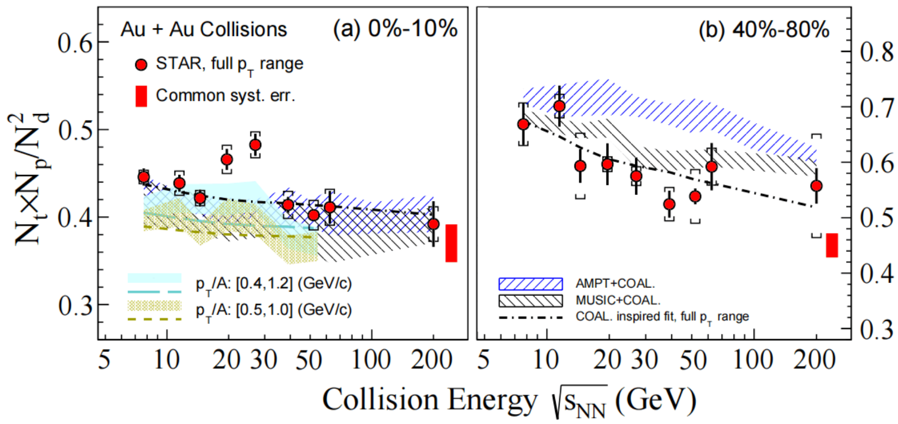

Figure 1.9: The yield ratio $N_t \times N_p/N_d^2$ of triton (N_t), deuteron (N_d) and proton (N_p) in the 0%-10% central (left panel) and 40%-80% peripheral (right panel) Au+Au collisions from the STAR experiment at RHIC. Figure taken from Refs. [50, 53]

.

show a non-monotonic behavior with collision energy [54, 55]. Figure 1.9 shows $N_t \times N_p/N_d^2$ as a function of collision energy in the 0%-10% central (left panel) and 40%-80% peripheral (right panel) Au+Au collisions from the STAR experiment. As we can see, $N_t \times N_p/N_d^2$ indeed shows a non-monotonic energy dependence with an enhancement in the 0%-10% central collisions, while it has a smooth decreasing with increasing energy in the 40%-80% peripheral collisions. The observed non-monotonic behavior may be due to the enhanced baryon density fluctuations induced by the QCD critical point or first-order phase transitions in heavy-ion collisions [50, 53].

The intermittency analysis also aims to search for the possible the QCD critical point, and we will investigate whether the corresponding observable also exhibits a non-monotonic energy dependence in the STAR experiment.

1.4 The Framework of Intermittency Analysis in Heavy-ion Collisions

Intermittency phenomenon is termed as big bursts from small region (cells) of the phase space, which signal unusual fluctuations of density [56, 57]. Based on the QCD state equation belonging to the 3D-Ising universality class, it's shown that large density fluctuations near the CP will lead to critical intermittency in heavy-ion collisions [56, 58, 59, 60, 61]. In this section, we introduce the framework of intermittency analysis and how to search the QCD critical point via an intermittency analysis in heavy-ion experiment. The observable, scaled factorial moments, and its power-law (scaling) behavior are describe in detail.

1.4.1 Local Density Fluctuations in Heavy-ion Collisions

Upon approaching a critical point, the correlation length of system diverges and the system becomes scale invariant, or self-similar when small pieces of an object are similar to the whole object [62, 63, 64]. Analogous to the critical opalescence, a striking light scattering phenomenon near criticality, large density fluctuations are developed due to self-similar structure of the system near the QCD critical point [54, 55, 58, 59].

At first, the basic theoretical input is provided by the effective action of the 3D Ising model $\tau[n]$, which represents QCD in the vicinity of critical point $T = T_c$, $\mu = \mu_c$. For a QCD critical system, the $\tau_c[n]$, which can be looked upon as the free energy, is given by [56, 58, 59]:

$$\Gamma_c[n] = T_c^{-5} g^2 \int d^3\vec{x}[\frac{1}{2}|\nabla n|^2 + G g^{\delta-1} T_c^8 |T_c^{-3} n|^{\delta+1}]. \tag{1.1}$$

where $\delta \simeq 5$ is the isotherm critical exponent, G is a dimensionless coupling in the effective potential and within a range $[1.5 - 2]$, n denote $n(\vec{x})$ which is the particle number density in coordinate space.

The free energy Eq. (1.1) must be adapted the relativistic geometry of the nuclear collision system. For this purpose, the longitudinal coordinate $x_\parallel$ is replaced by the space-time rapidity

y, and then $dx_{\parallel} = \tau_c coshydy, n(\vec{x}_{\perp}) = \rho(\vec{x}_{\perp})[2\tau_c sinh(\delta y/2)]^{-1}$. Integrating now in rapidity, Eq (1.1) is simplified as follows [56, 58, 59]:

$$\Gamma_c[n] = Cg^2 \int d^2\vec{x}_{\perp}[\frac{1}{2}|\nabla_{\perp}\rho|^2 + G(gC)^{\delta-1}\rho^{\delta+1}]. \tag{1.2}$$

The critical fluctuations of system belonging to the class of Eq. (1.2) can be described in a scheme where the partition function is as follows [56, 58, 59]:

$$Z\sum_s e^{-\tau_c[\rho_B^s]}; \qquad \nabla_{\perp}\rho_B^s - (\delta+1)G(gC)^{\delta-1}[\rho_B^s]^{\delta}] = 0 \tag{1.3}$$

A main characteristic of critical matter ($\delta \simeq 5, G \simeq 2$) produced in nuclear collisions revealed by Eq. (1.3), is that the density correlator $< \rho(\vec{x}_{\perp})\rho(0) >$ obeys a power-law structure:

$$< \rho(\vec{x}_{\perp})\rho(0) >\sim |\overrightarrow{x_{\perp}}|^{d_F-2}, \qquad d_F = \frac{2\delta}{\delta+1} \tag{1.4}$$

where $d_F \simeq \frac{3}{5}$ is the fractal dimension. The power-law behavior in Eq. (1.4) is the origin of critical opalescence with large density fluctuations in QCD matter.

The power-law of Eq. (1.4) developed in the coordinate space, can be transferred to the momentum space for a small momentum transfer $\vec{k}$:

$$\lim_{|\vec{k}|\to 0}\langle\rho_{\vec{k}}\rho_{\vec{k}}^*\rangle \sim |\vec{k}|^{-d_F}, \tag{1.5}$$

where $\rho_{\vec{k}}$ is the Fourier transform of particle number density from the coordinate space, and $\langle\rho_{\vec{k}}\rho_{\vec{k}}^*\rangle$ is the two-particle correlator in momentum space. The Eq. (1.5) reveals a self-similar, or fractal, structure in momentum space with a fractal dimension $\tilde{d}_F = 2 - d_F$. This self-similar structure will give rise to large local density fluctuations which provides a tool for the detection of a critical point in heavy-ion reactions.

In Fig. 1.10, clusters was produced in the entire phase space that illustrate the large local density fluctuations in heavy-ion reaction. Figure 1.10 (b) shows the distribution of cluster in the transverse momentum phase space. It's shown that there are many bursts from small cell of phase space, which is a typical phenomenon of intermittency.

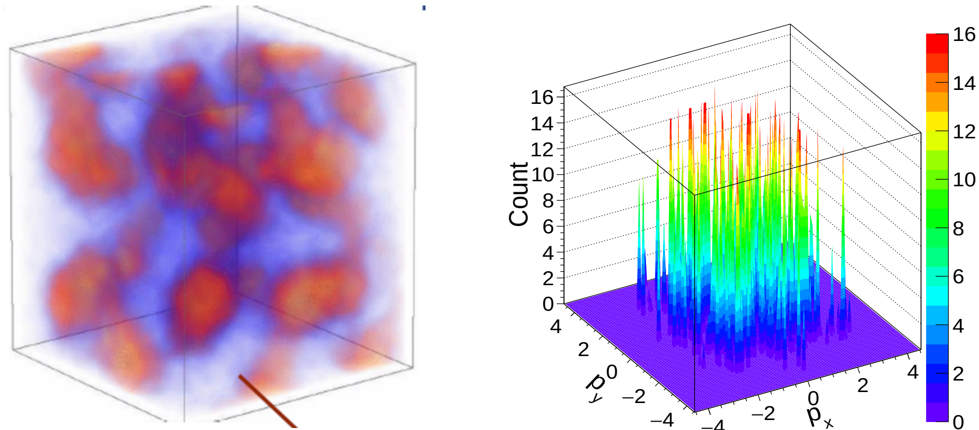

(a)

(b)

Figure 1.10: (a) a cartoon shows large local density fluctuations in $3D$ phase space. Figure taken from Ref. [54]. (b) a cartoon shows large local density fluctuations in transverse momentum phase space.

1.4.2 The Observable: Scaled Factorial Moment (SFM)

In high energy experiments, the intermittency driven by local density fluctuations can be measured by calculating the scaled factorial moment (SFM) of final state particles in momentum space [56, 58, 59, 65]. The SFMs are chosen to be sensitive to the power-law singularity of Eq. (1.5). For this purpose, the phase space is partitioned into M^D equal-size cells, and the qth-order SFM, $F_q(M)$, is defined as [58, 59, 65]:

$$F_q(M) = \frac{\langle \frac{1}{M^D} \sum_{i=1}^{M^D} n_i(n_i-1)\cdots(n_i-q+1)\rangle}{\langle \frac{1}{M^D} \sum_{i=1}^{M^D} n_i\rangle^q}, \tag{1.6}$$

where M^D is the number of cells in D-dimensional momentum space, n_i is the measured multiplicity in the ith cell, and the angle bracket denotes an average over all the events.

For example, Fig. 1.11 show the transverse momentum phase space(p_x, p_y) space is partitioned into 16 cells when $M = 4$, then n_i is the number of black point in the ith cell. When the

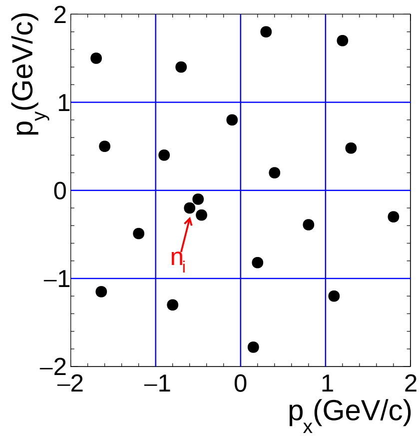

Figure 1.11: The transverse momentum space (p_x, p_y) is partitioned into 16 cells to calculate the SFM of multiplicity distribution.

transverse momentum space (p_x, p_y) is partitioned to M^2 equal-size cells and the order $q = 2$, Eq. (1.6) is shortly rewritten as follows:

$$F_2(M) = \frac{\langle \frac{1}{M^2} \sum_{i=1}^{M^2} n_i(n_i - 1) \rangle}{\langle \frac{1}{M^2} \sum_{i=1}^{M^2} n_i \rangle^2}, \tag{1.7}$$

The study of multiplicity fluctuations in decreasing phase-space intervals using the method of SFM was first proposed several years ago [57, 66]. Recent studies show that one can estimate the possible critical region of the QCD critical point by using the intermittency analysis together with the estimated free-out parameters [58, 59].

1.4.3 Intermittency Index

The intermittency phenomenon appears as a power-law (scaling) behavior of SFMs [57, 58, 67]. If a system features local density fluctuations, we expect a power-law behavior of $F_q(M)$ on the number of cells (M^D), defined as follows [58, 59, 60, 65]:

$$F_q(M) \propto (M^D)^{\phi_q}, M \gg 1, \tag{1.8}$$

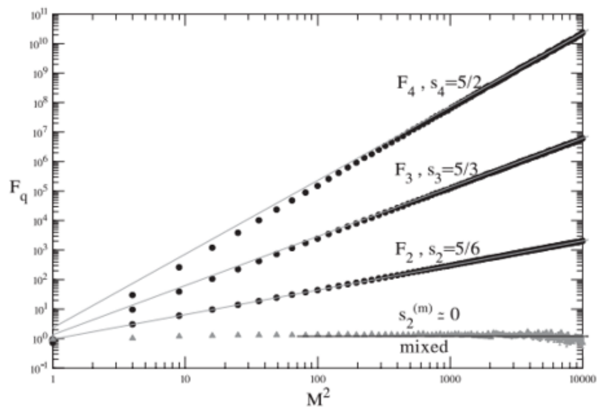

Figure 1.12: $F_q(M)$ (q=2-4) as a function of M^2 for a critical 3D Ising-like system. Figure taken from Ref. [58].

where ϕ_q is called the intermittency index characterizing the strength of the intermittency. The power-law behavior of Eq. (1.8) is expressed as $F_q(M)/M$ scaling where the sign ”/” denotes ”versus”. Near the QCD critical point, the value of ϕ_q is predicted to be equal to $5 \times (q-1)/6$ for baryons and $2 \times (q-1)/3$ for pions in the transverse momentum phase space [58, 67]. It's worth to note that intermittency could be observed in the first-order transition since density fluctuations in this region can be large and even follow a power-law geometry [68].

Figure 1.12 shows the $F_q(M)$ $(q = 2-6)$ as a function of M^2 in double-logarithmic. It is shown that $F_q(M)$ obey a clear power-law (scaling) behavior for a critical 3D-Ising system, equivalently, the relationship between $F_q(M)$ and M^2 is a linear line in a double-logarithmic plot.

1.4.4 Scaling Exponent

Another type of power-law behavior of higher-order $F_q(M)$ versus second-order $F_2(M)$ is defined as: [69, 70, 71, 72]:

$$F_q(M) \propto F_2(M)^{\beta_q}, M \gg 1, \tag{1.9}$$

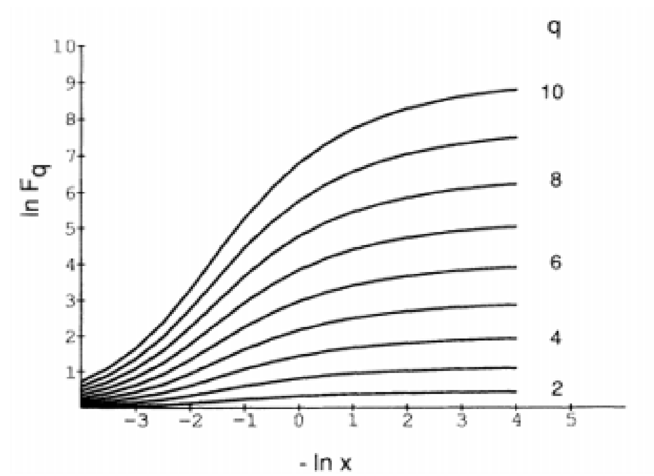

Figure 1.13: F_q (q=2-4) as a function of the size of cell x according to Ginzburg-Landau (GL) description of critical system. Figure taken from Ref. [69].

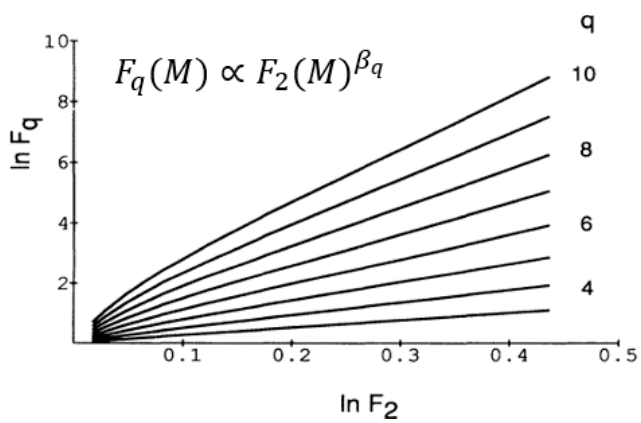

Figure 1.14: F_q (q=2-4) as a function of F_2 according to Ginzburg-Landau (GL) description of critical system. Figure taken from Ref. [69].

where β_q is the scaling index. Here, the power-law behavior of Eq. (1.9) is expressed as $F_q(M)/F_2(M)$ scaling. According to Ginzburg-Landau (GL) description of critical system [69, 70], $F_q(M)/F_2(M)$ scaling is observed experimentally, while $F_q(M)/M$ scaling could be washed out or absent. This is because that ϕ_q depends on the particular critical parameters which would vary with the temperature of system and are unknown in the dynamical evolution of collision system. However, $F_q(M)/F_2(M)$ scaling of Eq. (1.9) is a universal and visible behavior that is independent of whether $F_q(M)/M$ scaling is fully realized near the QCD critical point, since β_q is independent of those critical parameters. As show in Fig. 1.13 the relationship between $F_q(M)$ and M is a curve, but we can see in Fig. 1.14 that the relationship between $F_q(M)$ and $F_2(M)$ is still be linear.

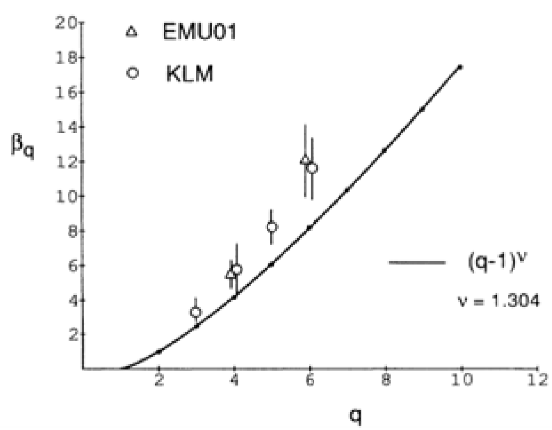

Figure 1.15: β_q as a function of $q-1$ according to Ginzburg-Landau (GL) description of critical system. Figure taken from Ref. [69].

To describe the general consequences of the phase transition, independent of considering details of critical parameters, the scaling exponent is defined and given by the power-law relationship between β_q and q [69, 70, 73, 74]:

$$\beta_q \propto (q-1)^{\nu}. \tag{1.10}$$

Here ν specifies the $F_q(M)/F_2(M)$ scaling of all orders and quantifies the strength of intermittency. The energy dependence of ν could be used to search for the signature of the QCD critical point. Figure 1.15 shows β_q as a function of $q-1$ based on the GL theory [69]. Near the QCD critical point, the critical value of ν is predicted to be equal to 1.304 in the entire space phase based on GL theory [69] and 1.0 from calculations of the 2D Ising model [70, 75]. Without subtracting background, ν = 1.743 from the UrQMD model [76] and 1.94 from the AMPT model [77]. These large values of ν from transport models are driven by backgrounds, while ν can not be extracted after background subtraction. It is important to note that a larger value of ν does not imply more fluctuations because it may well be the consequence of a smaller ϕ_2 [70].

Figure 1.16 shows the steps how to calculate the intermittency index (ϕ_q) and scaling exponent ν in the framework of intermittency analysis. At first, we calculate the scaled factorial moments of multiplicity distribution in transverse momentum (p_x, p_y) space. Then, we can calculate ϕ_q once $F_q(M)$ obey a power-law behavior with M^2, and β_q once $F_q(M)$ obey a power-law behavior with $F_2(M)$. At last, the scaling exponent ν is extracted from the power-law behavior of $\beta_q \propto (q-1)^\nu$. The centrality and energy dependence of ϕ_q and ν are the focus of this study.

$$F_q(M) = \frac{< \frac{1}{M^D} \sum_{i=1}^{M^D} n_i(n_i-1)\ldots(n_i-q+1) >}{< \frac{1}{M^D} \sum_{i=1}^{M^D} n_i >^q}$$

$$\Downarrow$$

$$F_q(M) \propto (M^2)^{\phi_q}$$

$$\Downarrow$$

$$F_q(M) \propto F_2(M)^{\beta_q}$$

$$\Downarrow$$

$$\beta_q \propto (q-1)^\nu$$

Figure 1.16: The observables in the framework of intermittency analysis.

1.4.5 Intermittency Analysis from the NA49 and NA61 Experiments

Experiments at CERN Super Proton Synchrotron (SPS) [39, 78] are ongoing to search for critical intermittency by measuring nuclear collisions at various energies. Attempts has been made by the NA49 experiment through changing system sizes of colliding nuclei (p+p, C+C, Si+Si, Pb+Pb) at $158A$ GeV/c and NA61/SHINE experiment by varying energies in p+p,p+Pb, Be+Be, Ar+Sc and Xe+La collisions.

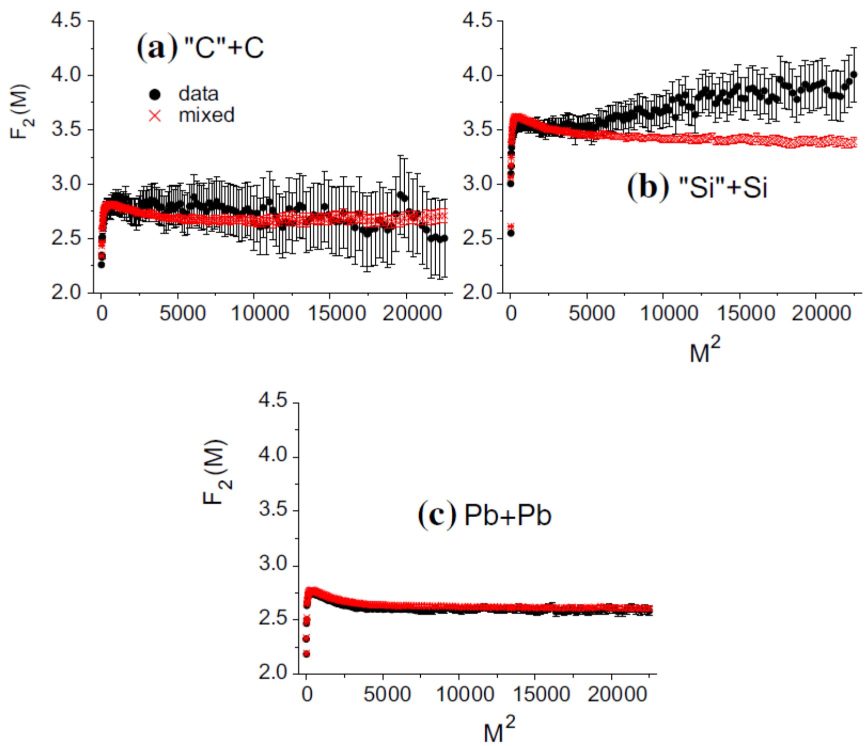

Figure 1.17: The measured second-order SFMs, $F_2(M)$, as a function of M^2 for proton in the most central collisions at $\sqrt{s_{\rm NN}}$ = 17.3 GeV for (a) C+C, (b) Si+Si, and (c) Pb+Pb collisions. The circles and crosses represent the $F_2(M)$ of the data and of the mixed events, respectively. Figure taken from Ref. [65].

Figure 1.17 shows $F_2(M)$ as a function of M^2 for data and mixed events at $\sqrt{s_{\mathrm{NN}}}$ = 17.3 GeV in C+C, Si+Si and Pb+Pb collisions from the NA49 experiment. The mixed event method is applied to eliminate the background contribution and its detail is described in Sec. 2.1.1. In Fig. 1.17, it is shown that $F_2(M)$ is larger than those of mixed events in the large M^2 region. The $\Delta F_2(M)$ $[F_2(M)^{data} - F_2(M)^{mix}]$ was found to obey a power-law behavior with M^2 in the Si+Si collisions and the extracted $\phi_2 = 0.96 \pm 0.16$ approached theoretical prediction [58], indicating the presence of intermittency in Si+Si collision. However, the $F_2(M)$ was almost overlap with those of mixed events in the C+C and Pb+Pb collisions, and therefore intermittency was not visible in these two collision system. The reason is that the density fluctuations can not develop in the small size of C+C system, and the signal of intermittency could be washed out during the longer evolution of the hadronic phase in the Pb+Pb collision [65].

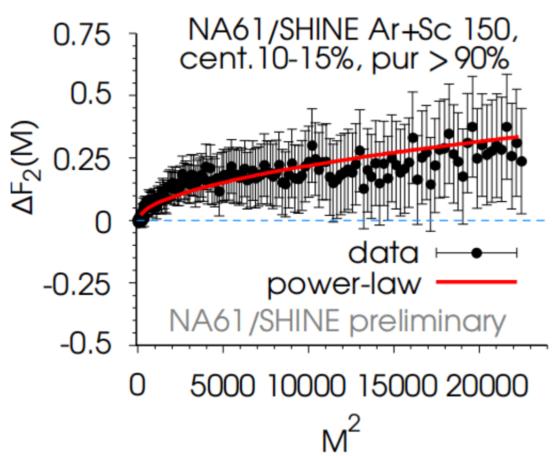

Figure 1.18: The measured $\Delta F_2(M)$ as a function of M^2 of proton density in 10-15% central Ar+Sc collisions at $150A$ GeV/c. Figure taken from Ref. [79].

In the successor to NA49, the NA61/SHINE experiment measured the intermittency for proton in the Be+Be and Ar+Sc collisions [39, 80]. Figure 1.18 shows the preliminary results on $\Delta F_2(M)$ $[F_2(M)^{data} - F_2(M)^{mix}]$ in 10-15% central Ar+Sc collisions at $150A$ GeV/c. It is observed that $\Delta F_2(M)$ obey a weak power-law with M^2, however the statistical uncer-

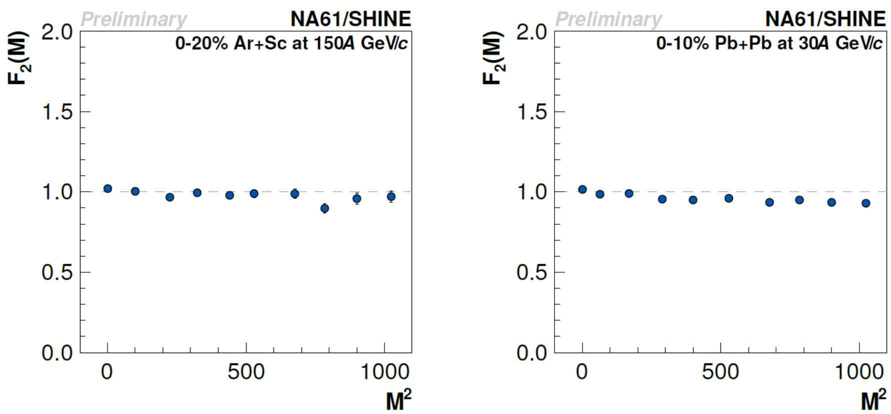

Figure 1.19: The measured second-order SFMs, $F_2(M)$, as a function of M^2 of proton density in 0-20% central Ar+Sc collisions at $150A$ GeV/c and in 0-10% central Pb+Pb collisions at $30A$ GeV/c. Figure taken from Ref. [80].

tainties of data points are large [79]. Furthermore, Fig. 1.19 shows the $F_2(M)$ as a function of M^2 in 0-20% central Ar+Sc collisions at $150A$ GeV/c and in 0-10% central Pb+Pb collisions at $30A$ GeV/c [79, 80]. Compared with the results in Fig. 1.18, the results in Fig. 1.19 is calculated using the cumulative variable method which is also used to subtract background contributions and is described in Sec. 2.1.2. It shows that $F_2(M)$ with cumulative transformation, is nearly flat with increasing M^2, therefore the intermittency was not observed in Ar+Sc and Pb+Pb collisions.

1.4.6 Intermittency Analysis from the UrQMD Model with Hadronic Potentials and Hydro

Recently, the UrQMD Model with hadronic potentials [81] is made to reproduce the signature of intermittency observed in experiment. In this model, the momentum correlations between proton pairs is included into the mean-field mode of the the UrQMD model [81]. By treating density-dependent potentials for both formed hadron and preformed hadron from string

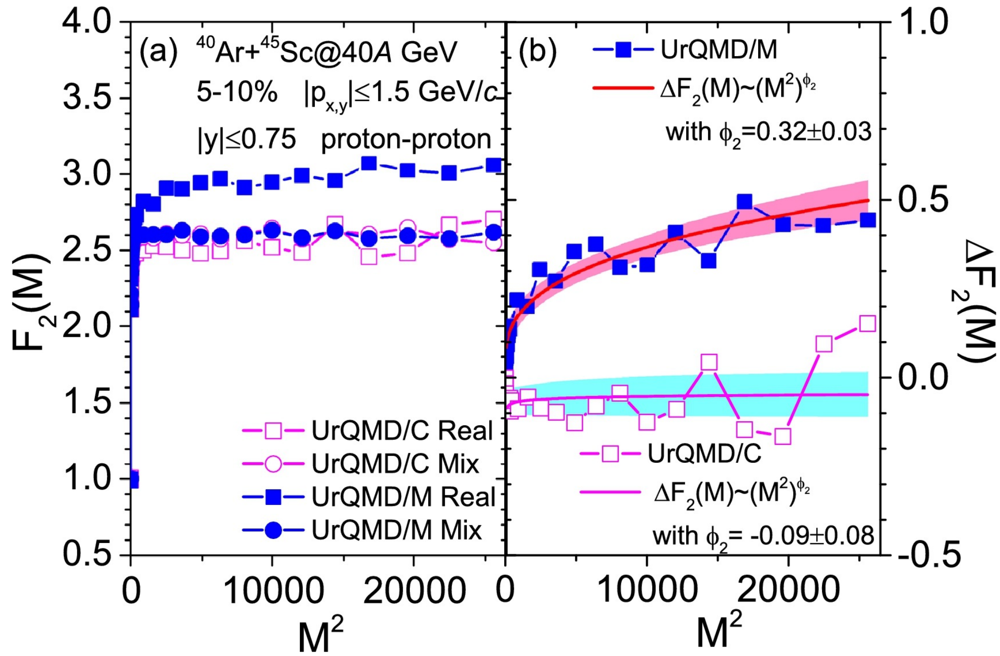

Figure 1.20: (a) $F_2(M)$ as a function of M^2 in the 5-10% central Ar+Sc collisions at 40A GeV/c. The solid squares (circles) are $F_2(M)$ of real events (mixed events) from the UrQMD model with hadronic potentials (UrQMD/M). The corresponding open squares and circles represent the measurements without hadronic potentials (UrQMD/C). (b) $\Delta F_2(M)$ as a function of M^2. Figure taken from Ref. [81].

fragmentation in a similar way, the density-dependent potentials is written as [81, 82]:

$$U = \alpha(\frac{\rho_h}{\rho_0}) + \beta(\frac{\rho_h}{\rho_0})^{\gamma}, \tag{1.11}$$

where ρ_0 is the nuclear matter saturation density and ρ_h is the hadronic density.

The momentum-dependent term of hadronic potential is defined as:

$$U_{md} = \sum_{k=1,2} \frac{t^k_{md}}{\rho_0} \int d\mathbf{p}' \frac{\mathbf{f}(\mathbf{r}, \mathbf{p}')}{\mathbf{1} + [(\mathbf{p} - \mathbf{p}')/\mathbf{a}^{\mathbf{k}}_{\mathbf{md}}]^{\mathbf{2}}}. \tag{1.12}$$

where t_{md} and a_{md} are parameters. More detailed description of the UrQMD model with hadronic potentials can be found in Refs [81, 82].

In Fig 1.20 (a), $F_2(M)$ from real events and mixed events show as a function of M^2 in the $5-10\%$ central Ar+Sc collisions at 40A GeV/c from the UrQMD model with and without hadronic potentials, and the correlator $\Delta F_2(M)$ $[F_2(M)^{real} - F_2(M)^{mix}]$ is shown in Fig 1.20 (b). For the UrQMD model with hadronic potential, $F_2(M)$ of real events is larger than those of mixed events, and $\Delta F_2(M)$ shows a power-law behavior with M^2, indicating the presence of intermittency in this model. Moreover, the $\phi_2 = 0.32 \pm 0.03$ extracted from the power-law behavior of $\Delta F_2(M)$, is similar to the one measured from the NA61 experiment [83]. For the UrQMD cascade model (UrQMD/C), it is observed that the values of $F_2(M)$ of real events are almost overlapped with those of mixed events and thus $\Delta F_2(M)$ is around 0. The extracted ϕ_2 is around zero from the UrQMD/C model. The comparison between the results from the UrQMD/M and those from the UrQMD/C model, indicates that the power-law behavior of $\Delta F_2(M)$ in the UrQMD/M model is due to the hadronic interactions, particular nuclear potentials which lead to an enhancement of proton pairs with small relative momenta [81, 84].

Besides the UrQMD/M model that hadronic potentials is added into the UrQMD model, another model is the UrQMD-hydro model that incorporating both transport and hydro-dynamical descriptions of heavy-ion collisions[85, 86]. In the UrQMD-hydro model, microscopic transport calculation for initial condition and freeze-out procedure is implemented with intermediate hydrodynamic calculations [85]. Figure. 1.21 shows $\ln F_q(M)$ as a function of $\ln M^2$ for all

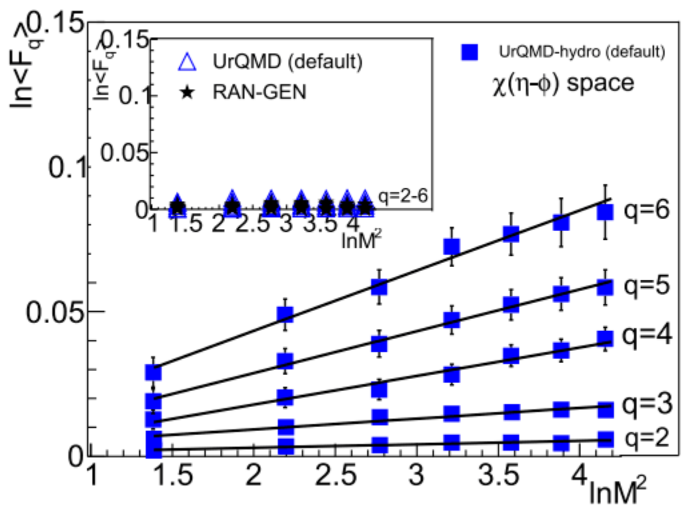

Figure 1.21: $\ln F_q(M)$ vs $\ln M^2$ for all charged particles in Au+Au collisions at 10A GeV/c from the UrQMD model with and without hydrodynamic. Figure taken from Ref. [85].

charged particles in Au+Au collisions at 10A GeV/c from the UrQMD-hydro model. In addition, variation of $\ln F_q(M)$ with M^2 from the original UrQMD model is shown in a small panel in Fig. 1.21. It is observed that $\ln F_q(M)$ for all orders ($q = 2 - 6$) increase with increasing $\ln M^2$ in the (0–5%) central Au+Au collisions from the UrQMD-hydro model, while no power-law behavior of $F_q(M)$ is visible in the original UrQMD model. This results infer that the observed intermittency is closely related to the hydrodynamic evolution of the medium produced in heavy-ion collision [84, 85]. It is worth to note that this observe signal is weak since the intermittency index $\phi_2 \simeq 0.02$ is small.

Chapter 2

Analysis Method

2.1 Background Subtraction

2.1.1 Mixed Event Method

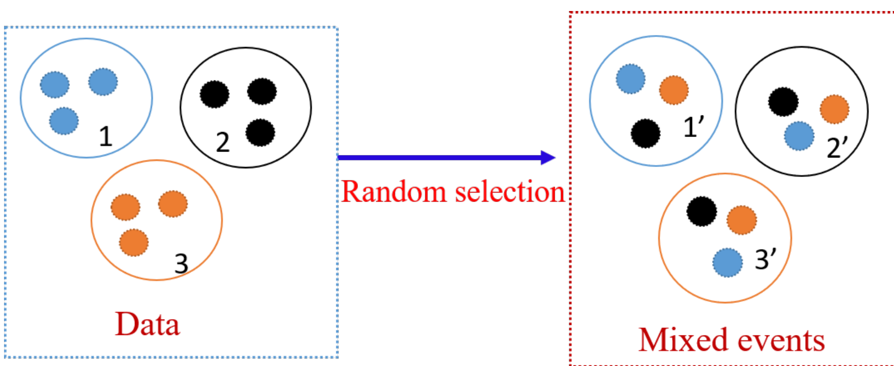

Figure 2.1: A simple case for constructing mixed events.

In practice, heavy-ion collision systems involve a large number of background effects that will significantly influence the particle multiplicity spectra in finite space [60, 65, 87]. When measuring scaled factorial moments, a large number of background effects significantly influence the results. These effects including the conservation laws, resonance decays, finite lifetime of system, statistical fluctuations, experimental acceptance as well as other source for trivial fluctuations, must be subtracted at the level of scaled factorial moments. The NA49 and NA61 experiments [60, 65, 83] apply the mixed event method to eliminate background contributions. For this purpose, additional observable, $\Delta F_q(M)$, is defined as:

$$\Delta F_q(M) = F_q^{data}(M) - F_q^{mix}(M). \tag{2.1}$$

The $\Delta F_q(M)$, instead of $F_q(M)$, is exclusively used to extract the ϕ_q in the power-law function of $\Delta F_q(M) \propto (M^D)^{\phi_q}$, equivalently, $\Delta F_q(M)/M$ scaling. And β_q in the power-law function of $\Delta F_q(M) \propto \Delta F_2(M)^{\beta_q}$, equivalently, $\Delta F_q(M)/\Delta F_2(M)$ scaling.

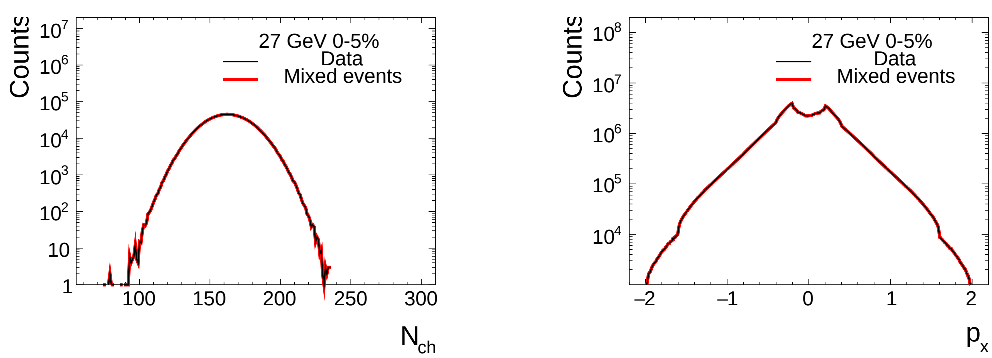

(a)

(b)

Figure 2.2: (a) N_{ch} distribution from data and mixed event in 0-5% central collisions at $\sqrt{s_{\rm NN}}$ = 27 GeV. (b) p_x distribution from data and mixed event in 0-5% central collisions at $\sqrt{s_{\rm NN}}$ = 27 GeV.

Mixed events are constructed by randomly selecting particles from different original events, while reproducing the multiplicity distribution of original events. The correlations between pairs of particles which exist in the original event, are eliminated in the mixed event samples since each particle now is chosen from different events. The method of mixed event obey three rules as following:

1) Mixed events are constructed by randomly selecting particles from the real (true) events.

2) Each particle in a mixed event is selected from a differently real event. As show in Fig. 2.1, the three particles in mixed event-1 are selected from real event-1, 2 and 3.

3) The multiplicity distribution, total distributions of the mixed event are the same as the real events. In Fig. 2.2, we can see that line of N_{ch}^{Data} distribution is overlapped with N_{ch}^{mix}, p_x^{Data} is also overlapped with p_x^{mix}.

2.1.2 Cumulative Variable Method

Besides the mixed event method to eliminate background contributions, another method is the cumulative variable, which has been proved to drastically reduce distortions of intermittency due to nonuniform single-particle density from background contributions [88, 89].

The cumulative variable $X(x)$ is related to the single-particle density distribution $\rho(x)$ through [88, 89]:

$$X(x) = \frac{\int_{x_{min}}^{x} \rho(x)dx}{\int_{x_{min}}^{x_{max}} \rho(x)dx}. \tag{2.2}$$

Here x represents the original measured variable, e.g., p_x or p_y. $\rho(x)$ is the density function of x. x_{min} and x_{max} are the lower and upper phase-space limits of the chosen variable x.

The cumulative variable $X(x)$ is determined by the shape of density distribution $\rho(x)$. The distribution of the new variable $X(x)$ is uniform in the interval from 0 to 1. It has been proved that the cumulative variable could remove the dependence of the intermittency parameters on the shape of particle density distributions and give a new way to compare measurements from different experiments [89]. To use the cumulative variable, the two-dimensional momentum space p_xp_y which is partitioned into M^2 cells will transfer to be p_Xp_Y space. And the SFM directly calculated in p_xp_y space $[F_2(M)]$ will transfer to be $CF_2(M)$, which is now calculated in p_Xp_Y space. The process of fitting ϕ_2^c from $CF_2(M)$ is similar to that of ϕ_2 from $F_2(M)$ according to Eq. (1.8).

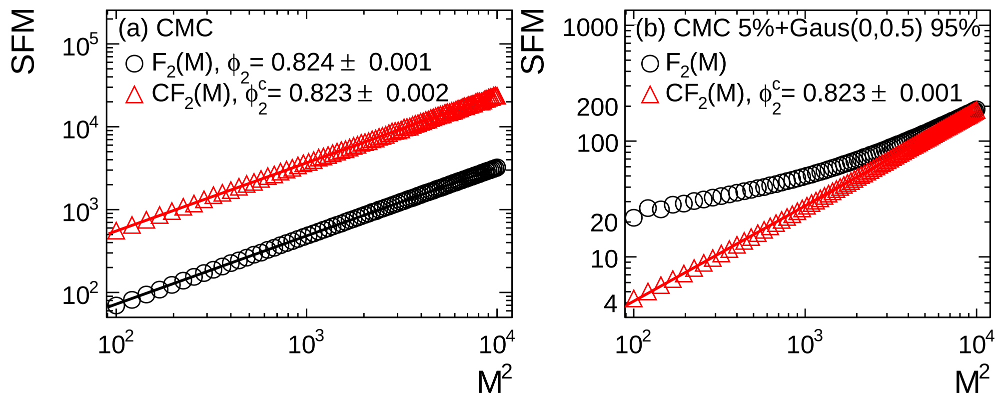

Figure 2.3: The black symbols represent the second-order scaled factorial moment as a function of number of partitioned cells (a) in pure CMC events and (b) in CMC events contaminated with Gaussian background fluctuations. The corresponding red ones are the SFMs calculated by the cumulative variable method.

To test the validity of the cumulative variable method in the calculations of SFMs, we use a Critical Monte Carlo (CMC) model [58, 61] of the 3D Ising universality class to generate critical event samples. The CMC model involves the self-similar or intermittency nature of particle correlations and leads to an intermittency index of $\phi_2 = \frac{5}{6}$ [58]. In Fig. 2.3(a), both $F_2(M)$ (black circles) and $CF_2(M)$ (red triangles) are shown in the same panel. We observe that $CF_2(M)$ follows a good power-law behavior as $F_2(M)$ with increasing M^2. Within statistical errors, the intermittency index ϕ_2^c fitted from $CF_2(M)$ equals ϕ_2 obtained from $F_2(M)$. It means that the cumulative variable method does not change the intermittency behavior for a pure critical signal event sample, which has been proved by Bialas and Gazdzicki when they proposed to use the cumulative variable method to study intermittency [89]. In Fig. 2.3(b), the CMC event sample is contaminated by hand with a statistical Gaussian background contribution, with the mixed probability $\lambda = 95\%$. The chosen value of λ is close to the one used in the simulations of background in the NA49 experiment [65]. In this case, one finds that the directly calculated $F_2(M)$ deviates substantially from the linear dependence, i.e., violation of the scaling law because of the Gaussian background contribution. So we can not make a good fitting based on the scaling function defined in Eq. (1.8). However, the trend of $CF_2(M)$, which is calculated by the cumulative variable method, still obeys a similar power-law dependence on M^2 as that in Fig. 2.3(a). Furthermore, the intermittency index ϕ_2^c calculated from $CF_2(M)$ keeps unchanged when comparing to the one in original CMC sample shown in Fig. 2.3(a). We feel that these results are encouraging. They confirms that, in the intermittency analysis, the cumulative variable method efficiently removes the effects caused by the background contribution.

2.2 Efficiency Correction: A Cell-by-cell Method

In the experiment, some particles are not recorded due to the limited capacity of the TPC and TOF detectors, hence the measured multiplicity distribution is different from the true one. The values of SFMs are influenced by the efficiency of detector since they are calculated from the measured multiplicity distribution of particles. To recover the true SFM from the experimentally measured one, one needs to perform a careful study on the efficiency effect. Generally, the efficiencies in experiments are obtained by using Monte Carlo (MC) embedding technique. This allows for the determination of the efficiency, which is the ratio of the matched MC tracks number and the number of input tracks. It contains the effects of tracking efficiency, detector acceptance and interaction losses.

Let us denote the number of produced particles as N and the number of experimental measured ones as n with a detection efficiency ϵ. To correct the factorial moment for efficiency effects, one has to invoke a model assumption for the response of the detector. It is often assumed to follow a binomial probability distribution function [90, 91]. Moreover, according to the detector simulations in the STAR experiment, the detector response is close enough to the binomial distributions within statistical significance up to the 6th-order cumulants [32, 46, 92]. Then the probability to measure n particles given N produced particles can be expressed as

$$p(n|N) = B(n, N; \epsilon) = \frac{N!}{n!(N-n)!}\epsilon^n(1-\epsilon)^{N-n}. \tag{2.1}$$

The true factorial moment is defined as $f_q^{true} = \langle N(N-1)...(N-q+1)\rangle$. It can be recovered by dividing the measured factorial moment, $f_q^{measured} = \langle n(n-1)...(n-q+1)\rangle$, with appropriate powers of the detection efficiency [90, 93, 94]:

$$f_q^{corrected} = \frac{f_q^{measured}}{\epsilon^q} = \frac{\langle n(n-1)...(n-q+1)\rangle}{\epsilon^q}. \tag{2.2}$$

This strategy has been used for the efficiency corrections in the high-order cumulant analysis [46, 93]. Consider that the probability to detect a particle is governed by a binomial distribution, then both cumulants [93] and off-diagonal cumulants [91] can be expressed in term of factorial moments and then can be corrected by using Eq. (2.2).

We apply the strategy for the efficiency correction to SFMs. Since the available region of phase space is partitioned into a lattice of M^2 equal-size cells, every element $\langle n_i(n_i-1)...(n_i-q+1)\rangle$ of measured SFMs should be corrected one by one. In this way, the efficiency corrected SFM is deduced as

$$F_q^{corrected}(M) = \frac{\langle \frac{1}{M^2}\sum_{i=1}^{M^2} \frac{n_i(n_i-1)\cdots(n_i-q+1)}{\bar{\epsilon_i}^q}\rangle}{\langle \frac{1}{M^2}\sum_{i=1}^{M^2} \frac{n_i}{\bar{\epsilon_i}}\rangle^q}. \tag{2.3}$$

Here, n_i denotes the number of measured particles located in the i-th cell. The mean $\bar{\epsilon_i}$, is calculated by $\langle \frac{\sum_{j=1}^{n_i}\epsilon_i^j}{n_i}\rangle$, representing the event average of the mean efficiency for the particles located in the ith cell. Its value depends on the momentum range of the i-th cell and particle species in experimental measurement [46, 94]. We call the efficiency correction technique of Eq. (2.3) the cell-by-cell method.

To demonstrate the validity of the cell-by-cell method, we employ the UrQMD model with the particle detection efficiencies used in real experiments. It is simulated by injecting particle tracks from UrQMD events into the STAR detector acceptance with the experimental efficiencies. In Fig. 2.4(a), we show the p_T dependence of the experimental efficiency in only the TPC detector in the most central Au + Au collisions at $\sqrt{s_{\rm NN}}$ = 19.6 GeV. It first increases with increasing p_T, and then gets saturated in higher-p_T regions. We employ this tracking

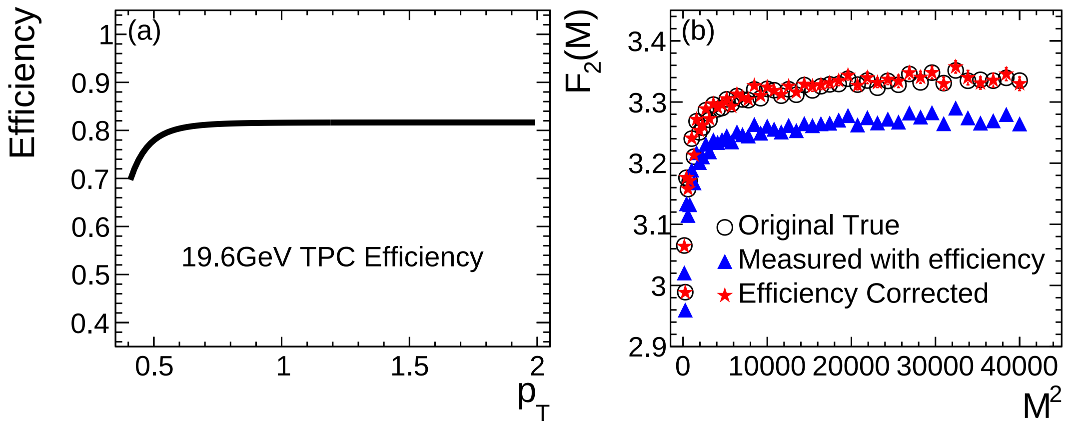

Figure 2.4: (a) Experimental tracking efficiencies as a function of p_T in the TPC detector in 0-5% Au + Au collisions. (b) The second-order SFM as a function of number of partitioned cells from UrQMD calculations.

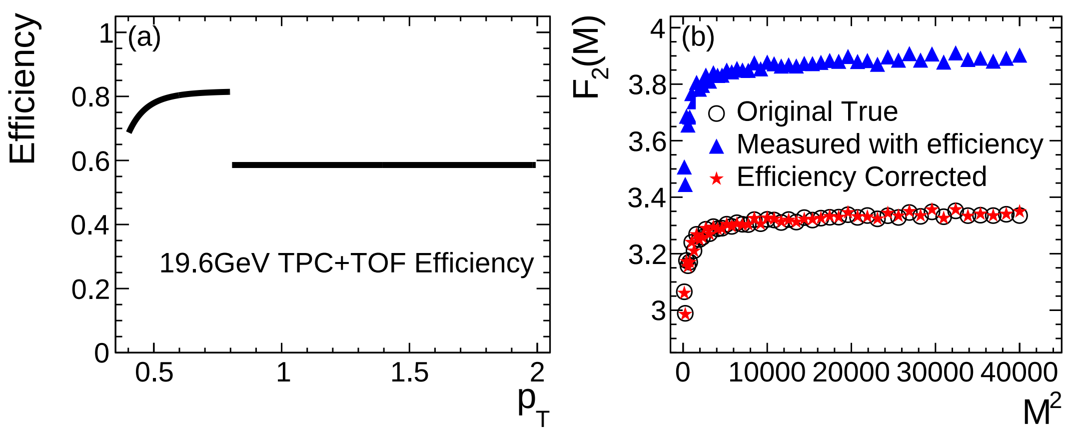

Figure 2.5: (a) Experimental tracking efficiencies as a function of p_T in TPC + TOF detectors in $0-5\%$ Au + Au collisions. (b) The second-order SFM as a function of number of partitioned cells from UrQMD calculations.

efficiency into the UrQMD event sample by keeping a particle according to the probability reading from Fig. 2.4(a) with the p_T of that particle. And the measured $F_2(M)$ is calculated in the event sample after discarding particles. Next, we apply the correction formula of Eq. (2.3) to do the efficiency correction on the measured $F_2(M)$. In Fig. 2.4(b), the black circles represent the original true $F_2(M)$, the blue solid triangles are the measured $F_2(M)$ after discarding particles according to the TPC efficiency, and the red stars show the efficiency corrected SFMs by using the cell-by-cell method. It is observed that the measured SFMs (blue triangle) are systematically smaller than the original true ones (black circles), especially in the large number of partitioned cells. However, the efficiency corrected SFMs (red stars) are found to be well consistent with the original true ones.

For the case of TPC+TOF efficiencies, Fig. 2.5(a) shows the tracking efficiencies as a function of p_T in TPC and TOF. We apply the TPC+TOF efficiency effect to the UrQMD event sample at $\sqrt{s_{\mathrm{NN}}}$ = 19.6 GeV and then correct the measured SFMs by Eq. (2.3). The results are shown in Fig. 2.5(b). Again, the SFMs corrected by the proposed cell-by-cell method (red stars) are verified to be coincide with the original true ones (black circles).

Chapter 3

The RHIC-STAR Experiment

3.1 Relativistic Heavy Ion Collider (RHIC) at BNL

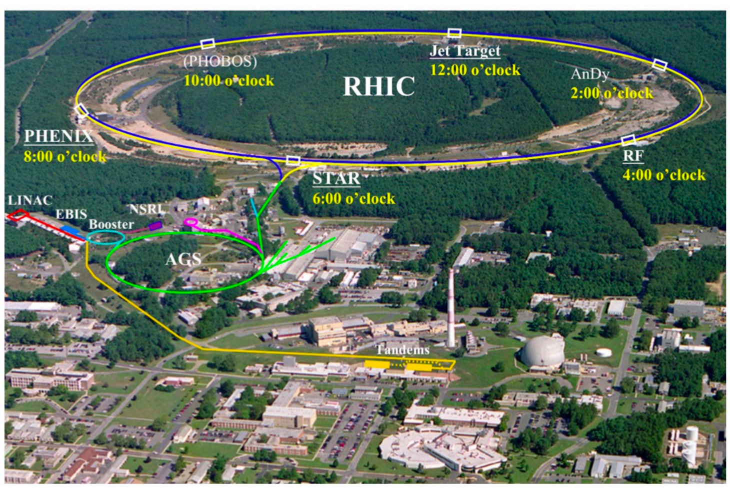

Figure 3.1: Schematic of the Relativistic Heavy Ion Collider (RHIC) complex at Brookhaven National Laboratory . Figure taken from Refs. [95, 96].

The Relativistic Heavy Ion Collider (RHIC) at Brookhaven National Laboratory (BNL), is a world-class particle accelerator where physicists are exploring the most fundamental forces and properties of QGP matter [95]. It was the first machine in the world capable of colliding heavy ions. The primary objective of RHIC is to investigate this phase transition and to study the formation and property of QGP [96].

RHIC was completely constructed in 1999 and began the first physics program in 2000. Over last two decades, RHIC has been successfully accelerated and collided different beam species: $p+p, p+Al, p+Au, He+Au, Cu+Cu, Cu+Au, Au+Au, U+U$. The top energy for heavy-ion beams (e.g., for Au ions) is 100 GeV per beam and that for protons is 250 GeV.

Figure 3.1 shows the layout of RHIC. RHIC has two completely independent rings and two sources of ions. The acceleration scenario for ions beam at RHIC is simply described as following. At first, negatively charged gold ions were partially stripped of their electrons and accelerated to the energy of 1 MeV at Tandem. Then beams of gold ions are delivered to the Booster Synchrotron and accelerated to 95MeV. Next, ions were stripped again at Booster and injected to the AGS that accelerated ions to the energy of 10.8 GeV. At last, ions were fully stripped and transferred to RHIC rings through the AGS-to-RHIC Beam Transfer Line. More details about acceleration scenario can be found in Refs [96].

RHIC has two major detectors (STAR and PHENIX) and two minor ones (PHOBOS and BRAHMS), equivalently, four interaction points. The STAR experiment is at 6 clock, the PHENIX experiment is at 8 clock, the PHOBOS experiment is at 10 clock and the BRAHMS experiment is at 2 clock. Currently, only the STAR experiment is ongoing to operate collision and other experiments have completed their task.

3.2 The STAR Experiment

The Solenoidal Tracker at RHIC (STAR) is one of two large detector systems constructed at the RHIC. The STAR was designed primarily for measurements of hadron production over a large solid angle, featuring detector systems for high precision tracking, momentum analysis,

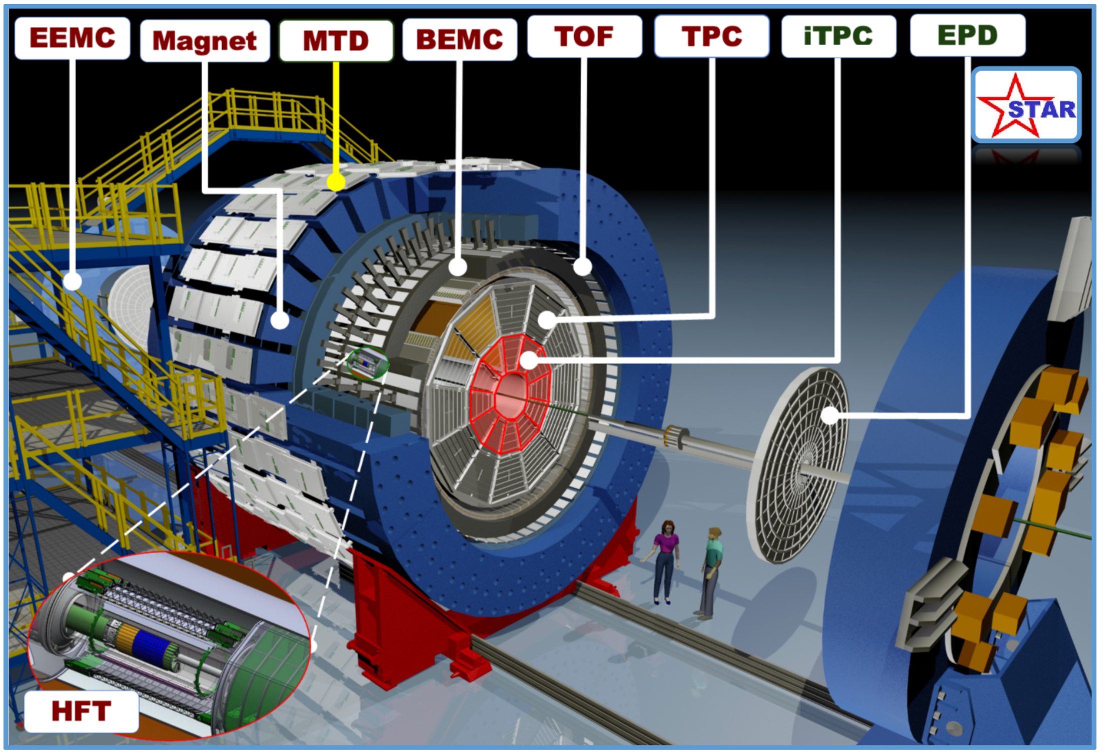

Figure 3.2: The 3D piture of the STAR detector. Figure taken from Ref. [97].

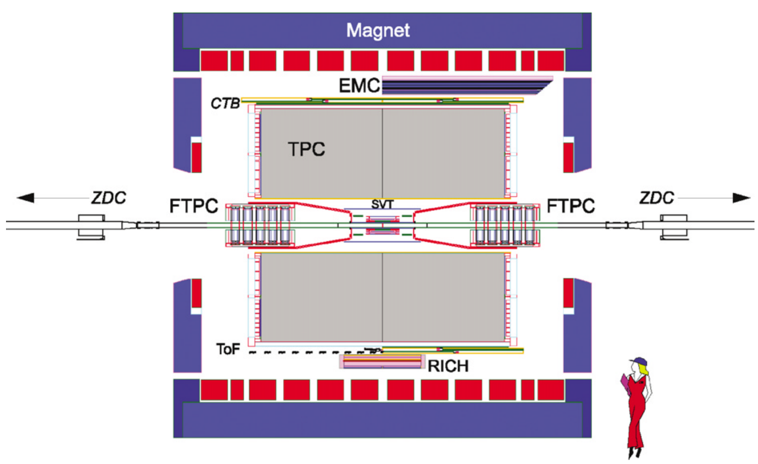

Figure 3.3: Cutaway side view of the STAR detector. Figure taken from Ref. [98].

and particle identification. The large acceptance of STAR maked it particularly well suited for event-by-event characterizations of heavy ion collisions [98].

Fig. 3.2 shows the layout of the STAR experiment, and a cutaway side view of the STAR detector is shown in Fig. 3.3. There are two main sub-detectors: Time Projection Chamber (TPC) and Time of Flight (TOF), to record the collisions in the STAR experiment. In the following analysis, the TPC detector combined with the TOF detector are used to measure momentum message and identify particle species, and we therefore discuss the TPC and TOF detectors in detail.

3.2.1 Subsystem: Time Projection Chamber (TPC) Detector

The STAR's 'heart' is the Time Projection Chamber (TPC) detector which tracks and identifies particles producing in heavy-ion collisions. Its acceptance covers $|\eta| < 1$ through through the full azimuth angle. Particles, over a momentum range from 100 MeV/c to greater than 1 GeV/c, are identified by measuring their ionization energy loss (dE/dx).

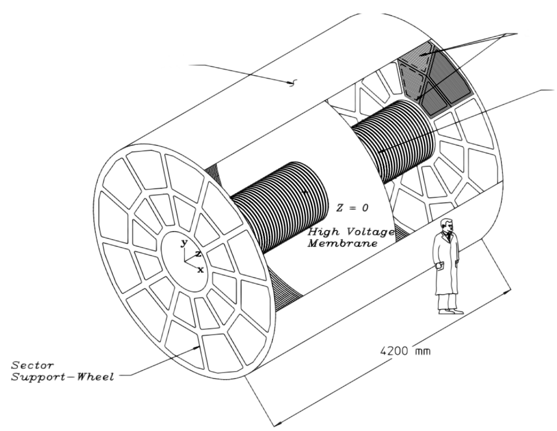

Figure 3.4: The STAR TPC detector surrounds a beam–beam interaction region. The collisions take place near the TPC center. Figure is taken from Ref. [99].

Figure 3.4 shows the crude structure of TPC detector. The TPC was 4.2 m long and 4 m in diameter. It was an empty volume of gas in a well-defined, uniform, electric field of ≈ 135 V/cm. The magnetic field in TPC was 0.5 T. The TPC was filled with P10 gas (10% methane, 90% argon) whose primary attribute was a fast drift velocity. The transverse diffusion in P10 gas was 230 μm/ $\sqrt{cm}$ at 0.5 T, and free electrons drifted at a steady speed around 5.45 cm/μ.

The readout system was based on Multi-Wire Proportional Chambers (MWPC) with readout pads. The readout modules, or sectors, were arranged as on a clock with 12 sectors around the circle. The track of a particle passing through the TPC was reconstructed by finding ionization cluster. There were total 45 pad rows to record the hit point ionization clusters. The clusters were found in separately in x, y, z place, which the x and y of a cluster were determined by the charged on adjacent pads row, and the z coordinate was given by measuring the time of drift of a cluster. To extract the momentum information, the tracking software fit the points on a track. Finally, The transverse momentum (p_T) of a track was determined by fitting a circle through the x, y coordinates of the vertex and the points along the track. In addition, the total momentum was calculated using this radius of curvature and the angle that the track makes with respect to the z-axis of the TPC.

The (dE/dx) of a particle was extracted from the energy loss measured on up to 45 pad rows, identifying particle species in the TPC. Experimentally, only 70% of the pad rows were performed to calculate the average $(< dE/dx >)$. For a given charged particle, it's dE/dx can be described by the Bethe-Bloch function as follows:

$$-\frac{dE}{dx} = Kz^2\frac{Z}{A}\frac{1}{\beta^2}(\frac{1}{2}ln\frac{2m_ec^2\beta^2\gamma^2T_{max}}{I^2} - \beta^2 - \frac{\delta}{2}) \tag{3.1}$$

where $K = 0.3071\frac{MeV}{g/cm^2}$ is a constant, z is the charge of the particle, Z is the atomic number of absorb, I is the average ionization energy of the material, δ is a correction based on the electron density and T_{max} is the maximum kinetic energy.

Figure 3.5 shows the measured dE/dx as a function of (p/q) in Au+Au collision at $\sqrt{s_{NN}} = 39$ GeV from the STAR experiment. In this Fig. 3.5, the colored dashed lines represent the theoretical values given by Eq. (3.1) for different charged particles. Experimentally, the criteria for particle identification is determined by a new observable $n\sigma$:

$$n\sigma = \frac{1}{R} log \frac{(dE/dx)_{measured}}{(dE/dx)_{Bishsel}} \tag{3.2}$$

where $R = 0.55$ is the relative energy resolution in TPC. The $n\sigma$ following a Gaussian distribution, describe how far a measured track always from theoretically expected value. Generally, a appropriate cut of $|n\sigma| < 2$ is applied to judge particle species in data analysis. In Fig. 3.5, we can see that TPC is able to separate kaon (pion) and protons up to $p \approx 1$ GeV/c, and poins and kaons up to 0.7 GeV/c.

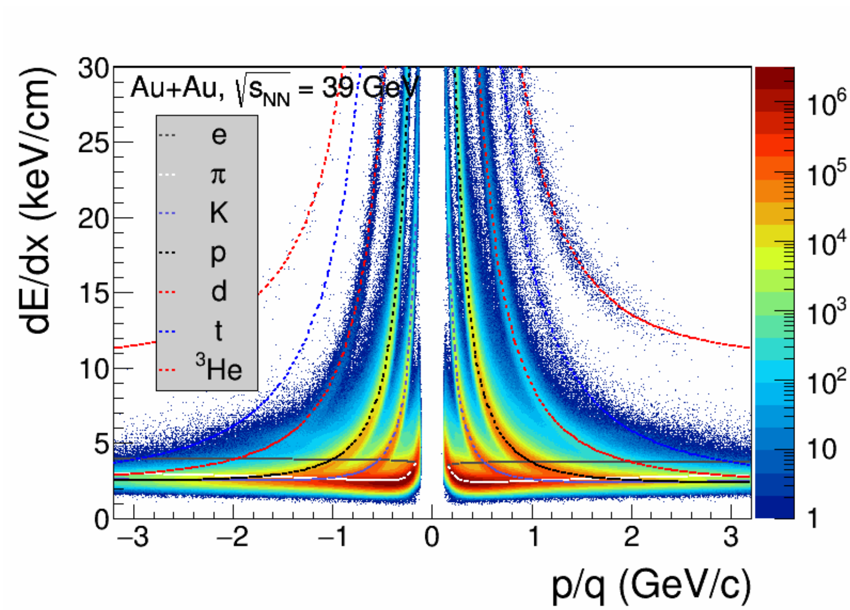

Figure 3.5: Energy loss dE/dx as a function of rigidity (p/q) in Au+Au collisions at $\sqrt{s_{NN}}$ = 39 GeV measured by the TPC detector. The colored dashed lines represent the theoretical values for different charged particles.

3.2.2 Subsystem: Time of Flight Detector (TOF) Detector

A full barrel Time-of-Flight (TPC) detector was proposed to extend the particle identification to high momentum, since the particle identification in the TPC was limited at low momentum [100, 101]. The TOF detector was based on the Multi-gap Resistive Plane Chamber (MRPC) which was basically a stack of resistive plates with a series of uniform gas gaps [101]. The TOF consists of 120 trays of MRPC modules that covered the entire acceptance of the TPC detector. There were a total of 3800 MRPC modules with 23000 readout channels. The main features of the proposed arrangement was to achieve a timing resolution of at least 100 ps.

The TOF detector determines charged particle velocity by measuring the time required to travel from the interaction point to the time of flight detector, or between two detectors. The 'start' time (t_{start}) was measured by Vertex position detectors (VPD) that always 5.4m from the TPC center, and the 'stop' time (t_{stop}) was read out by the TCPU card in the TOF system. Hence, the time intervals is $\Delta t = t_{stop} - t_{start}$. Furthermore, the TPC provided the momentum (p), and total path length (s). Therefore, the inverse velocity, $1/\beta$, for each track, is calculated by:

$$1/\beta = c\Delta t/s \tag{3.3}$$

where c is the speed of light. Then, the track momentum measured by the TPC detector and the associated velocity allowed the calculation of the particle mass, m, via:

$$m^2 = \frac{p^2}{(\beta\gamma)^2} = p^2[\frac{(c\Delta t)^2}{s^2} - 1] \tag{3.4}$$

Shown in Fig. 3.6 is the particle mass via the TOF for pions, kaons, protons, as labelled, versus the rigidity (p/q) in Au+Au collisions at $\sqrt{s_{NN}}$ = 39 GeV. The white dash lines represent the rest mass for different particles species. As we can see, the TOF detector will extend capability for kaons (pions) separation from 0.6 to 1.7 GeV/c, the range for proton separation will be increased from 1 to 3 GeV/c. By combining the information from the TPC and TOF detectors, we can measure pions, kaons, protons and so on, in the high p_T range, which is crucial to many measurements.

In the following analysis, TPC particle identification is performed using the measured energy loss, with $K^{\pm}$ and $\pi^{\pm}$ requiring a momentum range $0.2 < p_T < 0.4$ GeV/c, and p and $\bar{p}$ requiring a momentum range $0.4 < p_T < 0.8$ GeV/c. Moreover, mass squared from the TOF detector is used for particle identification, with $K^{\pm}$ and $\pi^{\pm}$ requiring a momentum range of $0.4 < p_T < 1.6$ GeV/c, and p and $\bar{p}$ requiring a momentum range of $0.8 < p_T < 2.0$ GeV/c.

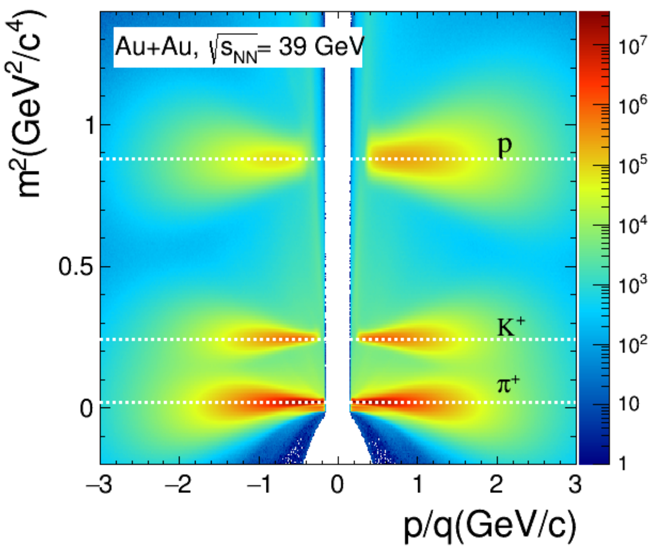

Figure 3.6: Mass (m^2) as a function of rigidity (p/q) in Au+Au collisions at $\sqrt{s_{NN}} = 39$ GeV measured by the TOF detector. The dashed lines represent the rest mass for proton, kaons and pions, respectively.

Chapter 4

Analysis Details of the STAR Data

4.1 Data Sets

The experimental data presented here were measured by the STAR detector from the first phase of Beam Energy Scan (BES) program RHIC. Those were Au+Au collisions at $\sqrt{s_{\mathrm{NN}}}$ = 7.7, 11.5, 14.5,19.6, 27, 39, 54.4, 62.4 and 200 GeV. In table 4.1, we show the basic information about production message for the STAR data.

4.2 Event Selection

4.2.1 Selection Cuts

In present analysis, we select minimum bias trigger events with a z-coordinate (V_z) of primary vertex within ± 30 cm for most of the colliding systems and energies, from the center of the TPC along the beam line. This ensures uniformity of detector efficiency and ideal detector coverage. The range of $|V_z|$ is chosen to optimise the event statistics and uniformity of the response of the detectors. In order to reject background events which involve interactions with the beam pipe, the transverse radius (V_r) of the event vertex is required to be within 2 cm (1

$\sqrt{s_{\mathrm{NN}}}$ **(GeV)**	**Year**	**Trigger ID**	**Production**	**# of Events(M)**
7.7	2010	290001, 290004	P10ih	3.2
11.5	2010	310014	P10ih	6.8
14.5	2014	440005, 440015, 440006, 440016	P14ii	13.1
19.6	2011	340001, 340011, 340021	P11id	16.2
27	2011	360001	P11id	32.2
39	2010	280001	P10ih	89.3
54.4	2017	580021	P18ic	441.7
62.4	2010	270001, 270011, 270021	P10ik	46.7
200	2010	260001, 260011, 260021, 260031	P10ik	236

Table 4.1: Basic information for the data sets.

cm for 14.5 GeV) of the center of STAR detector. To remove pile-up events at $\sqrt{s_{\mathrm{NN}}}$ = 39, 54.4, 62.4 and 200 GeV, we require the V_z difference between the two methods to be within 3 cm. In table 4.2, we show the event selection cuts for all energies.

In Fig. 4.2 and Fig. 4.3, we show the event selection cuts for $\sqrt{s_{\mathrm{NN}}}$ = 39 GeV.

<table>
<tr><th>$\sqrt{s_{\mathrm{NN}}}$ (GeV)</th><th>V_z (cm)</th><th>V_r (cm)</th><th>$\lvert\mathrm{Vpd}V_z - V_z\rvert$ (cm)</th></tr>
<tr><td>7.7</td><td>$\lvert V_z\rvert < 50$</td><td rowspan="2">< 2</td><td rowspan="5">nan</td></tr>
<tr><td>11.5</td><td rowspan="8">$\lvert V_z\rvert < 30$</td></tr>
<tr><td>14.5</td><td>< 1</td></tr>
<tr><td>19.6</td><td rowspan="6">< 2</td></tr>
<tr><td>27</td></tr>
<tr><td>39</td><td rowspan="4">< 3</td></tr>
<tr><td>54.4</td></tr>
<tr><td>62.4</td></tr>
<tr><td>200</td></tr>
</table>

Table 4.2: Basic event cuts for the data sets.

4.2.2 Bad Runs

To ensure the quality of our data, one need a run by run study of several variables to remove the bad runs. Run-by-Run QA was already done and bad runs at BES I energies are given from official StRefMultCorr. Events were selected on the run-by-run variables: average Refmult, Refmult2, V_z, V_r, DCA, p_T, ϕ, η and remove the outlier runs beyond $+/-3\sigma$, as shown in Fig.4.4.

4.2.3 Pile-up Events

Pile-up event is the event that contains more than one single-collision events [102]. It is formed when the detector identifies two or more single-collision events as an event, since those

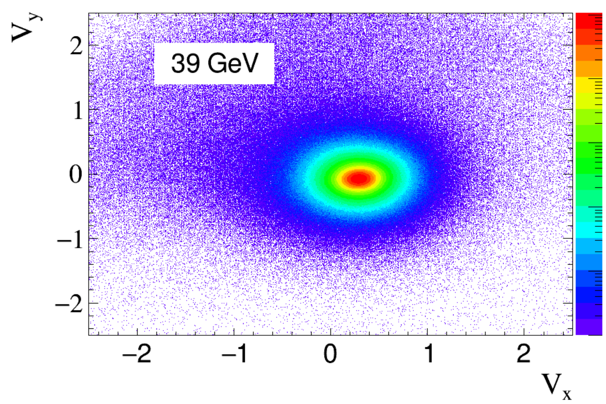

Figure 4.1: V_x Vs. V_y distribution in Au + Au collision at $\sqrt{s_{\mathrm{NN}}}$= 39 GeV.

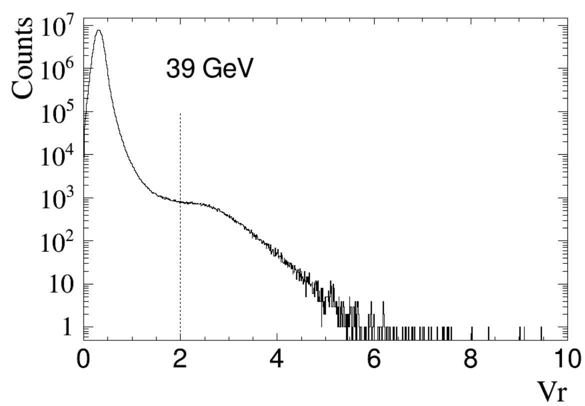

Figure 4.2: V_r distribution in Au + Au collision at $\sqrt{s_{\mathrm{NN}}}$= 39 GeV.

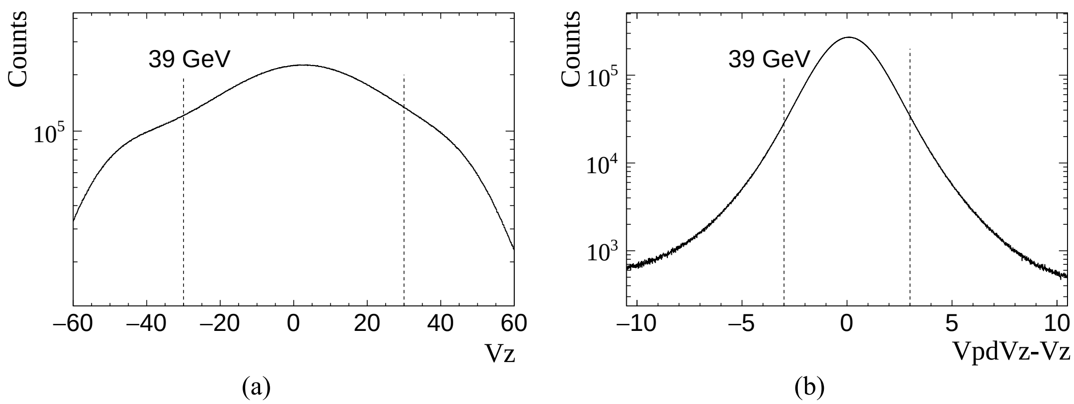

Figure 4.3: (a) V_z distribution in Au + Au collision at $\sqrt{s_{\rm NN}}$ = 39 GeV. (b) $VpdV_z - Vz$ distribution. The dash line represent the value of cut.

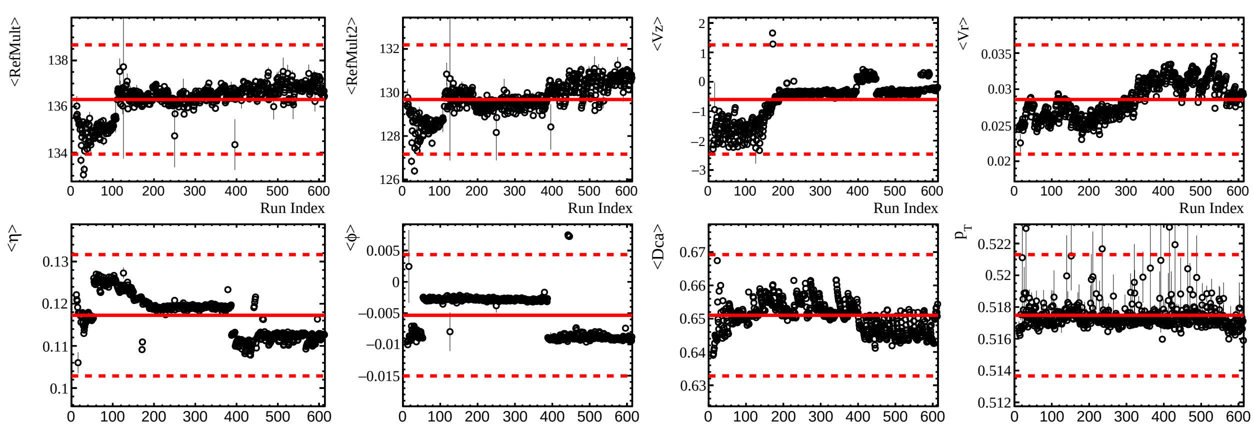

Figure 4.4: Run by Run QA of event level quantities, Refmult, Refmult2, V_z, V_r, DCA, p_T, ϕ, η for trigger 580021 and 580001 at $\sqrt{s_{\rm NN}}$ = 54 GeV.

single-collision events are produced within a small time and space interval. The multiplicity of pile-up events are the combination of those from two or more single-collision events, and therefore it has a oblivious tail shown in the reference multiplicity distribution. The unexpected pile-up events must be removed by some 2D-plot cuts.

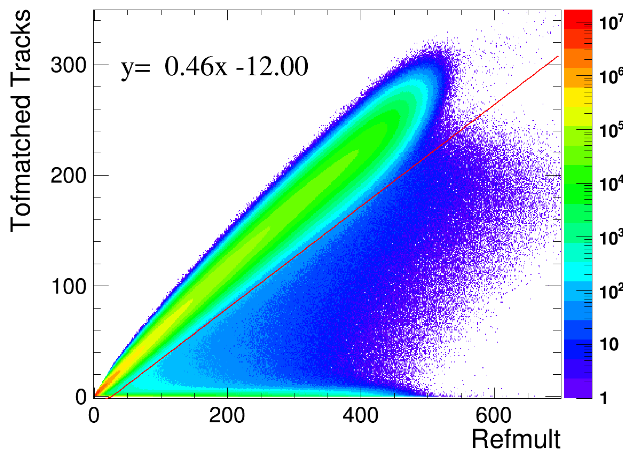

Figure 4.5: nToFmatch Vs. Refmult $\sqrt{s_{\mathrm{NN}}}$ = 54 GeV.

Pile-up events cuts are applied in this analysis and based on 2D plots.

1. nToFmatch Vs. Refmult. Some TPC tracks are not matched to the TOF, that is out of time pile-up events. It is defined as the primary tracks counts in $|\eta| < 1$ as:

If($|\eta| < 0.5$&&dca<3&&nFitHits>10&&ToFmatchflag>0) nToFmatch++;

2. Beta-tofmatch Vs. Refmult. In some events, TPC tracks are matched to the TOF detector, but the beta (v/c, velocity) is not correctly calculated. It is defined as:

If($|\eta| < 1$&&dca<3&&nFitHits>10&&beta>0.1) beta-tofmatch++;

Figures 4.5 and 4.6 show the 2D plots for $\sqrt{s_{\mathrm{NN}}}$ = 54 GeV. The pile-up event cuts at this collision energy are:

if(nToFfmatch<=1||(nToFfmatch<0.46×refmult-12)) continue;

if(beta-tofmatch<=0||(beta-tofmatch<0.88×refmult-25.96)) continue;

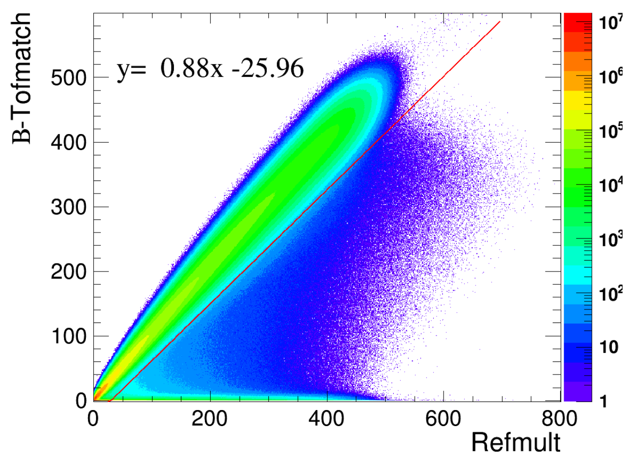

Figure 4.6: Beta-tofmatch Vs. Refmult at $\sqrt{s_{\mathrm{NN}}}$ = 54 GeV .

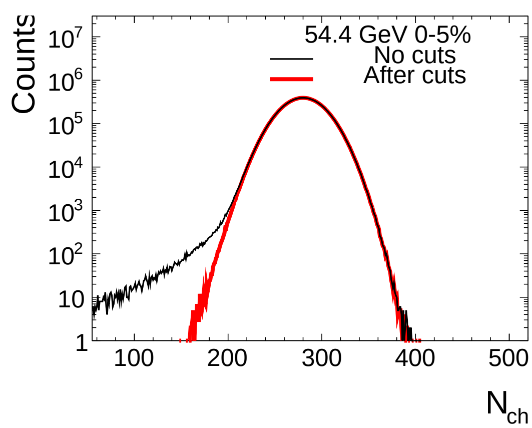

Figure 4.7: N_{ch} distribution in 0-5% at $\sqrt{s_{\mathrm{NN}}}$ = 54.4 GeV.

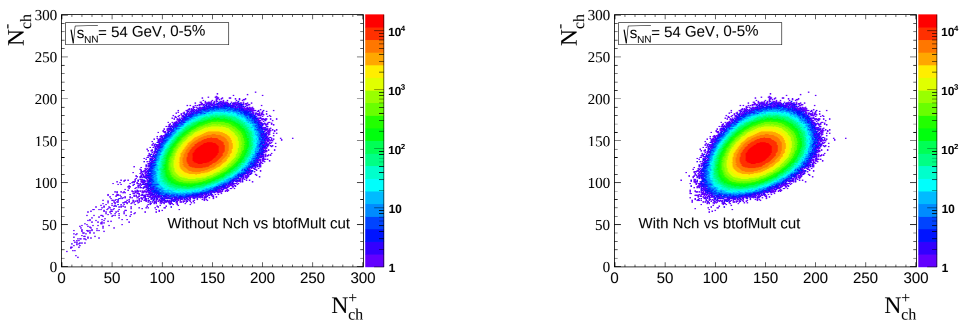

(a) (b)

Figure 4.8: (a) Without using N_{ch} Vs.btofTrayMultiplicity cut in analysis, the N^+_{ch} vs. N^+_{ch} plot in the most central Au+Au collisions at $\sqrt{s_{\mathrm{NN}}}$= 54.4 GeV. (b) With using N_{ch} Vs. btofTrayMultiplicity cut in analysis, the N^+_{ch} vs. N^+_{ch} plot in the most central Au+Au collisions at $\sqrt{s_{\mathrm{NN}}}$= 54.4 GeV.

Besides, for $\sqrt{s_{\mathrm{NN}}}$= 54.4-200 GeV, it was found that there is tail in lower values of N_{ch} distribution as shown as the black line in Fig. 4.7, the N_{ch} is the charge multiplicity of a event which after event selection in table 4.2 and track selection in table 4.4 within the windows $0.2 < p_T < 2.0$ GeV and $|\eta|$ <0.5. To remove the tail, we have two cuts in Refmult Vs. btofTrayMultiplicity plot and N_{ch} Vs. btofTrayMultiplicity plot, as show in Fig. 4.9 and 4.10, respectively. The tail is mainly removed by the N_{ch} Vs. btofTrayMultiplicity cut. Moreover, we found that the left tail of N_{ch} distribution was mainly caused by events which have lower N^+_{ch} and N^-_{ch} multiplicity as show in Fig 4.8 (a). We can see that some data points are outed of the main zone in the N^+_{ch} Vs. N^-_{ch} plot in Fig 4.8 (a), and these events can be removed by the N_{ch} Vs. btofTrayMultiplicity cut as shown in Fig 4.8 (b).

It's worthwhile to note that the effect of tail on the scaling exponent is little, since the scaling exponent is 0.3934±0.0030 when the the N_{ch} Vs. btofTrayMultiplicity cut is not applied, while scaling exponent is 0.3903±0.0031 when the cut is applied. Although the change on scaling exponent is small, we still need to discard these unexpected events. The cuts for

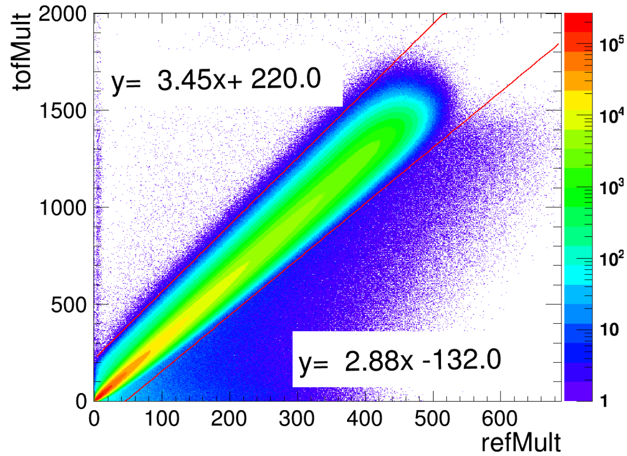

Figure 4.9: Refmult Vs. btofTrayMultiplicity at $\sqrt{s_{\mathrm{NN}}}$= 54.4 GeV.

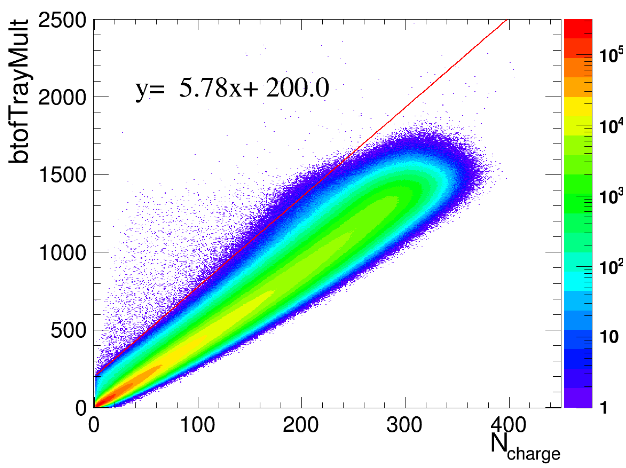

Figure 4.10: N_{ch} Vs. btofTrayMultiplicity at $\sqrt{s_{\mathrm{NN}}}$= 54.4 GeV.

removing the tail at $\sqrt{s_{\mathrm{NN}}}$= 54.4 are listed below:

if(btofTrayMultiplicity $>$ (3.45$\times$refMult+222)) continue;

if(btofTrayMultiplicity $<$ (2.88$\times$refMult-132.2)) continue;

if(btofTrayMultiplicity $>$ (5.78$\times N_{ch}$+200)) continue;

4.3 Collision Centrality

The collision centrality is the degree of overlapped region between the two nuclei in nucleus-nucleus collision. Generally, the collision centrality is characterized by different quantities. A commonly used quantity is the impact parameter b, which is defined as the distance between the geometrical centers of the colliding nuclei in the plane transverse to their direction [33, 103], as show in Fig 4.11. In addition, the number of participant nucleons (N_{part}) and the number of binary collisions (N_{coll}), are also used to characterize the collision centrality. Unfortunately, those geometrical variables cannot be directly measured in experiment. However, the impact parameter b is monotonically related to charged-particle multiplicity (N_{ch}) which can be easily measured in experiment. Therefore, the collision centrality is usually determined by a comparison between experimental measured particle multiplicity and Glauber Monte Carlo simulations [33, 103].

The Glauber model, a Monte Carlo approach, is a multiple collision model that treats an nucleus-nucleus collision as an independent sequence of nucleon-nucleon collisions [103]. This model is used to calculate geometric quantities (N_{part}, N_{coll}) for a fixed impact parameter (b) which characterize the collision centrality. Figure 4.12 shows the relationship betwen N_{part} (N_{coll}) and b in Au+Au and Cu+Cu collisions at $\sqrt{s_{\mathrm{NN}}}$= 200 GeV from the Glauber model.

In Fig. 4.13, it is shown how to define a collision centrality by comparing the particle multiplicities with Glauber Monte Carlo simulation and the correlation between the N_{ch} and the Glauber-calculated quantities b and N_{part}. For events with large b, their N_{ch} is low and N_{part} is small, whereas N_{ch} is high and N_{part} is large for events with small b. In the simplest case, the events with large N_{ch} is determined to be central collision events, otherwise they will

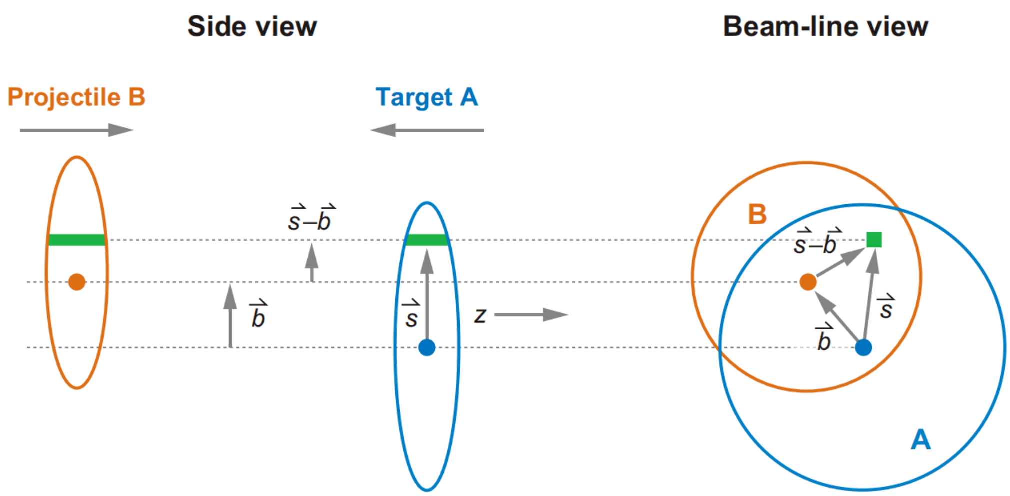

Figure 4.11: Two heavy ions, target A and projectile B, are shown colliding at relativistic speeds with impact parameter b. Figure taken from Ref. [103].

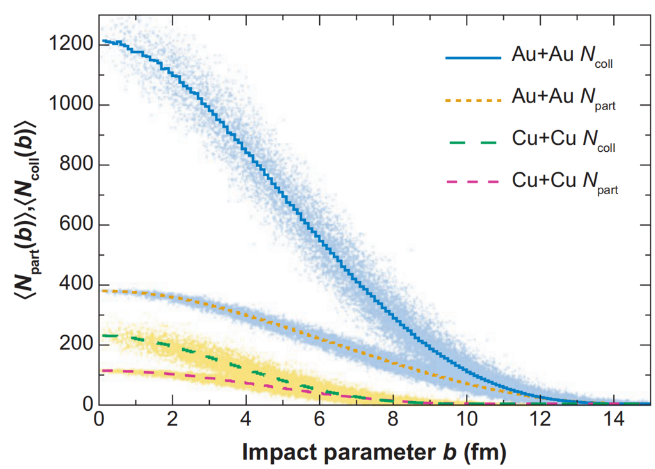

Figure 4.12: Average number of participants N_{part} and binary nucleon-nucleon collisions N_{coll} in the Glauber Monte Carlo calculation, as a function of the impact parameter b. Figure taken from Ref. [103].

be peripheral events. Once the total integral of the experimental measured N_{ch} distribution is known, centrality classes are defined by binning the N_{ch} distribution on the basis of the fraction of the total integral, and is denoted as a percentage value (e.g., 0–5, 5–10%, 10-20%...), as shown by the dash lines in Fig. 4.13. In this way, we can calculate the N_{ch} from experiment and determine the centrality classes with Glauber model simulations.

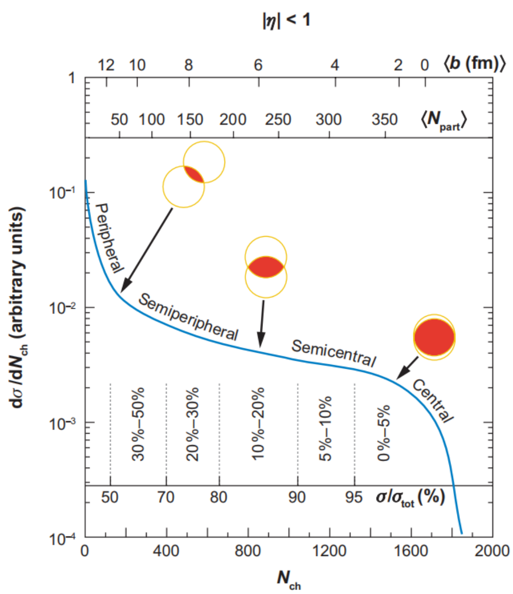

Figure 4.13: An illustrated example of the correlation of the final-state-observable total inclusive charged-particle multiplicity N_{ch} with Glauber-calculated quantities, such as, b and N_{part}. Figure taken from Ref. [103].

The charged-particle density $dN_{ch}/d\eta$ near mid-rapidity is well described by a two-component model, expressed as:

$$\frac{dN_{ch}}{d\eta} = n_{pp}[(1-x)N_{part} + xN_{coll}] \tag{4.1}$$

where n_{pp} is the average multiplicity in $p+p$ collisions, x is the fraction of the hard component, the N_{part} and N_{coll} can be obtained from the Glauber model.

The multiplicity distribution was simulated on the basis of a convolution of the N_{part}

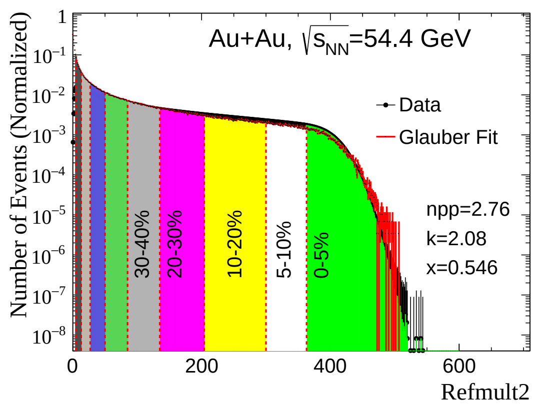

Figure 4.14: The Refmult2 distribution in Au+Au collisions at $\sqrt{s_{\mathrm{NN}}}$ = 54 GeV. The black circles represent the experimental data, and red solid line represent the Glauber MC simulation with negative binomial distribution. The vertical dashed lines represent different centrality classes.

distribution from a Glauber Monte Carlo simulation and an Negative Binomial Distribution (NBD). The multiplicity (n) distribution was assumed to follow an NBD:

$$P_{NBD}(n_{pp}, k; n) = \frac{\tau(n+k)}{\tau(n+1)\tau(k)} \frac{(n_{pp}/k)^n}{(n_{pp}/k+1)^{n+k}} \tag{4.2}$$

where τ is the gamma function, the n_{pp} and k are treated as free parameters in the simulation. Then, the multiplicity distribution was simulated for a grid of values for n_{pp}, k, and x to find the minimum λ^2/DOF comparing between the measured N_{ch} and Glauber simulated one.

Figure 4.14 show the reference multiplicity 2 (Refmult2) distribution at $\sqrt{s_{\mathrm{NN}}}$ = 54 GeV from STAR data (black circles) and Glauber MC simulation (red solid line). The discrepancy at small Refmult2 is due to low detector efficiency in the peripheral collisions (80-100%). The Refmult2 from Glauber MC simulation is used to determine the centrality class. In Fig. 4.14, the dash red lines represent the nine centrality cuts from 0-5%, 5-10% … 70-80%, obtained by binning the Refmult2 distribution on the basis of the fraction of the total integral.

To avoid self-correlation [46, 104], the centrality is determined from Refmult2 within a pseudo-rapidity window of $0.5 < |\eta| < 1$, chosen to be outside the analysis window of $|\eta| < 0.5$. Finally, we list the Refmult2 cuts for centrality definition at $\sqrt{s_{\mathrm{NN}}}$ = 7.7-200 GeV, in table 4.3.

$\sqrt{s_{\mathrm{NN}}}$(GeV)	0-5%	5-10%	10-20%	20-30%	30-40%	40-50%	50-60%	60-70%	70-80%
7.7	165	137	95	64	41	25	14	7	3
11.5	206	172	118	80	52	32	18	9	4
14.5	225	188	129	87	57	35	20	10	5
19.6	258	215	149	100	65	40	22	12	5
27	284	237	164	111	71	43	25	13	6
39	307	257	179	121	78	47	27	14	6
54.4	363	300	204	135	85	50	27	13	5
62.4	334	279	194	131	84	51	29	15	7
200	421	355	247	167	108	65	37	19	9

Table 4.3: Centrality bins for Refmult2 at $\sqrt{s_{\mathrm{NN}}}$ = 14.5 GeV and 54.4 GeV

4.4 Track Selection and Particle Identification (PID)

To reduce the contamination from secondary charged particles, only primary particles have been selected, requiring a distance of closest approach (DCA) to the primary vertex less

$\lvert\eta\rvert$	< 0.5
No. of fit points	> 20
No. of dE/dx points	> 5
No . of fit points/ No. of possible hints	> 0.52
DCA	< 1

Table 4.4: Track quality used in BES I energies.

Protons, Kinematic Cuts	**PID Cuts**
$0.4 < p_T < 0.8\,(\mathrm{GeV}/c)$ $p < 1$ (GeV/c)	**TPC**, $\lvert n\sigma_p\rvert < 2$
$0.8 < p_T < 2.0\,(\mathrm{GeV}/c)$ $p < 3$ (GeV/c)	**TPC+TOF**, $\lvert n\sigma_p\rvert < 2$, $0.6 < m^2 < 1.2$ (GeV$^2/c^4$)

Table 4.5: Particle identification selections for protons

Kaons, Kinematic Cuts	**PID Cuts**
$0.2 < p_T < 0.4$ GeV/c	**TPC**, $\lvert n\sigma_K\rvert < 2$
$0.4 < p_T < 1.6$ GeV/c	**TPC+TOF**, $\lvert n\sigma_K\rvert < 2$, $0.14 < m^2 < 0.4$ (GeV$^2/c^4$)

Table 4.6: Particle identification selections for kaons

Pions, Kinematic Cuts	**PID Cuts**
$0.2 < p_T < 0.4$ GeV/c	**TPC**, $\lvert n\sigma_\pi\rvert < 2$
$0.4 < p_T < 1.6$ GeV/c	**TPC+TOF**, $\lvert n\sigma_\pi\rvert < 2$, $-0.15 < m^2 < 0.14$ (GeV$^2/c^4$)

Table 4.7: Particle identification selections for pions

than 1cm. Track must have at least 20 points (NFitPoints) used in track fitting out of maximum of 45 hits possible in the TPC detector. The minimum number of points used to derive dE/dx values is limited to 5. To prevent multiple counting of split tracks, at least 52% of the total possible fit points are required (NHitsFit/NFitPoss). Track selection cuts for all energies are listed in table 4.4, and Fig. 4.15 shows the NFitPoints distribution and DCA distribution.

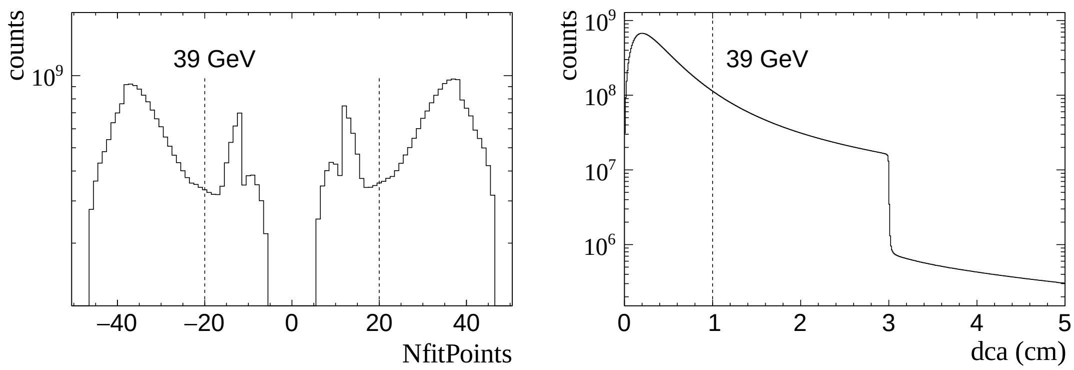

Figure 4.15: (a) NFitPoints distribution in Au + Au collision at $\sqrt{s_{\rm NN}}$ = 39 GeV. (b) DCA distribution in Au + Au collision at $\sqrt{s_{\rm NN}}$ = 39 GeV. The dash line represent the value of cut.

These long-lived particles ($\pi^{\pm}, K^{\pm}, p, \bar{p}$) can be directed identified by using both energy loss information from the TPC detector and time of flight information from the TOF detector. The identification capability of TPC and TOF can be found in Fig. 3.5 and 3.6. In Fig. 3.5, we can see that the pions and kaons have good separation when the momentum is less than 0.6 GeV. In Fig. 3.6, the particle has good separation with other according to their m^2. In our analysis, the associated TPC dE/dx information and TOF m^2 are used for pions, kaons and protons identification. Tables 4.5, 4.6 and 4.7 show the particle identification cuts for protons, kaons and pions, respectively.

4.5 Detector Efficiency

4.5.1 TPC Efficiency

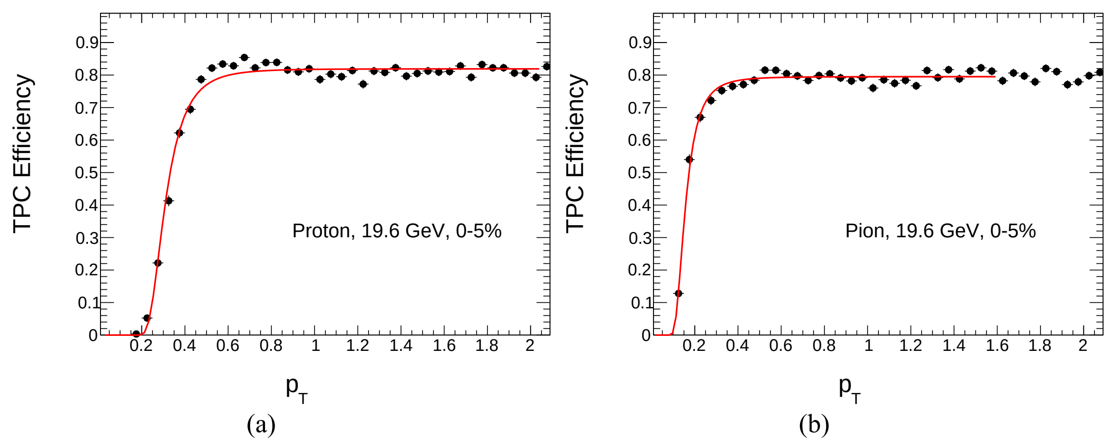

Figure 4.16: (a) p_T dependence of the embedding efficiency for proton at $\sqrt{s_{\mathrm{NN}}}$ = 19.6 GeV. The red line is the fitting function according to Eq. (4.2). (b) p_T dependence of the embedding efficiency for pion at $\sqrt{s_{\mathrm{NN}}}$ = 19.6 GeV.

In real case, as we don't have 100% detector efficiency (include acceptance), we need to estimate the effect of the detector efficiency on the observable. The TPC efficiencies as a function of transverse momentum for identified particles can be calculated from the embedding simulation.

$$\epsilon(p_T) = \frac{N_{RC}(p_T)}{N_{MC}(p_T)}, \tag{4.1}$$

where N_{RC} and N_{MC} represent the number of reconstruct track and Monte Carlo tracks, respectively. Figure 4.16 shows the TPC efficiency as a function of p_T, which is well fitted by the function:

$$y = p_0 e^{-(\frac{p_1}{x})^{p_2}} \tag{4.2}$$

4.5.2 TOF Efficiency

The TOF matching efficiency is calculated using a data driven method and can be calculated as:

$$\epsilon(p_T) = \frac{\text{The number of TOF matched track (MatchFlag} > 0\text{, Track cuts, } |Nsigma| < 2)}{\text{The number of TPC tracks (Track cuts, } |Nsigma| < 2)}. \tag{4.3}$$

Figure 4.17 shows the p_T dependence of the TOF match efficiency for protons and pions.

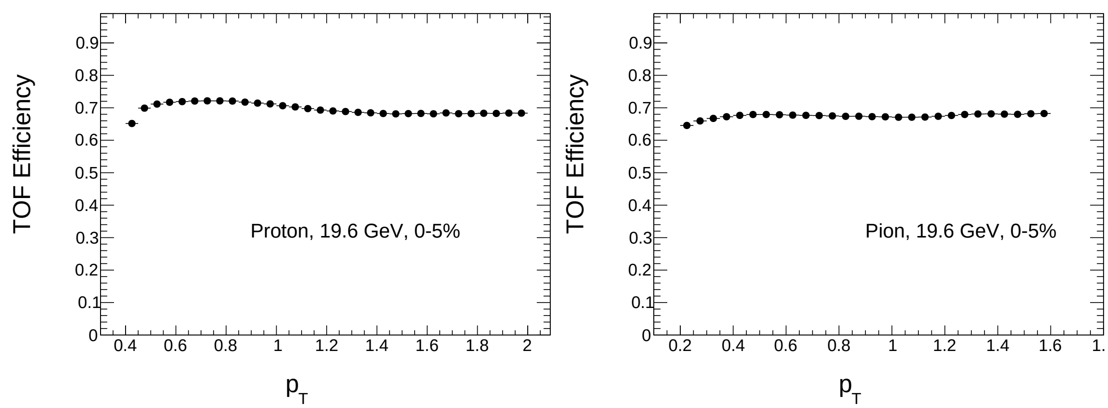

(a) (b)

Figure 4.17: (a) p_T dependence of the TOF efficiency for proton at $\sqrt{s_{\rm NN}}$ = 19.6 GeV. (b) p_T dependence of the TOF efficiency for pion at $\sqrt{s_{\rm NN}}$ = 19.6 GeV.

4.5.3 TPC+TOF Efficiency

The particle identification method is different between low- and high-p_T regions. The TPC detector is used to obtain momentum of charged particles and do the particle identification in low-p_T region. Moreover, the TOF detector is used to do the particle identification in the relatively-high-p_T region. In this case, particles need to be counted separately for the two p_T

regions, in which the values of the efficiencies are different. Based on different PID method used in low p_T and relatively-high-p_T region, thus we have efficiencies at two p_T regions as show in Fig. 4.18 and Fig. 4.19.

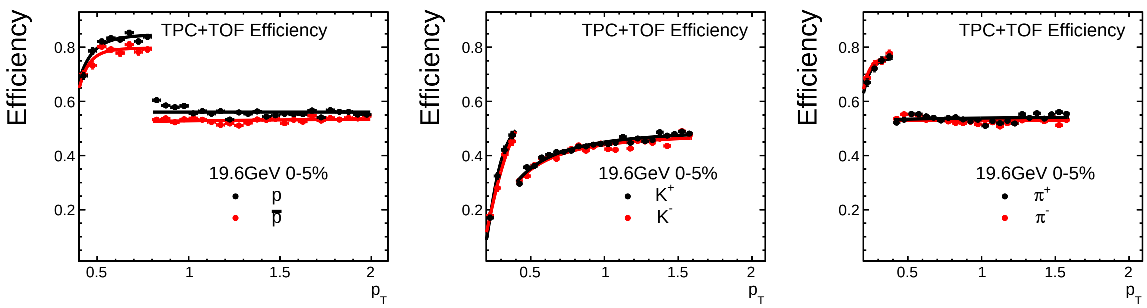

Figure 4.18: TPC+TOF efficiency as a function of p_T for protons, kaons and pions in 0-5% collisions at $\sqrt{s_{\rm NN}}$ = 19.6 GeV. The solid lines represent the fitting function according to Eq. (4.2) at two p_T regions.

4.6 Systematic Uncertainty

To estimate systematic uncertainty, we varied 3 track cuts including dca, NFitHit, NSigma and different fit range for the number of cells M^2. The DCA mainly controls the fraction of background which are knocked out from the beam pipe by other particles. The selection of a sufficiently large number of fit points can suppress track splitting in the TPC. The purity of the charged hadron samples can be controlled by the $n\sigma$ variable of the ionization energy loss. Table 4.8 shows the DCA, NFitPoints and $n\sigma$ are used to estimate the systematic error.

The default cuts used in the analysis are: DCA<1, NFitPoints>20, $|b\sigma|<2$, When we vary one of the cut, the other cuts stick to the default value. For example, the systematic errors

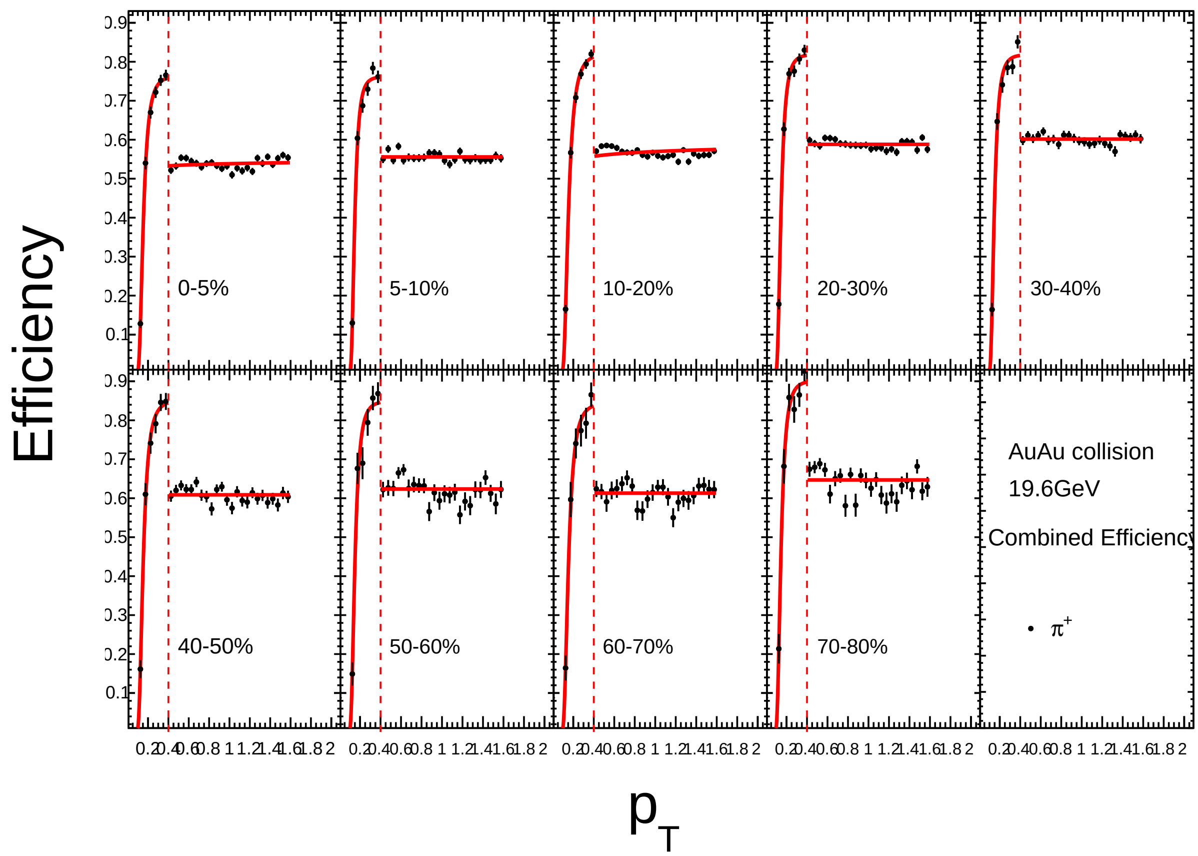

Figure 4.19: TPC+TOF efficiency as a function of p_T for pion in different centralities at $\sqrt{s_{NN}}$ = 19.6 GeV. The red lines represent the fitting function according to Eq. (4.2) at two p_T regions

DCA	0.8	0.9	1.0	1.1	1.2
NfitPoint	15	18	20	22	25
NSigma	1.6	1.8	2.0	2.2	2.4

Table 4.8: Systematic cuts for DCA, NFitPoint and NSigma (protons, kaon and pions)

from one kind of cut can be calculated as:

$$Error = \sqrt{\frac{1}{n}\sum_{i=1}^{n}(cut_i - def.)^2}. \tag{4.1}$$

Thus, the total systematic errors are calculated as:

$$Sys\_err = \sqrt{Err(DCA)^2 + Err(NFit)^2 + Err(NSigma)^2 + Err(M^2)^2}. \tag{4.2}$$

Here the $Err(M^2)$ denotes the systematic errors from the different fit range of M^2. For each set of the cuts, we can calculate the point by point difference between the varied cuts and the default cut.

Chapter 5

Results from the STAR Experiment

The results presented here are obtained from the Au + Au collisions at $\sqrt{s_{\mathrm{NN}}}$ = 7.7, 11.5, 14.5, 19.6, 27, 39,54.4, 62.4 and 200 GeV in the first phase of the BES program at RHIC. We measure the SFMs of identified charged hadrons ($h^{\pm}$) combining p, $\bar{p}$, $K^{\pm}$, and $\pi^{\pm}$ together. Particle identification is required in order to apply the efficiency correction on the SFMs. The domain $[-p_{x,max}, p_{x,max}]\otimes$ $[-p_{y,max}, p_{y,max}]$ of the transverse momentum plane with $p_{x,max} = p_{y,max} =$ 2.0 GeV/c is partitioned into M^2 cells to calculate the SFMs according to Eq. (1.6). Statistical uncertainty of $F_q(M)^{data}$ and $F_q(M)^{mix}$ are estimated using the Bootstrap method, and statistical uncertainty of $\Delta F_q(M)$ is calculated by $Err(\Delta F_q(M)) = \sqrt{Err(F_q(M)^{data})^2 + Err(F_q(M)^{mix})^2}$

5.1 Efficiency Corrected and Uncorrected SFMs

Figure 5.1 shows the efficiency corrected $F_2(M)$ Vs. uncorrected $F_2(M)$, it is observed that both the values of $F_2(M)^{data}$ and $F_2(M)^{mix}$ are become smaller than uncorrected values.

Also, the corrected $\Delta F_2(M)$ is smaller than uncorrected $\Delta F_2(M)$. Figure 5.2 shows the same case for the sixth-order SFM.

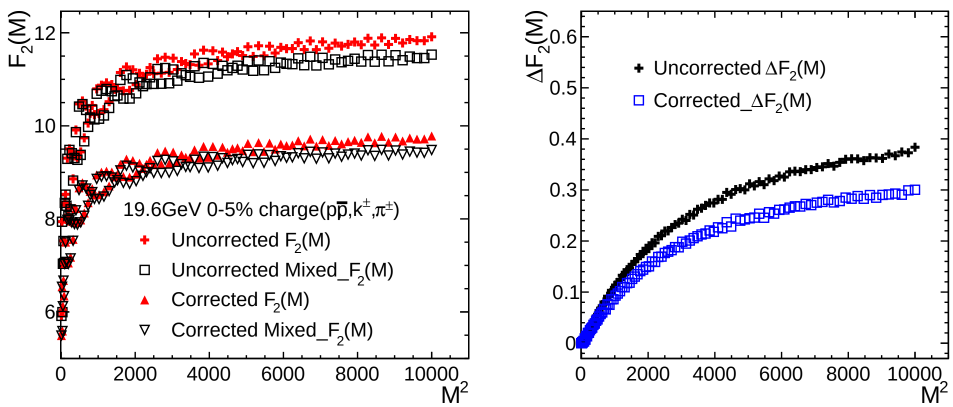

Figure 5.1: (Left) Efficiency corrected $F_2(M)$ Vs. uncorrected $F_2(M)$ for data and mixed events in 0-5% central collision at $\sqrt{s_{\mathrm{NN}}}$ = 19.6 GeV. (Right) Efficiency corrected $\Delta F_2(M)$ Vs. uncorrected $\Delta F_2(M)$

5.2 Energy Dependence of SFMs in Au + Au collisions

Figure 5.3 and Fig. 5.4 show $F_q(M)^{data}$ and $F_q(M)^{mix}$ corrected for reconstruction efficiency, from the second order to the sixth order, in the 0-5% central collision and 10-40% central collision, respectively. Based on the statistic of BES-I data, the calculation of $F_q(M)$ can be performed in the range of M^2 from 1 to 100^2 and up to the sixth order (q=6). In Fig. 5.3, red marks represent $F_q(M)$ of original data while black marks represent $F_q(M)$ of associated mixed events. Error bars of $F_q(M)^{data}$ and $F_q(M)^{mix}$ were obtained from the Bootstrap method. It is observed that all order of $F_q(M)^{data}$ are larger than $F_q(M)^{mix}$ at large M^2 region at all $\sqrt{s_{\mathrm{NN}}}$, therefore, a deviation of $\Delta F_q(M)$ from zero is present in central Au + Au collisions. $F_q(M)^{data}$ was observed to overlap with $F_q(M)^{mix}$ and $\Delta F_q(M) \approx 0$ from the

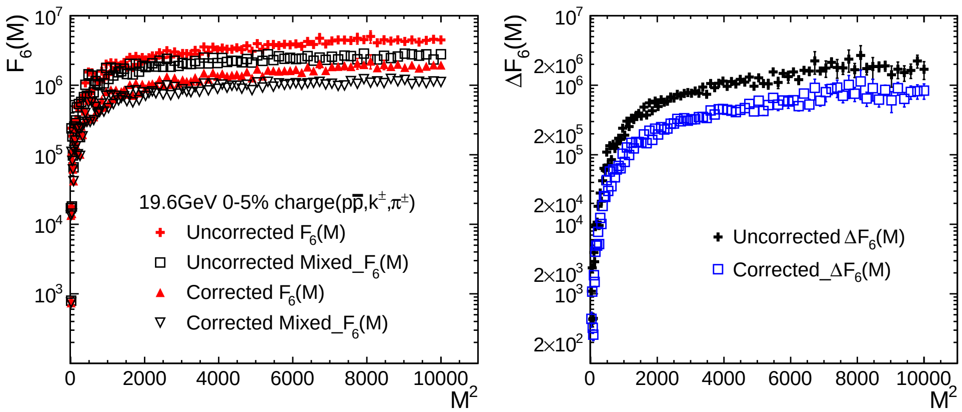

Figure 5.2: (Left) Efficiency corrected $F_6(M)$ Vs. uncorrected $F_6(M)$.(Right) Efficiency corrected $\Delta F_2(M)$ Vs. uncorrected $\Delta F_2(M)$

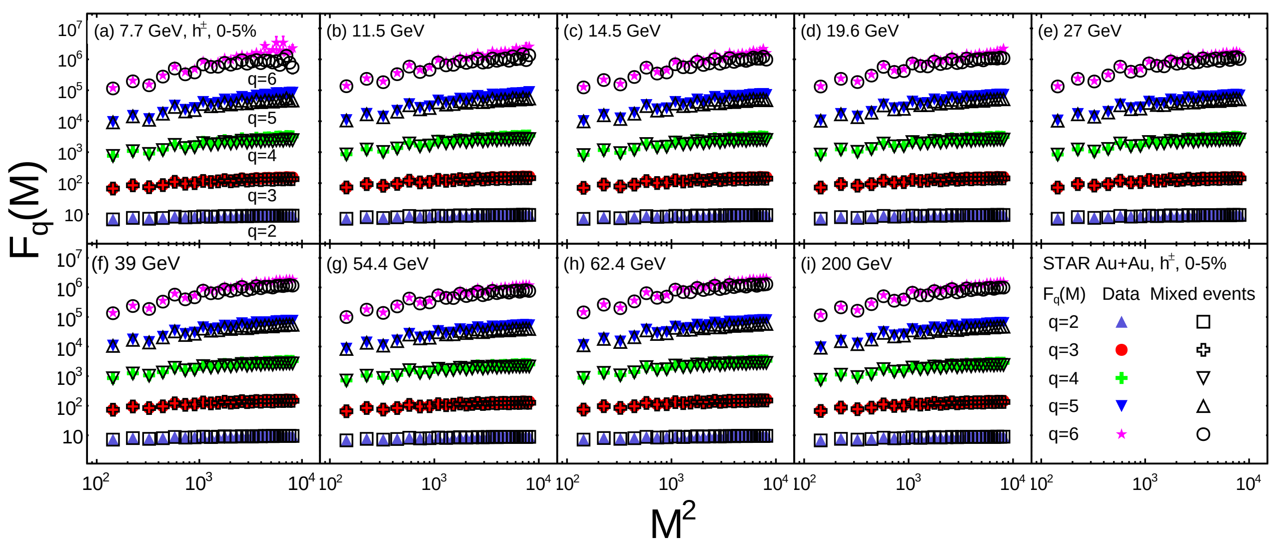

Figure 5.3: The scaled factorial moments, $F_q(M)$ ($q = 2 - 6$), from data and mixed events for charged hadrons in the most central(0-5%) Au + Au collisions at $\sqrt{s_{\mathrm{NN}}}$ = 7.7-200 GeV in double-logarithmic scale.

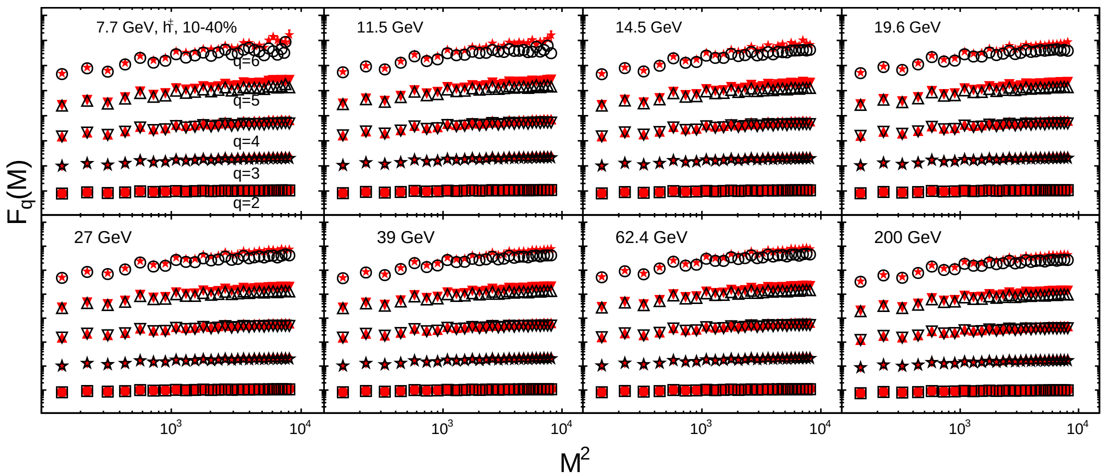

Figure 5.4: The scaled factorial moments, $F_q(M)$ $(q = 2-6)$, from data and mixed events for charged hadrons in central(10-40%) Au + Au collisions at $\sqrt{s_{\mathrm{NN}}}$ = 7.7-200 GeV in double-logarithmic scale.

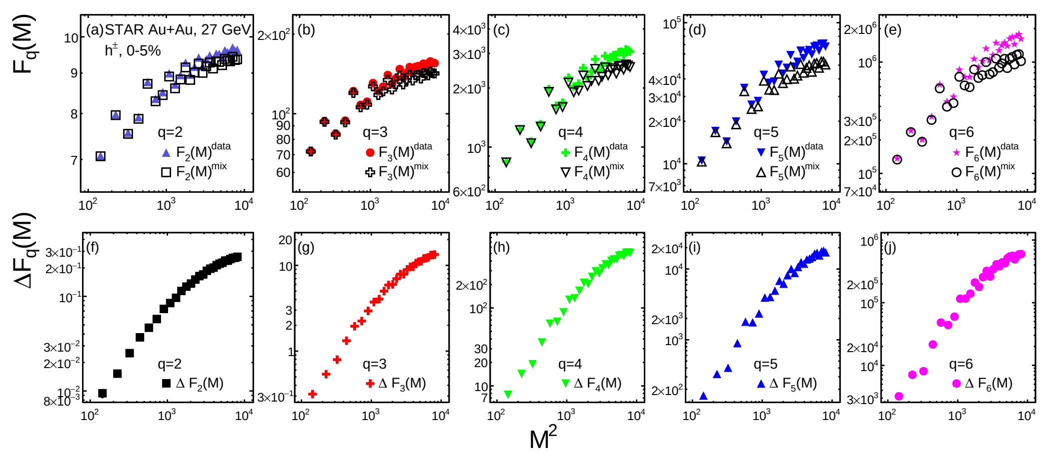

Figure 5.5: (a)-(e) $F_q(M)^{data}$ and $F_q(M)^{mix}$ for different order in the most central (0-5%) Au + Au collisions at $\sqrt{s_{\mathrm{NN}}}$ = 27 GeV in double-logarithmic scale. (f)-(j) $\Delta F_q(M)^{data}$ for different order in the most central (0-5%) Au + Au collisions at $\sqrt{s_{\mathrm{NN}}}$ = 27 GeV in double-logarithmic scale.

UrQMD calculations (see Sec. 6.1.3), which cannot describe the data presented here, since it does not incorporate any density fluctuations.

Figure 5.5 show $F_q(M)^{data}$, $F_q(M)^{mix}$ and $\Delta F_q(M)^{mix}$ as a function of M^2 for different order at $\sqrt{s_{\rm NN}}$ = 27 GeV. It is observed that all order of $F_q(M)^{data}$ are larger than $F_q(M)^{mix}$ at large M^2 region, therefore a deviation of $\Delta F_q(M)$ from zero is present in central Au + Au collisions.

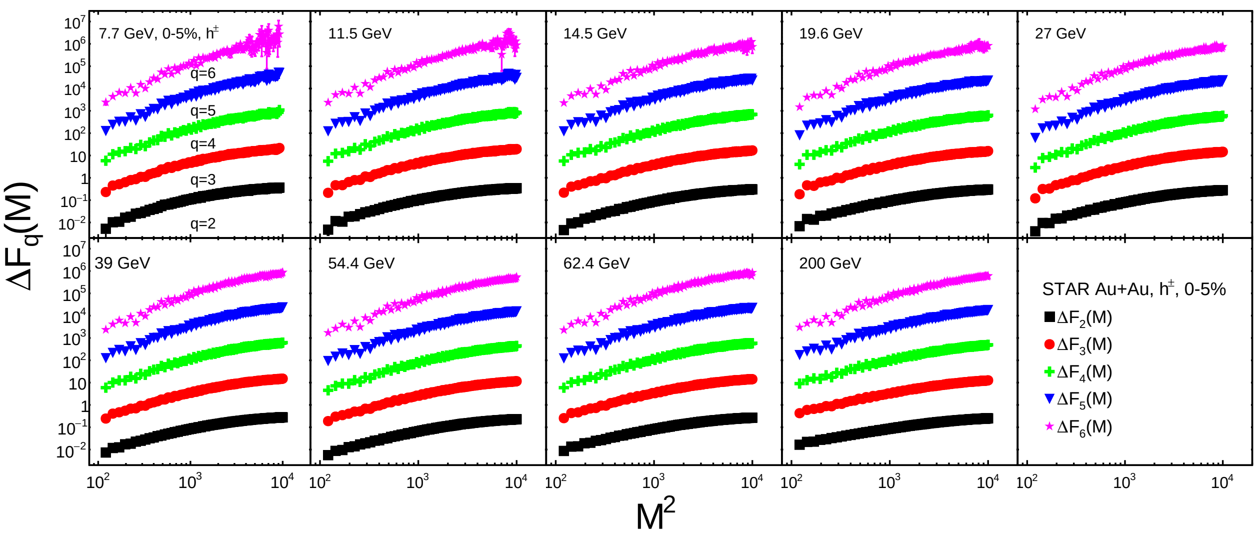

Figure 5.6: The $\Delta F_q(M)$ (up to sixth order) as a function of M^2 for the most central (0-5%) Au + Au collisions at $\sqrt{s_{\rm NN}}$ = 7.7-200 GeV in double-logarithmic scale.

Figure 5.6 and Fig. 5.7 shows the ΔF_q (q=2-6), calculated by Eq.(2.1), as a function of M^2 in 0-5% and 10-40% central collisions, respectively. We find that $\Delta F_q(M)$ (q = 2-6) increase with increasing M^2 and become saturated when M^2 is large ($M^2 > 4000$). Therefore, $\Delta F_q(M)$ (q = 2-6) does not obey a power-law behavior of $\Delta F_q(M) \propto (M^2)^{\phi_q}$ over the whole range of M^2. Equivalently, $\Delta F_q(M)$/M scaling is not valid for the whole range of M^2. The ϕ_q cannot be extracted in a reliable manner (independently of M^2 range) due to the absence of $\Delta F_q(M)/M$ scaling, therefore we focus on the power-law behavior of $\Delta F_q(M) \propto$

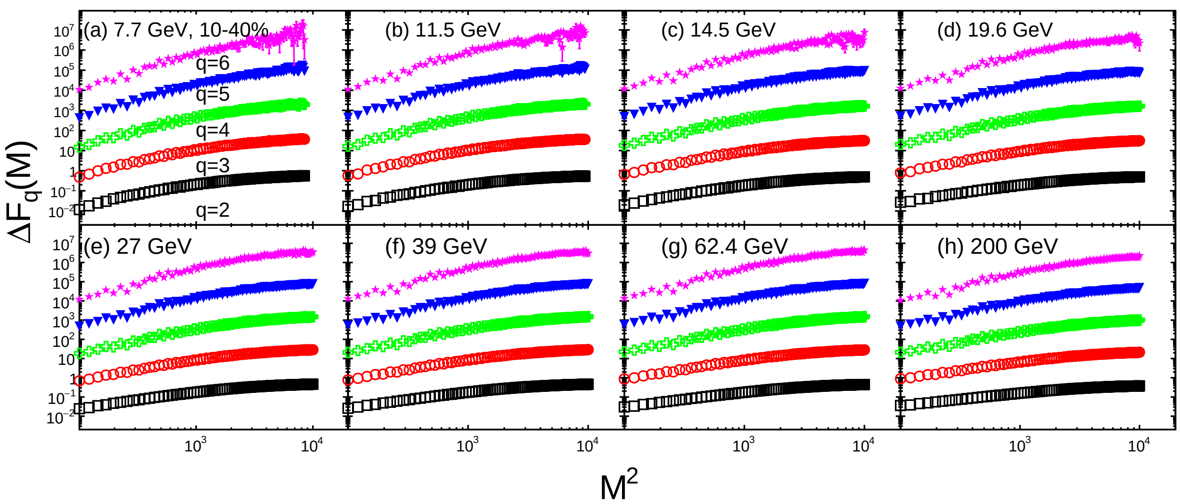

Figure 5.7: The $\Delta F_q(M)$ (up to sixth order) as a function of M^2 in 10-40% central Au + Au collisions at $\sqrt{s_{\mathrm{NN}}}$ = 7.7-200 GeV in double-logarithmic scale.

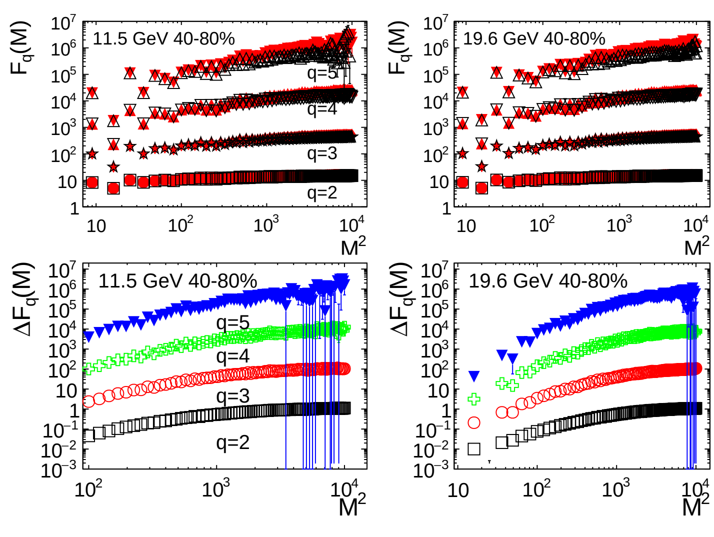

Figure 5.8: The $\Delta F_q(M)$ (up to the fifth order) as a function of M^2 in 40-80% central Au + Au collisions at $\sqrt{s_{\mathrm{NN}}}$ = 11.5 and 19.6 GeV in double-logarithmic scale.

$\Delta F_2(M)^{\beta_q}$ and the scaling exponent.

As for the $F_q(M)$ in peripheral Au + Au collisions, Fig. 5.8 show the $F_q(M)^{data}$, $F_q(M)^{mix}$ and $\Delta F_q(M)$ as a function of M^2 in 40-80% peripheral collisions at $\sqrt{s_{\rm NN}}$ = 11.5 and 19.6 GeV. We observe that almost four orders $\Delta F_q(M)(q = 2-5)$ can be calculated in 40-80% peripheral collisions while five orders can be calculated in central collisions. Since higher order $\Delta F_q(M)$ can't be calculated in peripheral collisions at lower energies, the β_q/q scaling can't be extracted in peripheral collisions.

5.3 Centrality Dependence of SFMs in Au+Au Collisions

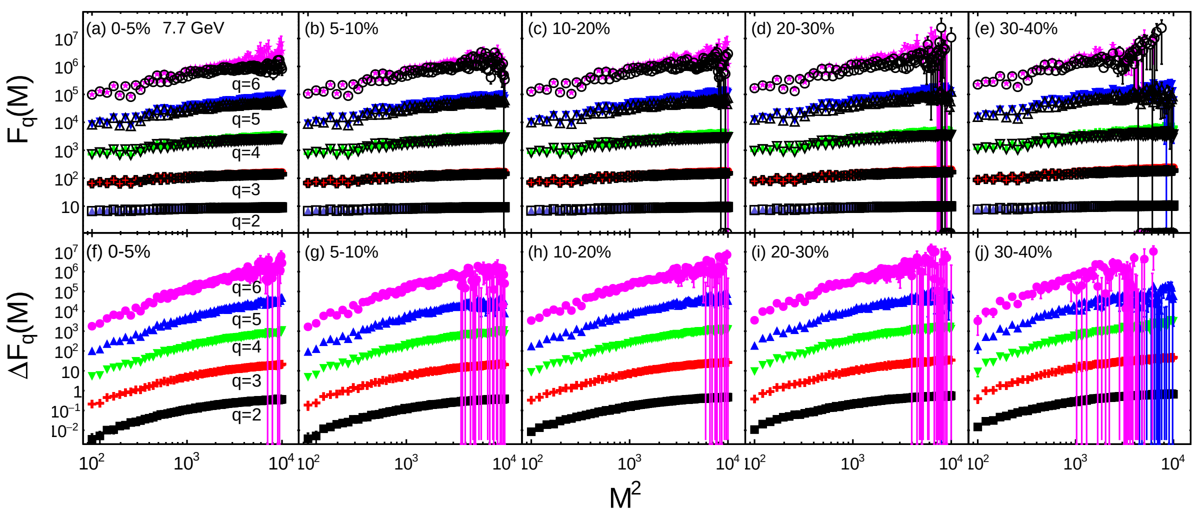

Figure 5.9: (a)-(e)$F_q(M)(q = 2-6)$, of identified charged hadrons ($h^{\pm}$) in 0-5%, 5-10%, 10-20%, 20-30%, 30-40% centralities at $\sqrt{s_{\rm NN}}$ = 7.7 GeV in double-logarithmic scale. Solid (open) markers represent $F_q(M)$ of data (mixed events) as a function of M^2. (f)-(j) $\Delta F_q(M)$ (q = 2-6) as a function of M^2 in these centralities at $\sqrt{s_{\rm NN}}$ = 7.7 GeV.

Figure 5.9 (a)-(e) shows the $F_q(M)^{data}$ and $F_q(M)^{mix}$ as a function of M^2 in in 0-5%, 5-10%, 10-20%, 20-30%, 30-40% centralities at $\sqrt{s_{\rm NN}}$ = 7.7 GeV. Fig. 5.9 (f)-(j) show

$\Delta F_q(M)$ (q = 2-6) as a function of M^2 in this five centralities. The $\Delta F_6(M)$ exhibits large statistical error for large M^2 from 5-10% to 10-40% centrality collision. Therefore the higher order $\Delta F_6(M)$ for large M^2 cannot be calculated except the most central collisions (0-5%). In the following calculation of scaling exponent, we will merge the 10-20%, 20-30%, 30-40% centrality bins to one centrality bin (10-40%) at lower collision energies. And the centrality dependence of scaling cannot be calculated for each centrality bin.

Figure 5.10 shows the centrality dependence of $F_q(M)^{data}$, $F_q(M)^{mix}$ and $\Delta F_q(M)$ (q = 2-6) at $\sqrt{s_{\rm NN}}$ = 19.6 GeV. In the 30-40% centrality at $\sqrt{s_{\rm NN}}$ = 19.6 GeV, there are only several data points of higher order $\Delta F_6(M)$ which have large statistical error. Therefore, we can calculate the scaling exponent from 0-5% central collision to 30-40% at $\sqrt{s_{\rm NN}}$ = 19.6 GeV. In the following analysis, we will calculate the centrality dependence of the scaling exponent when $\sqrt{s_{\rm NN}} \geq$ 19.6 GeV.

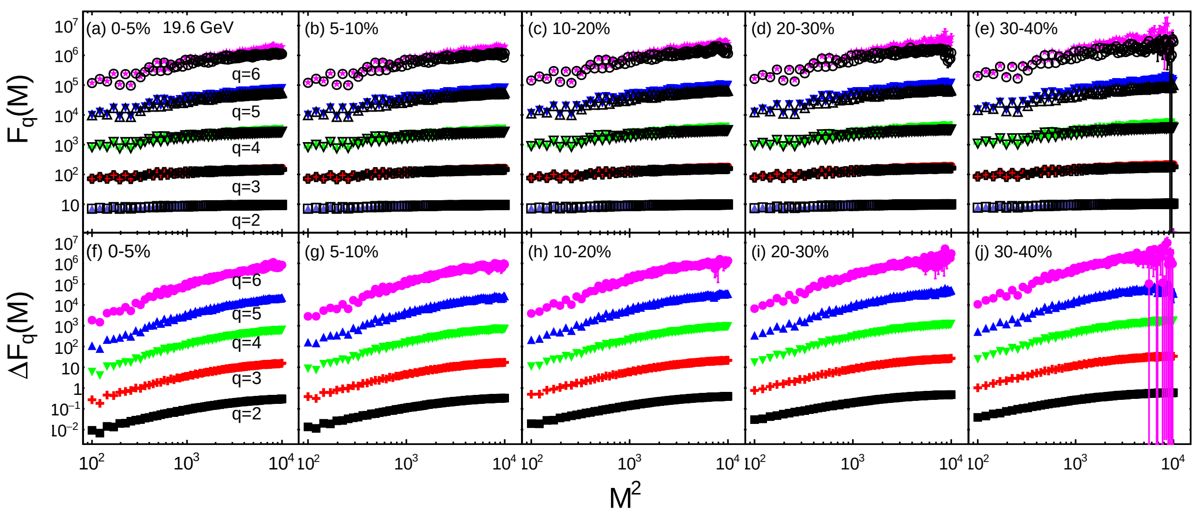

Figure 5.10: (a)-(e) $F_q(M)(q = 2-6)$, of identified charged hadrons ($h^{\pm}$) in 0-5%, 5-10%, 10-20%, 20-30%, 30-40% centralities at $\sqrt{s_{\rm NN}}$ = 19.6 GeV in double-logarithmic scale. Solid (open) markers represent Fq(M) of data (mixed events) as a function of M2. (f)-(j) $\Delta F_q(M)$ (q = 2-6) as a function of M^2 in these centralities at $\sqrt{s_{\rm NN}}$ = 19.6 GeV.

5.4 Mixed Events Method to Suppress Volume Fluctuation

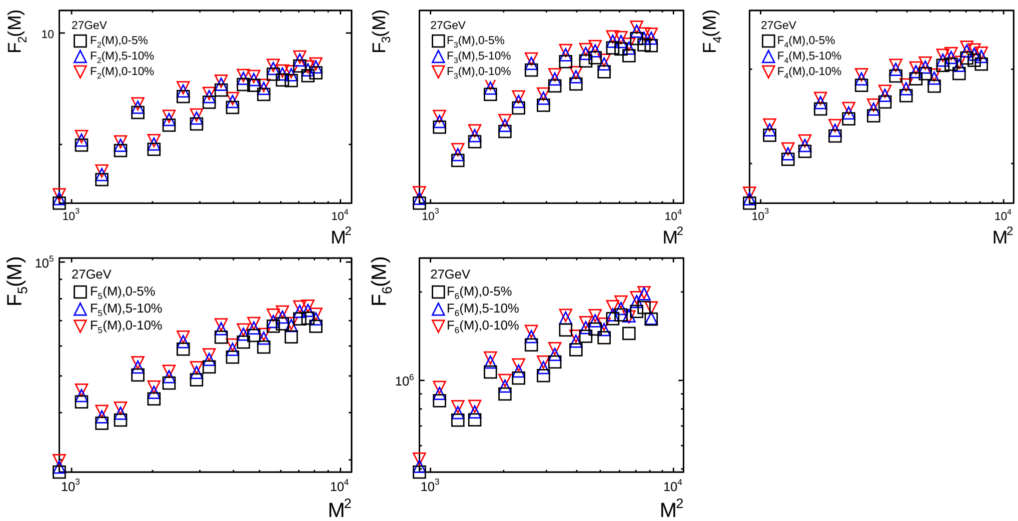

Figure 5.11: The $F_q(M)^{data}$ (up to the sixth order) as a function of M^2 in 0-5%, 5-10%, and 0-10% central Au + Au collisions.

In the cumulant analysis [46], it is known that calculating cumulants in such broad centrality bins leads to a strong enhancement of cumulants and cumulant ratios due to initial volume fluctuations. A Centrality Bin Width Correction (CBWC) can effectively suppress the effect of the volume fluctuations on cumulants within a finite centrality bin width. However, the CBWC could not applied to the $F_q(M)$ in the intermittency analysis since two main reasons: 1) One should perform the intermittency analysis only using $F_q(M)$ at larger M^2 region, and the calculations of $F_q(M)$ at larger M^2 region, especially for higher order, require enough event statistic. The events for a Refmult2 bin is too small to calculate $F_q(M)$ at larger M^2. 2) The computation time for $F_q(M)(q = 2-6)$ at different $M(1 \leq M \leq 100)$ is already very large, and it would require much longer time once we calculate $F_q(M)$ for each Refmult2 bin. 3) The rules of mixed events method also require enough statistic events.

In the intermittency analysis, the mixed event method is used to remove the possible effect

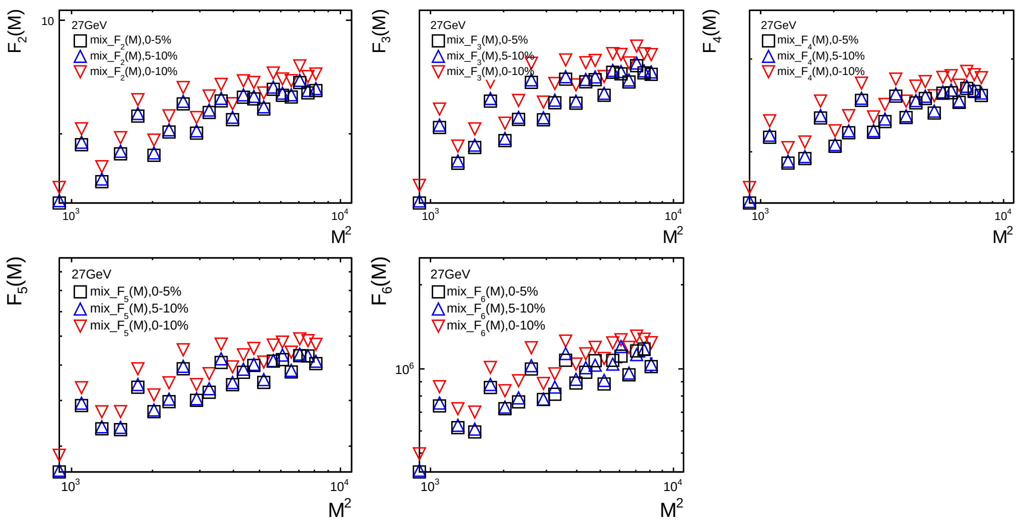

Figure 5.12: The $F_q(M)^{mix}$ (up to the sixth order) as a function of M^2 in 0-5%, 5-10%, and 0-10% central Au + Au collisions.

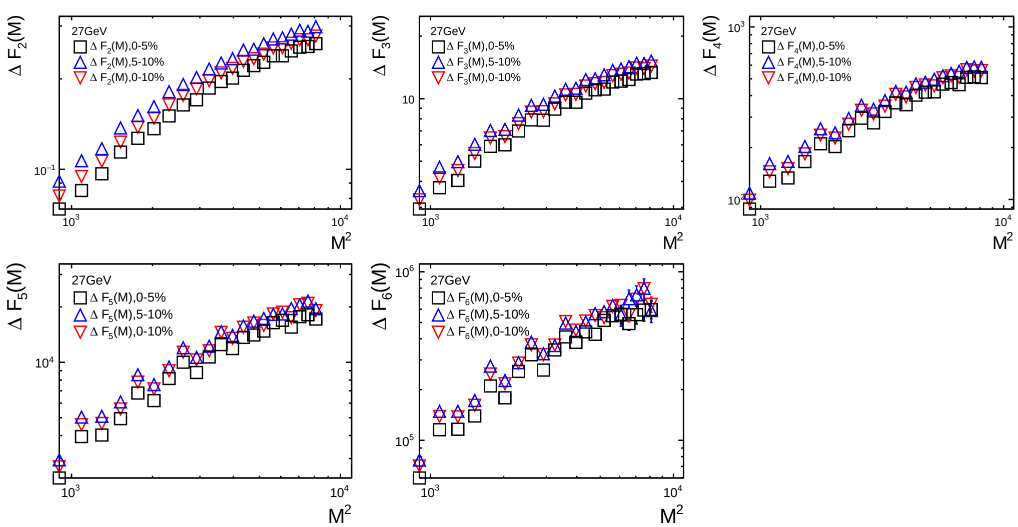

Figure 5.13: The $F_q(M)^{mix}$ (up to the sixth order) as a function of M^2 in 0-5%, 5-10%, and 0-10% central Au + Au collisions.

of the volume fluctuations belonged to one of trivial fluctuations or backgrounds. In Fig. 5.11, we can see the values of $F_q(M)^{data}$ in 0-10% centrality is larger than the values in 0-5% and 5-10%. Also, in Fig. 5.12, $F_q(M)^{mix}$ for 0-10% centrality is larger than the values 0-5% and 5-10%. However, as show in Fig. 5.13, the values of $\Delta F_q(M)$ which equal to $F_q(M)^{data} - F_q(M)^{mix}$, in 0-10% are smaller than the values in 5-10% and still larger than the values in 0-5%. Therefore, the mixed events method can effectively suppress the effect of the volume fluctuations for the $F_q(M)$ in the intermittency analysis.

5.5 Scaling Behavior of Higher-order SFMs on Second-order SFM

As discussion in Sec. 1.4.4, even if $\Delta F_q(M)/M$ scaling of $\Delta F_q(M) \propto (M^D)^{\phi_q}$ is not observed, the $\Delta F_q(M)/\Delta F_2(M)$ scaling of $\Delta F_q(M) \propto \Delta F_2(M)^{\beta_q}$ could still be visible in heavy-ion experiment. In Fig. 5.6, we haven't observe the $\Delta F_q(M)/M$ scaling. Next we draw the plots for the $\Delta F_q(M)/\Delta F_2(M)$ scaling.

In Fig. 5.14, we show $\Delta F_q(M)$ (q=2-6) as a function of $\Delta F_2(M)$ in most central (0-5%) collision at $\sqrt{s_{\mathrm{NN}}}$ = 7.7 GeV. It is note that we removed data points of $\Delta F_6(M)$ ($M > 80$) which have very large statistical error at $\sqrt{s_{\mathrm{NN}}}$ = 7.7 GeV. As we can see, in Fig 5.14 (b), the data points which have large error bars are removed. It's required that the value of $\Delta F_6(M)$ minus it's statistical error should larger than 2000, equivalently, $\Delta F_6(M) - Err(\Delta F_6(M)) > 2000$. And there were 4 data points which don not satisfy the requirement, should be deleted in our calculation. It was found that the previous value of ν is 0.515$\pm$0.039 at $\sqrt{s_{\mathrm{NN}}}$ = 7.7 GeV (without removing these points) and the new values is 0.535$\pm$0.041 after removing these points. The change is not bigger, but it is necessary to remove those points, and therefore make the $\Delta F_q(M)/\Delta F_2(M)$ plot look cleaner.

Figure 5.15 shows $\Delta F_q(M)$ (q=2-6) as a function of $\Delta F_2(M)$ in most central (0-5%) collision at all $\sqrt{s_{\mathrm{NN}}}$ and Fig. 5.16 show the results in 10-40% collisions. It's note that the $\Delta F_q(M)/\Delta F_2(M)$ scaling are not observed in 40-80% peripheral collisions since the higher

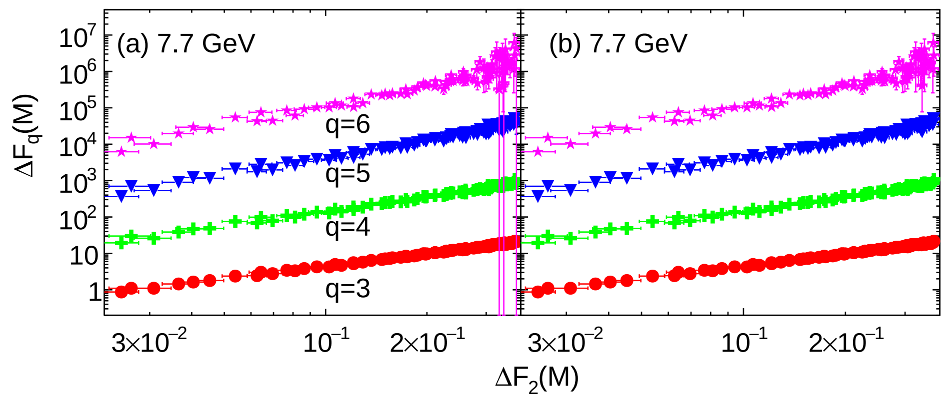

Figure 5.14: $\Delta F_q(M)$ (q=3-6) as a function of $\Delta F_2(M)$ in the most central (0-5%) Au + Au collisions at $\sqrt{s_{\mathrm{NN}}}$ = 7.7 GeV in double-logarithmic scale. The difference between Fig. (a) and (b) is that some data points of $\Delta F_6(M)$ which have very large error bars, are removed in Fig. (b).

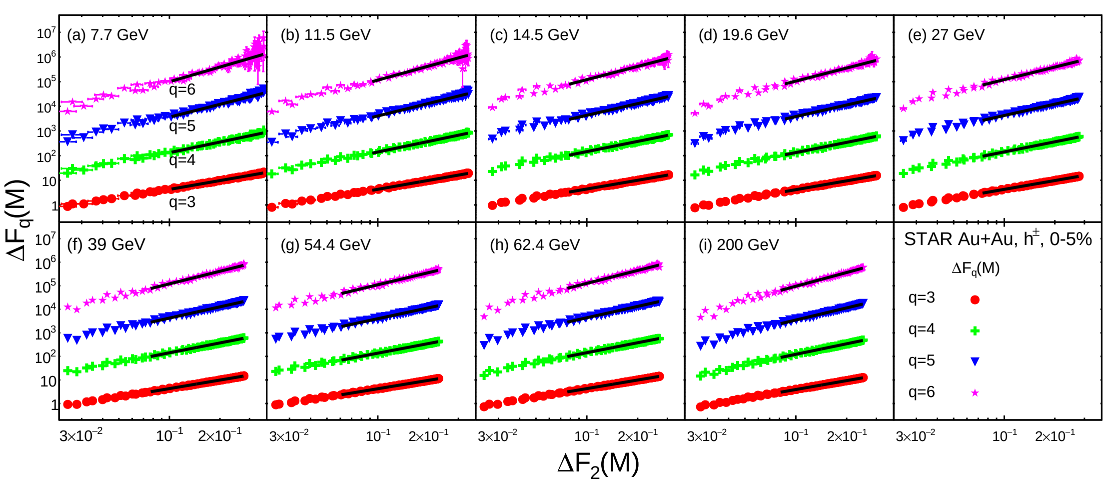

Figure 5.15: $\Delta F_q(M)$ (q=3-6) as a function of $\Delta F_2(M)$ in the most central (0-5%) Au + Au collisions at $\sqrt{s_{\mathrm{NN}}}$ = 7.7-200 GeV in double-logarithmic scale. The solid lines represent the power-law fit according to Eq.(1.9).

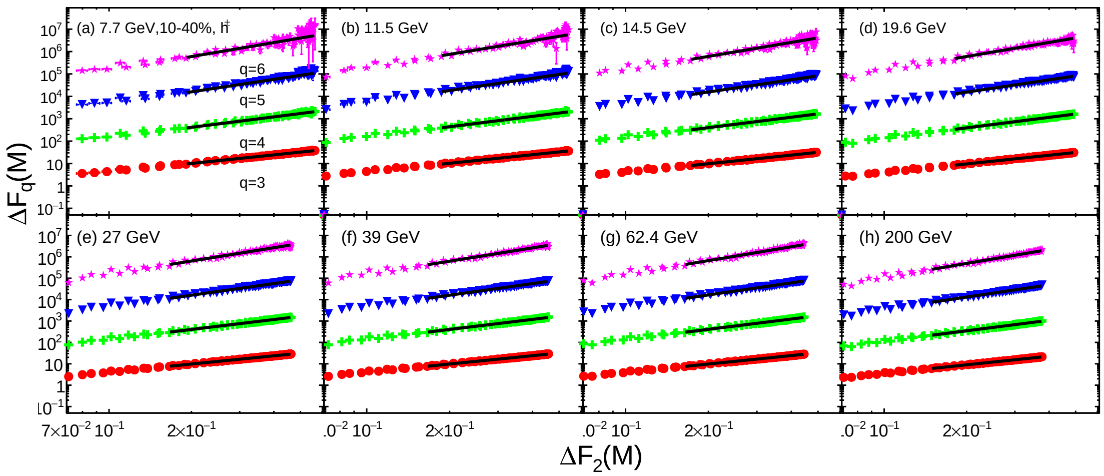

Figure 5.16: $\Delta F_q(M)$ (q=3-6) as a function of $\Delta F_2(M)$ in 10-40% central Au + Au collisions at $\sqrt{s_{\mathrm{NN}}}$ = 7.7-200 GeV in double-logarithmic scale.

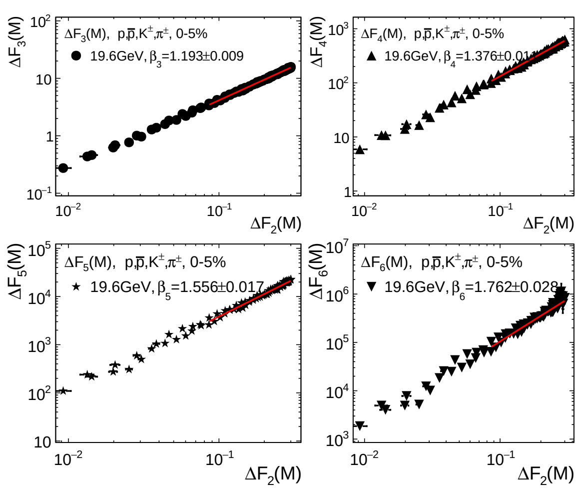

Figure 5.17: $\Delta F_q(M)$ (q=3-6) as a function of $\Delta F_2(M)$ in 0-5% central Au + Au collisions at $\sqrt{s_{\mathrm{NN}}}$ = 19.6 GeV in double-logarithmic scale.

order $\Delta F_q(M)(q = 5-6)$ have very large statistical error and thus can not be calculated. In Fig. 5.15 and Fig. 5.16, we clearly observe that $\Delta F_q(M)$ (q=3-6) obey strict power-law scaling with $\Delta F_2(M)$ in central Au + Au collisions as expected.

Figure 5.17 shows more detail of the $\Delta F_q(M)/\Delta F_2(M)$ scaling at $\sqrt{s_{\rm NN}}$ = 19.6 GeV. The solid lines are the results of the power-law fit according to Eq.(1.9). Its note that one should perform the intermittency analysis only using $F_q(M)$ at larger M^2 region because scaling behavior is associated with small momentum scales [60]. In our analysis, the chosen fitting range of $\Delta F_2(M)$ is at $M \in (30, 100)$ and is the same for all energy and centrality. Moreover, value of β_q is obtained through the fit of $\Delta F_q(M)/\Delta F_2(M)$ scaling and its error is determined by the fit, that is, the slope of back straight line. Here, $\Delta F_q(M)/\Delta F_2(M)$ scaling behaviors are found with $\beta_6 \geq \beta_5 \geq \beta_4 \geq \beta_3$. The extracted β_q is found to be changed little when the fitting range is varied, and we set the fitting range as one of systematic error.

5.6 Scaling Behavior of the Scaling Index on the Order

Figure 5.18 shows β_q as a functions of $q-1$ in 0-5% (red marks) and 10-40% (blue marks) central Au + Au collisions at $\sqrt{s_{\rm NN}}$ = 7.7-200 GeV. Agree with theoretical expectation, all order of β_q also obey a good scaling behavior with q, therefore scaling exponent, ν, can be obtained through a power-law fit of Eq.(1.10). The value of ν which is shown in legend, is the slope of linear lines and its error is determined by the fit. Figure shows the β_q/q scaling in 0-5%, 5-10%, 10-20%, 20-30% and 30-40% central Au + Au collisions at $\sqrt{s_{\rm NN}}$ = 19.6-200 GeV. At $\sqrt{s_{\rm NN}} \leq$ 19.6 GeV, the β_q/q scaling in these centralities are not shown since large statistical error for $\Delta F_q(M)(q = 5-6)$ and β_q can not be extracted.

5.7 Results of Scaling Exponent

As show in last sections, scaling exponent ν can be obtained through a power-law fit of β_q/q scaling observed in central Au + Au collisions.

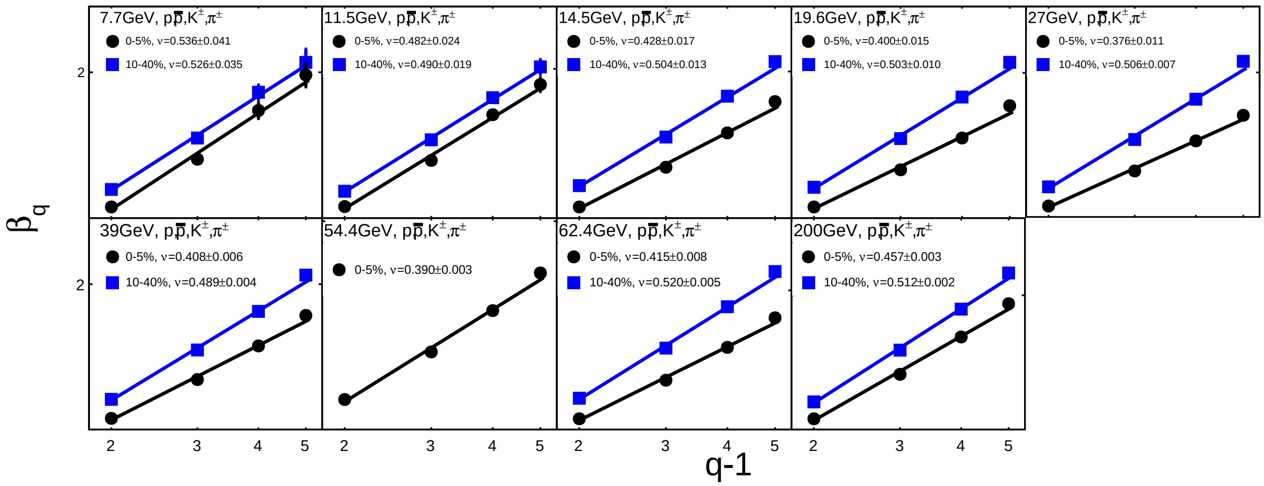

Figure 5.18: The β_q as a function of $q-1$ in 0-5% and 10-40% central Au + Au collisions at $\sqrt{s_{\mathrm{NN}}}$ = 7.7-200 GeV in double-logarithmic scale.

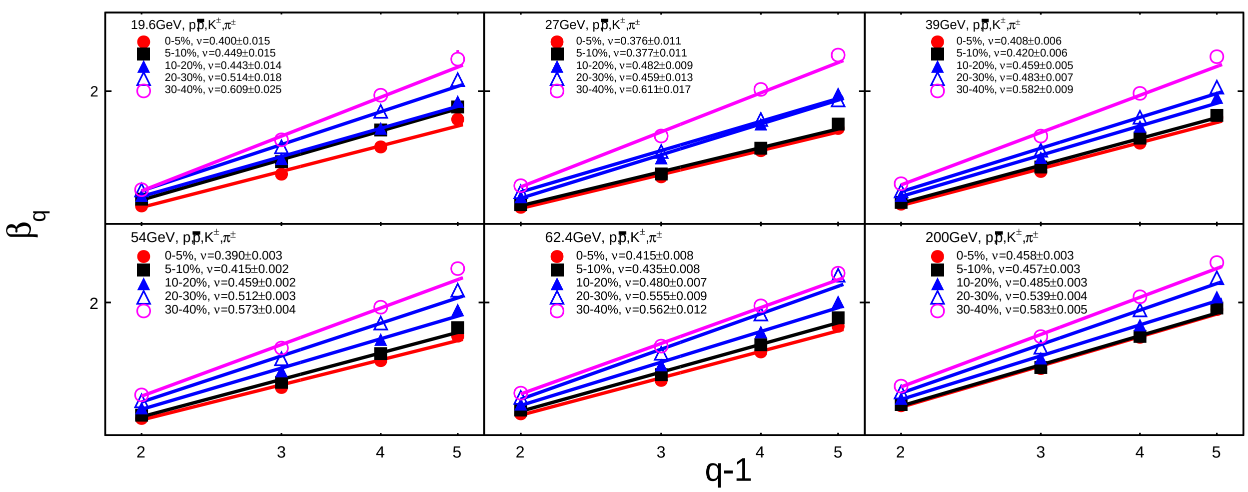

Figure 5.19: The β_q as a function of $q-1$ in 0-5%, 5-10%, 10-20%, 20-30% and 30-40% central Au + Au collisions at $\sqrt{s_{\mathrm{NN}}}$ = 19.6-200 GeV in double-logarithmic scale.

5.7.1 Corrected and Uncorrected Scaling Exponent

Figure 5.20 shows the efficiency corrected (red marks) ν Vs. uncorrected ν (black marks) for three fitting ranges. After efficiency correction, the values of ν become larger.

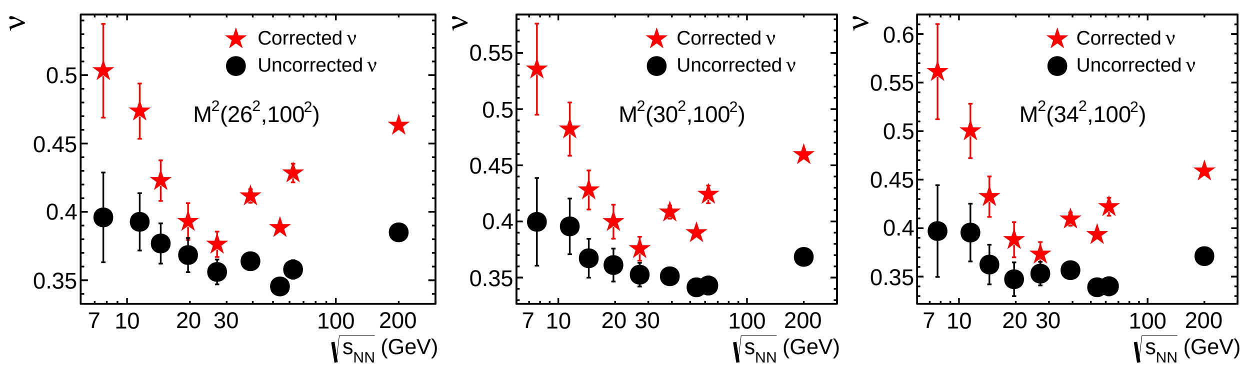

Figure 5.20: Efficiency corrected ν Vs uncorrected ν in 0-5% central collision at $\sqrt{s_{\mathrm{NN}}}$ = 7.7-200 GeV.

5.7.2 Scaling Exponent for Different Fitting Range

Figure 5.21 shows the energy dependence of ν for different fitting $\Delta F_2(M) \sim M^2$ range. We can see that the trend of energy dependence is not changing with different fitting range. Consider the statistical error, we set the range of $\Delta F_2(M)$ from $M^2 = 30$ to $M^2 = 100^2$ as default fitting range. Moreover, the range of $\Delta F_2(M)$ from $M^2 = 26$ to $M^2 = 100^2$, and from $M^2 = 34$ to $M^2 = 100^2$ will set as the variation of fitting range for systematic error.

5.7.3 Scaling Exponent for Different Track Cuts

Figure 5.22 show the ν for different variation of track cuts in 0-5%. We can see the NFitPoint cuts have more effect on ν than other track cuts, but it is not remarkable.

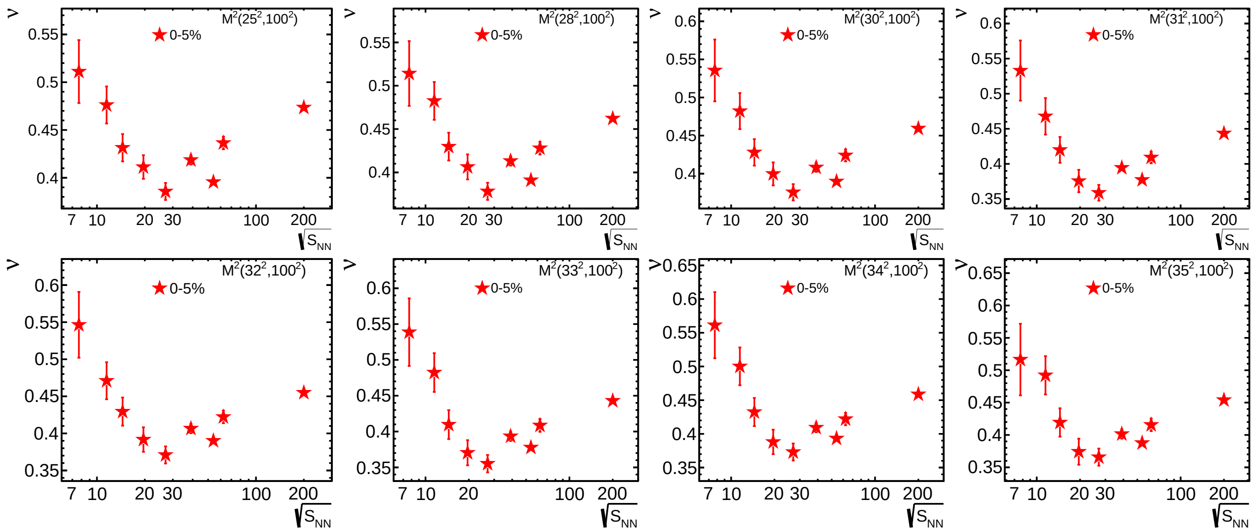

Figure 5.21: Efficiency corrected ν for different fitting range at $\sqrt{s_{\mathrm{NN}}}$ = 7.7-200 GeV.

5.8 Centrality Dependence of Scaling Exponent

In last sections, we have extracted ν for different centralities. Because the statistics at lower $\sqrt{s_{\mathrm{NN}}}$ (≤ 14.5 GeV) are not enough, the centrality dependence of ν can not be extracted. Besides, ν can not be extracted in peripheral collisions because higher orders of $\Delta F_q(M)$ (q=5-6) have very large statistical uncertainty.

In Fig. 5.23(a), we show the β_q as a function of $q-1$ in 0-5% central collisions. In Fig. 5.23(b), we show the ν, as a function of Average Number of Participant Nucleons $< N_{part} >$ in Au + Au collisions at $\sqrt{s_{NN}}$ = 7.7-200 GeV. Both of β_q and ν at all $\sqrt{s_{\mathrm{NN}}}$ are scaled by different factors. The statistical and systematical errors are shown in bars and brackets, respectively. Meanwhile, Fig. 5.24 shows the the same result in the plot of centrality bin Vs. ν. From Fig. 5.23(b) and 5.24, its found that ν decreases from mid-central (30-40%) to the most central (0-5%) Au + Au collisions.

The event statistics at $\sqrt{s_{\mathrm{NN}}}$ = 7.7-14.5 GeV don’t allow us to calculate the centrality de-

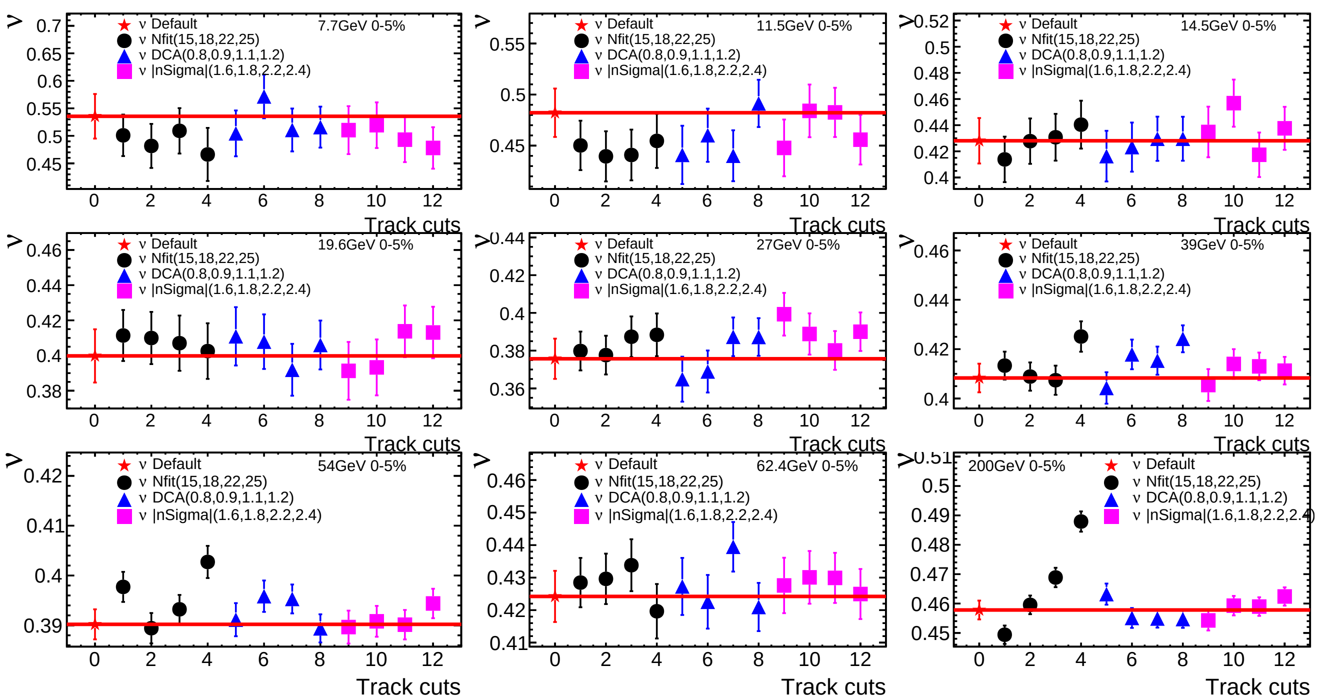

Figure 5.22: ν for different variation of track cuts in 0-5% central Au + Au collisions at $\sqrt{s_{\rm NN}}$ = 7.7-200 GeV. The red line represent the value of ν in the condition of the default track cuts.

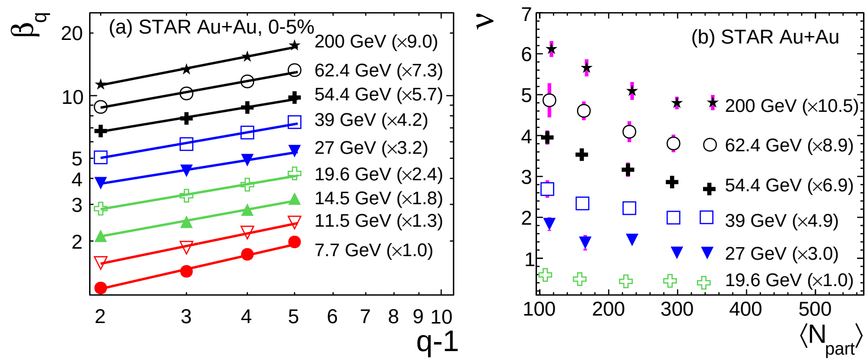

Figure 5.23: (a) The scaling index β_q (q=3-6) as a function of q-1 in most central Au + Au collisions at $\sqrt{s_{NN}}$ = 7.7-200 GeV. The solid lines are the result of the power-law fit according to Eq. (1.10). (b) The scaling exponent ν as a function of Average Number of Participant Nucleons ($< N_{part} >$) in Au + Au collisions at $\sqrt{s_{NN}}$ = 7.7-200 GeV.

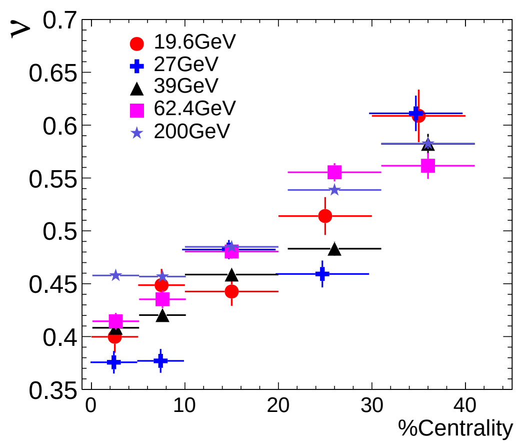

Figure 5.24: The scaling exponent ν as a function of centrality bin in Au + Au collisions at $\sqrt{s_{NN}}$ = 19.6-200 GeV.

pendence of scaling exponent from 0-5% to 30-40% centrality. To calculate the ν, the $\Delta F_q(M)$ is needed to calculate up to the sixth order. In Sec 5.3, we can see that higher order $\Delta F_6(M)$ in 30-40% centrality, can be calculated until $\sqrt{s_{NN}}$ = 19.6 GeV. Therefore, the results for $\sqrt{s_{\mathrm{NN}}}$ = 7.7-14.5 GeV are not included in Fig. 5.23 (b). In future works, the BSE-II data will allow us to calculate the centrality dependence of scaling exponent for $\sqrt{s_{\mathrm{NN}}}$ = 7.7-14.5 GeV.

5.9 Energy Dependence of Scaling Exponent

Figure 5.25 shows the energy dependence of ν of charged hadrons in Au + Au collisions for two collision centralities (0-5% and 10-40%). In the most central collisions, ν exhibits a non-monotonic behavior on collision energy and seems to reach a minimum around $\sqrt{s_{\mathrm{NN}}}$ = 20-30 GeV. On the other hand, ν shows a flat trend with increasing $\sqrt{s_{\mathrm{NN}}}$ in 10-40% central collisions. At lower $\sqrt{s_{\mathrm{NN}}} \leq$ 14.5 GeV, statistical and systematic uncertainty for ν are large, higher statistics data from BES-II will help confirm the trend of energy dependence of ν. Compare to theoretical prediction of critical $\nu = 1.30$ from GL theory [69] and 1.0 from 2D-Ising model [70, 75] which both are given in entire phase space and whole acceptance level, the observed ν is much smaller. Of course, it also much smaller than calculations from AMPT [77] and UrQMD [105] models. It is note that the observed ν is measured in available region of transverse momentum space with η and p_T acceptance, critical ν under such conditions need to be pointed out in theory.

5.10 Quantitative Estimation of the Non-monotonic Energy Dependence of Scaling Exponent

We estimate the non-monotonic energy dependence of ν as performed in net-proton C_4/C_2 paper [32]. In Fig. 5.26, the red and black solids lines represent third and fourth-order polynomial fit functions, respectively. We generated one million sets of points, and a fourth-order polynomial function is applied to fit each new ν vs. a $\sqrt{s_{\mathrm{NN}}}$ data set points. It was found that a

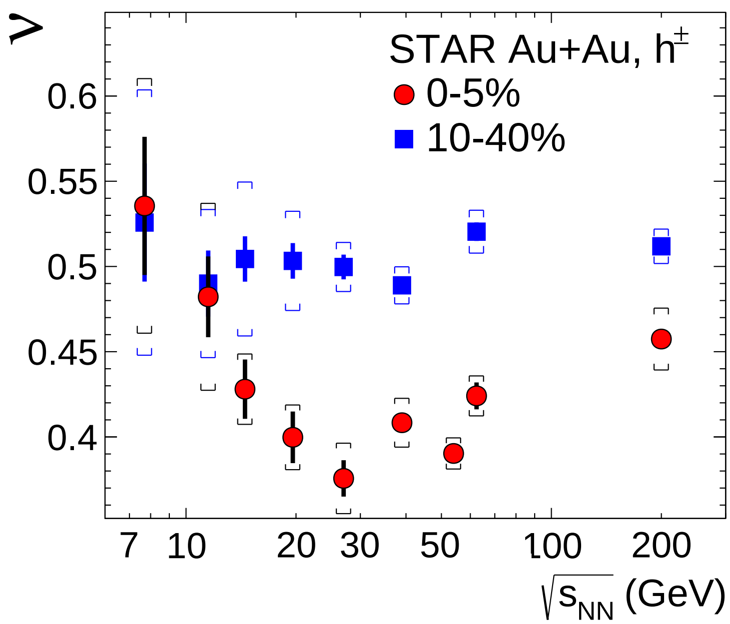

Figure 5.25: Energy dependence of scaling exponent, ν, of charged hadrons in Au + Au collisions at $\sqrt{s_{NN}}$ = 7.7-200 GeV. Red stars and blue circles represent ν in most central collisions(0-5%) and central collisions(10-40%), respectively. The statistical and systematical error are shown in bars and brackets, respectively.

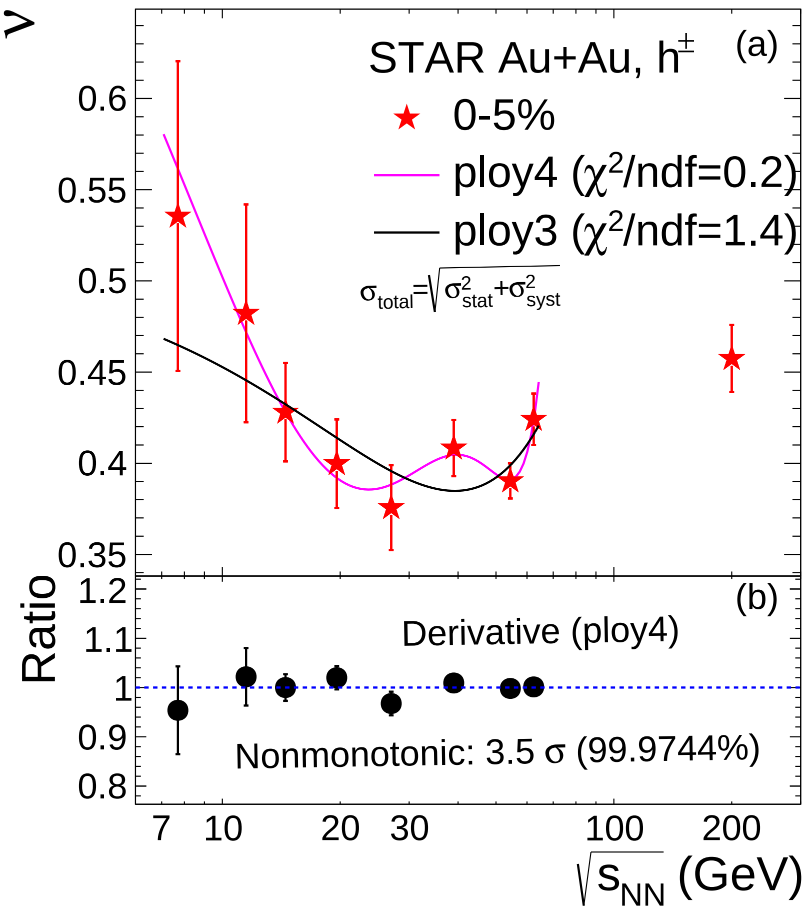

Figure 5.26: (a) The scaling exponent for charged hadrons in the most 0-5% central Au+Au collisions at $\sqrt{s_{\mathrm{NN}}}$ = 7.7-200 GeV. The bars on the data points are statistical and systematic uncertainties added on quadrature. The black solid line is 3th-order polynomial fit function, and red solid line is 4th-order polynomial fit function that best describe the data. (b) Derivative of the fitted polynomial as a function of $\sqrt{s_{\mathrm{NN}}}$.

total set of 255 sets were found to have the same derivative sign, and the probability that at least one derivative at a given collision energy has a different sign is $(10^6 - 255)/10^6$=99.9744%, which corresponds 3.5 σ.

$\sqrt{s_{\rm NN}}$ (GeV)	7.7 GeV	11.5 GeV	14.5 GeV	19.6 GeV	27 GeV	39 GeV	54 GeV	200 GeV
Case 1	5	0	0	1	49	2895	228	4220
Case 2	124	6	0	21	111245	15044	102330	210056
Case 3	1283	175	49	13248	463843	348772	258035	541681
Case 4	1419	1330	729	16977	222057	208601	221082	223433
All	2831	1511	778	30247	797194	575312	581675	979390

Table 5.1: The counts of different sign at all energies for 1 million data sets

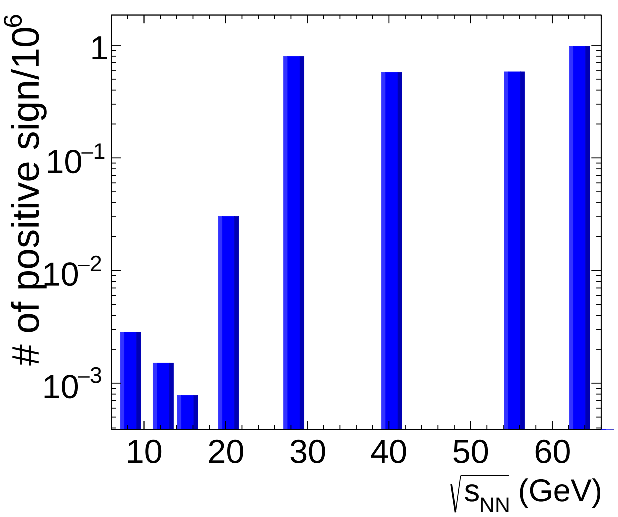

Figure 5.27: Counts of positive sign/10^6 versus collision energy.

We recorded the counts of different sign (positive values of derivative) at various collision energy. For example, given a set, if there is only a positive value of derivative in eight values and this positive value is at $\sqrt{s_{\mathrm{NN}}}$ = 27 GeV, the counts at $\sqrt{s_{\mathrm{NN}}}$ = 27 GeV will add 1. Also, if there are two positive values in eight values at $\sqrt{s_{\mathrm{NN}}}$= 27 GeV and 62.4 GeV, both the count of different sign at $\sqrt{s_{\mathrm{NN}}}$ = 27 GeV and 62.4 GeV will add 1.

We listed the counts of different sign at all energies for 1 million data sets as table 5.1. In table 5.1, "Case 1" means that there is only a positive value of derivative (other are negative values) and corresponding count for all energies. And soon, "Case 4" means that there are four positive values of derivative (other are negative values) and corresponding count for all energies.

The counts of positive sign which are the values in the last row of upper table, are divined by the numbers of data sets at all energies. Fig. 5.27 shows counts of positive sign/10^6 vs. collision energy. We can see there is suddenly change at $\sqrt{s_{\mathrm{NN}}}$ = 19.6-27 GeV. In addition, the value at $\sqrt{s_{\mathrm{NN}}}$ = 62.4 GeV is largest since the value of derivative at this energy is almost large than 0 according to the fitting result of $4th$-order polynomial function.

Chapter 6

Results from Models

6.1 Results from the Ultra relativistic Quantum Molecular Dynamics (UrQMD) Model

In high energy collisions, the UrQMD model has been widely and successfully applied to simulate $p+p$, $p+A$, and $A+A$ interactions [106, 107, 108]. It is a microscopic transport approach which treats the covariant propagation of all hadrons as classical trajectories combined with stochastic binary scatterings, the excitation and fragmentation of color strings, and decay of hadronic resonances [106].

The UrQMD model represents a Monte Carlo solution of a large set of coupled partial integro-differential equations for the time evolution of the various phase space densities $f_i(x,p)$ of particle species, which non-relativistically assumes the Boltzmann form [106]:

$$\frac{df_i(x,p)}{dt} = Stf_i(x,p), \tag{6.1}$$

where x and p are the position and momentum of the particle.

Particles are represented by Gaussian wave packets in the phase space which read as [106, 109]:

$$\psi_i(r) = (\frac{1}{2\pi L^2})^{3/4} e^{-\frac{r-r_i}{4L^2}} e^{\frac{iP_i \cdot r}{h}} \tag{6.2}$$

where L is the width parameter of the wave packet. The Wigner distribution function f_i of particle i can be derived by [106, 109]:

$$f_i(r,p) = \frac{1}{(\pi\hbar)^3} e^{-(r-r_i)^2/2L^2} e^{-(p-p_i)^2 \cdot 2L^2/h^2} \tag{6.3}$$

where r and p are the coordinate and momentum of particle, given by the Hamilton’s equation of motion [106, 109]:

$$\dot{r}_i = \frac{\partial H}{\partial p_i}, \quad \dot{p}_i = -\frac{\partial H}{\partial r_i}. \tag{6.4}$$

The Hamiltonian H consists of the kinetic energy T and the potential energy V ($H = T + V$). The potential energies include the two-body and three-body Skyrme-, Yukawa-, Coulomb- and Pauli-terms as a base [106, 109]:

$$V = V_{sky}^{(2)} + V_{sky}^{(3)} + V_{Yuk} + V_{Cou} + V_{Pau} \tag{6.5}$$

The UrQMD model incorporates baryon-baryon, meson-baryon and meson-meson interactions with collision terms including more than 50 baryon and 45 meson species, and all particles can be produced in hadron-hadron collisions. Conservation law of electric charge and baryon number are taken into account in the model [110, 111]. It can reproduce the cross-section of hadronic reactions, and successfully describe yields and momentum spectra of various particles in $A + A$ collisions [106, 112]. The UrQMD is a well-designed transport model for simulations with the entire available range of energies from Schwerionen Synchrotron at GSI Darmstadt (SIS) energy ($\sqrt{s_{\rm NN}} \approx 2$ GeV) to the top RHIC energy ($\sqrt{s_{\rm NN}}$ = 200 GeV). More details about the model can be found in Refs [106, 107, 113].

The UrQMD model is a suitable simulator to estimate non-critical contributions from the hadronic phase as well as the associated physics processes since there is no phase transition to

QGP state in the simulation. In this work, we use the cascade UrQMD model (version 3.4) to generate event samples in Au+Au collisions at RHIC energies.

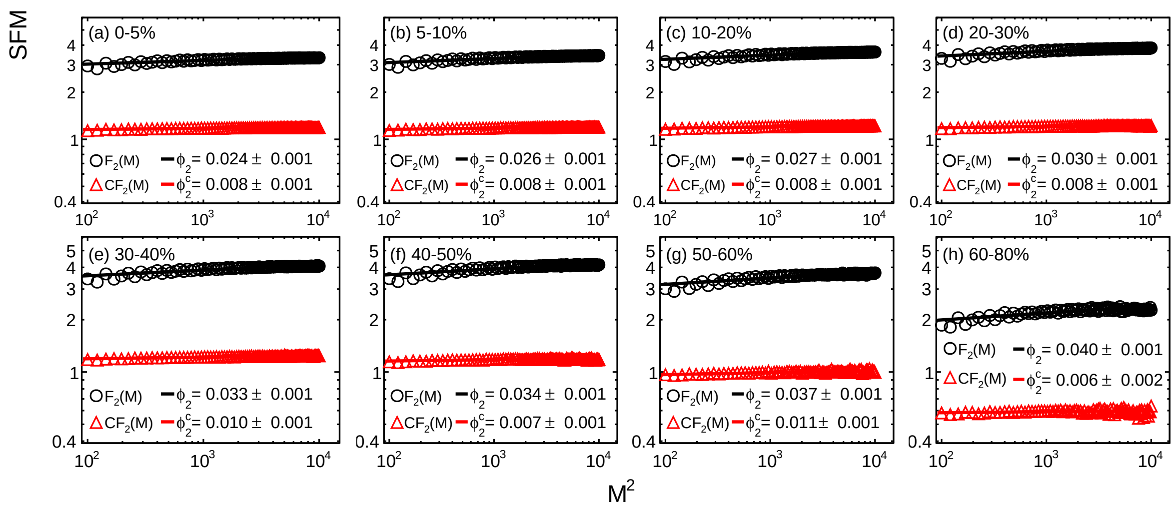

Figure 6.1: The second-order scaled factorial moment (black circles) as a function of number of partitioned cells from the most central ($0\% - 5\%$) to the most peripheral ($60\% - 80\%$) collisions at $\sqrt{s_{\mathrm{NN}}}$ = 19.6 GeV. The corresponding red ones represent the SFMs calculated by the cumulative variable method.

6.1.1 Centrality Dependence of SFMs for Protons

By using the UrQMD model, we generate event samples at various centralities in Au + Au collisions at $\sqrt{s_{\mathrm{NN}}}$ = 7.7, 11.5, 19.6, 27, 39, 62.4, and 200 GeV. The corresponding event statistics are 72.5, 105, 106, 81, 133, 38, 56 millions at $\sqrt{s_{\mathrm{NN}}}$ = 7.7, 11.5, 19.6, 27, 39, 62.4, 200 GeV, respectively. In the model calculations, we apply the same kinematic cuts and technical analysis methods as those used in the RHIC (STAR) experiment data [46]. The protons are measured at midrapidity($|y| < 0.5$) within the transverse momentum $0.4 < p_T < 2.0$ GeV/c. The centrality is defined by the charged pion and kaon multiplicities within pseudorapidity $|\eta| < 1.0$. Since we only concern protons in the calculations and use pions and kaons without protons to determine centrality, it can effectively avoid auto-correlation effects in the measurement of SFMs. In our analysis, we focus on proton multiplicities in a two-dimensional transverse momentum space of p_x and p_y. The available two-dimensional (2D) region of transverse momentum is partitioned into M^2 equal-size bins to calculate SFMs in various sizes of cells. The statistical error is estimated by the bootstrap method [114].

The $F_2(M)$ measured at various collision centralities in Au + Au collisions at $\sqrt{s_{\rm NN}}$ = 19.6 GeV are shown as the black circles in Fig. 6.1. And the black lines are the fitting according to power-law function of $F_q(M) \propto (M^2)^{\phi_q}$. We find that the directly calculated SFMs can be fitted with a small intermittency index. The values of ϕ_2 increase slightly from the most central ($0\% - 5\%$) to the most peripheral ($60\% - 80\%$) collisions.

6.1.2 Energy Dependence of SFMs for Protons

In Fig. 6.2, the black circles represent the second-order SFMs as a function of number of partitioned bins, directly calculated in transverse momenta for proton numbers in $0\% - 5\%$ the most central Au + Au collisions at $\sqrt{s_{\rm NN}}$ = 7.7-200 GeV. It is observed that $F_2(M)$ increases slowly with increasing number of dividing bins. The black lines show the power-law fit of $F_2(M)$ according to Eq. (1.8). The slopes of the fitting, i.e., the intermittency indices ϕ_2, are found to be small at all energies. And they are much less than the theoretical prediction $\phi_2 = 5/6$ for a critical system of the 3D-Ising universality class [58].

We calculate SFMs in the same event sample by the proposed cumulative variable method and then get the intermittency index from $CF_2(M)$. The results are shown as red triangles and red lines in Fig. 6.1 and Fig. 6.2. $CF_2(M)$ is found to be nearly flat with an increasing number of cells in all measured energies and centralities. Furthermore, the intermittency index, with the value near to zero, is much smaller than the value directly calculated from $F_2(M)$. It verifies that the background of noncritical effect can be efficiently removed by the cumulative variable method in the calculation of SFMs in the UrQMD model. This method could also be used for the intermittency analysis in the ongoing experimental at RHIC (STAR) or further heavy-ion experiments in search of the QCD critical point.

We would also note that the fit values of ϕ_2^c from $CF_2(M)$ are still not exactly zero although they are much smaller than ϕ_2 obtained directly from measured $F_2(M)$. It possibly accounts for other effects such as proton correlations due to Coulomb repulsion and Fermi–Dirac statistics [65] or the influence of momentum resolution [115]. Further studies on these effects should also be concerned in the calculation of intermittency index in heavy-ion collisions.

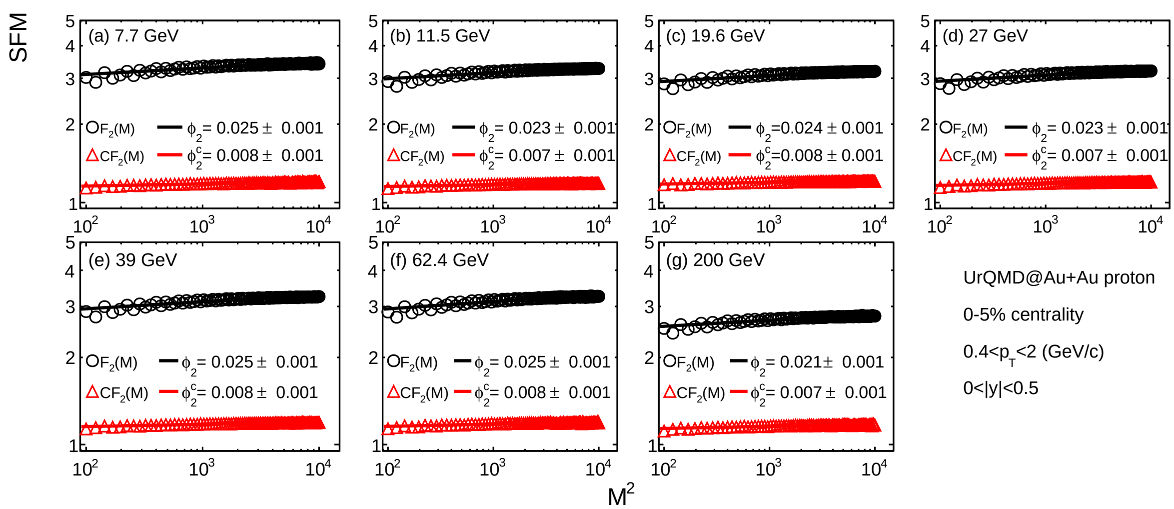

Figure 6.2: The second-order scaled factorial moment (black circles) $F_2(M)$ as a function of number of partitioned cells in a double-logarithmic scale at $\sqrt{s_{\mathrm{NN}}}$ = 7.7-200 GeV from the UrQMD model. The black lines are the power-law fitting. The corresponding red ones represent the SFMs calculated by the cumulative variable method.

In current experimental explorations of the intermittency in heavy-ion collisions, the NA49 and NA61 collaborations have directly measured ϕ_2 at various sizes of colliding nuclei [60, 65, 116], which are represented as blue symbols in Fig. 6.3. The intermittency parameter at $\sqrt{s_{\mathrm{NN}}}$ = 17.3 GeV for the Si + Si system at NA49 experiment approaches the theoretic expectation value, shown as red arrow in the figure, in the second-order phase transition in a critical QCD

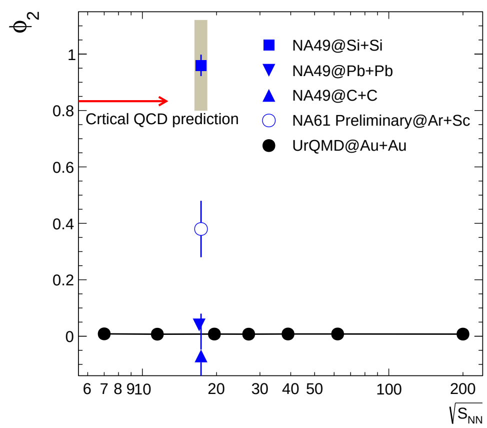

Figure 6.3: The second-order intermittency index measured at NA49 [60, 65] (solid blue symbols) and NA61 [116] (open blue circles). The results from the UrQMD model in central Au + Au collisions are plotted as black circles. The red arrow represents the theoretic expectation from a critical QCD model [58].

model [58]. The black circles of the UrQMD results give a flat trend with the value around zero at all energies because no critical mechanisms are implemented in the transport model.

6.1.3 Energy Dependence of SFMs for Charged Hadrons

In our analysis, we apply the same analysis techniques and kinematic cuts as those used in the STAR experiment. Charged Hadrons including proton (p), anti-proton ($\bar{p}$), kaons ($K^{\pm}$) and pions ($\pi^{\pm}$) are selected within pseudo-rapidity window ($|\ \eta\ | < 0.5$), p_T window ($0.2 < p_T < 1.6$ GeV/c) for $K^{\pm}$ and $\pi^{\pm}$, and ($0.4 < p_T < 2.0$ GeV/c) for p and $\bar{p}$. To avoid auto-correlation effects, the centrality is determined from uncorrected charged particles within $0.5 <|\ \eta\ |< 1$, which is chosen to be beyond the analysis window $|\ \eta\ |< 0.5$. Two dimensional transverse momentum space of p_x and p_y are partitioned into M^2 equal-size cells to calculate $F_q(M)$ with M^2 varying from 1 to 100^2. The corresponding event statistics are 1.54, 1.17, 1.15, 1.25,

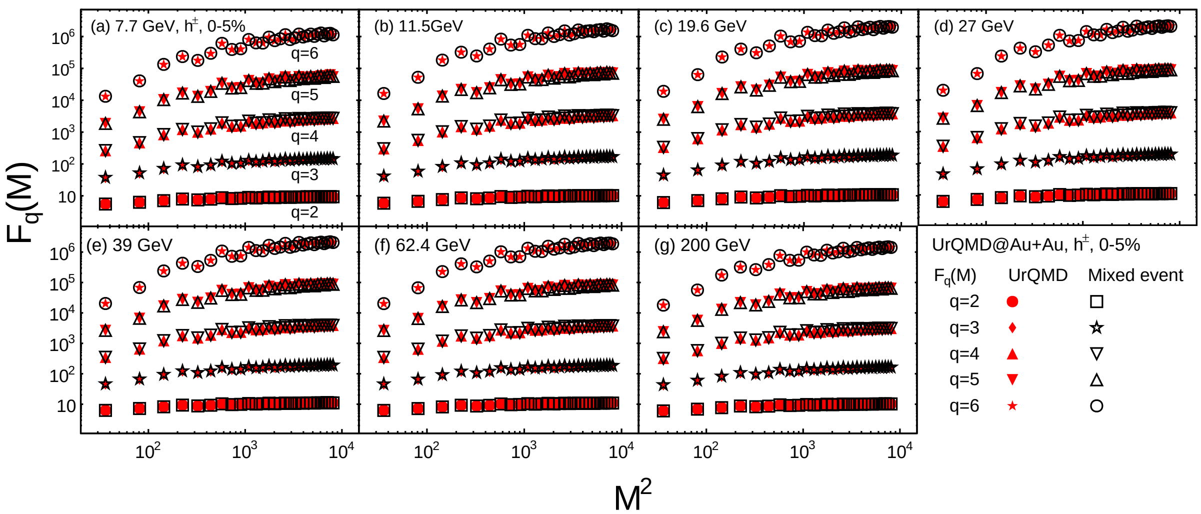

Figure 6.4: The scaled factorial moments, $F_q(M)$ (up to sixth order), as a function of number of cells (M^2) of charged hadrons in the most central (0-5%) Au+Au collisions at $\sqrt{s_{\rm NN}}$ = 7.7-200 GeV from the UrQMD model in a double-logarithmic scale. Red (black) marks represent $F_q(M)$ of UrQMD data (mixed events), respectively. Statistical uncertainties are obtained from the Bootstrap method and are smaller than the maker size.

1.20, 1.30, 0.5×10^6 at $\sqrt{s_{\rm NN}}$ = 7.7, 11.5, 19.6, 27, 39, 62.4, 200 GeV, respectively.

In Fig. 6.4, we show $F_q(M)$ of UrQMD data (red marks) and the corresponding mixed events (black marks) of charged hadrons, as a function of M^2 in the most central (0-5%) Au+Au collisions at $\sqrt{s_{\rm NN}}$ = 7.7-200 GeV. $F_q(M)$ of UrQMD and associated mixed events are calculated up to the sixth order. Its found that $F_q(M)^{UrQMD}$ are almost overlapped with $F_q(M)^{mix}$, which leads to the correlator $\Delta F_q(M) \approx 0$. It implies that the magnitude of $F_q(M)^{UrQMD}$ are dominated by non-critical background contributions from the cascade UrQMD model. There should be no intermittency in this model since it does not incorporate any self-similar local density fluctuations. In contrast to the UrQMD model, $F_q(M)^{data}$ ($q = 2-6$) are larger than $F_q(M)^{mix}$ and thus $\Delta F_q(M)$ increase with increasing M^2 at RHIC energies from the preliminary results of the STAR experiment.

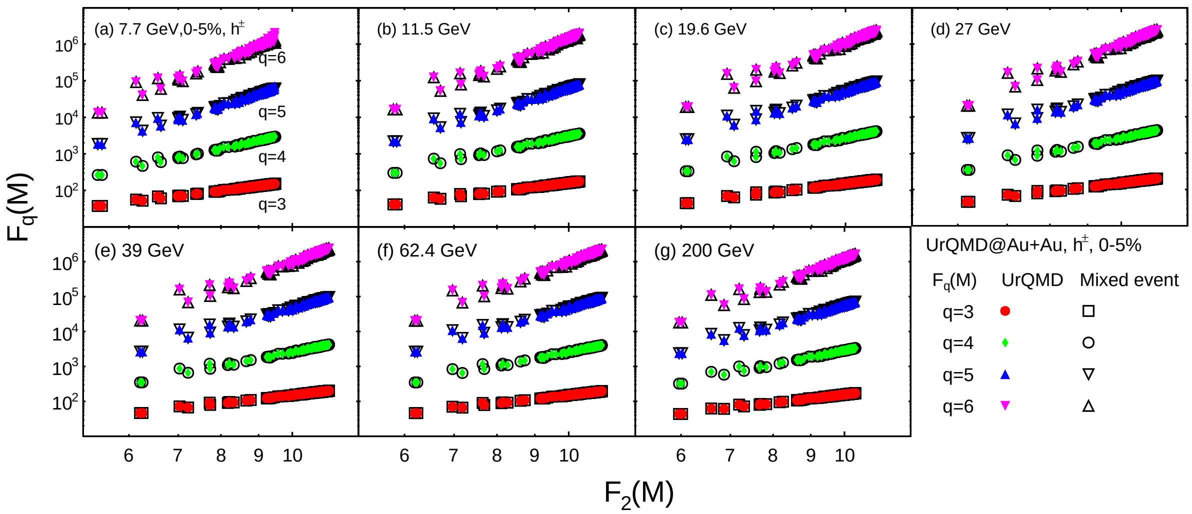

Figure 6.5: The higher-order $F_q(M)$ (q=3-6) of charged hadrons as a function of $F_2(M)$ in the most central (0-5%) Au+Au collisions at $\sqrt{s_{\mathrm{NN}}}$ = 7.7-200 GeV from the UrQMD model in a double-logarithmic scale. Solid (open) marks represent $F_q(M)$ of UrQMD data (mixed events), respectively.

6.1.4 Scaling Behavior of SFMs for Charged Hadrons

We then investigate the $F_q(M)/F_2(M)$ scaling as introduced in Eq. (1.9). The solid symbols in Fig. 6.5 illustrate the higher-order $F_q(M)^{UrQMD}$ (q=3-6) of charged hadrons as a function of $F_2(M)^{UrQMD}$ in the most central (0-5%) Au+Au collisions at $\sqrt{s_{\mathrm{NN}}}$ = 7.7-200 GeV. It seems that $F_q(M)^{UrQMD}$ (q=3-6) exhibit clear power-law scaling with $F_2(M)^{UrQMD}$. Whereas, the corresponding open symbols for the mixed events agree well with the UrQMD results. It means that background effects dominate the observed $F_q(M)/F_2(M)$ scaling in the cascade UrQMD samples. This scaling will be vanished if the background effects are subtracted from the UrQMD results by the mixed event method.

6.2 Results from the Critical Monte Carlo (CMC) Model

6.2.1 The Critical Monte Carlo Model

In order to study the intermittency behavior in detail by using the SFM method, we generate simulation events by implementing a critical Monte-Carlo (CMC) model [58]. The simulation of CMC sample involving critical fluctuations in the baryon density requires the generation of baryon momenta correlated according to the power law of Eq. (1.5). A Levy random walk method [117] is proposed to produce the momentum profile of the final state particles, with the probability density between two adjacent walks:

$$\rho(p) = \frac{\nu p_{\text{min}}^{\nu}}{1-(p_{\text{min}}/p_{\text{max}})^{\nu}} p^{-1-\nu}. \tag{6.1}$$

Here p is the momentum distance of two particles which satisfying $p \in [p_{\text{min}}, p_{\text{max}}]$. The model parameters can be set to $\nu = 1/6$ and $p_{\text{min}}/p_{\text{max}} = 10^{-7}$ for the 3D Ising universality class with the fractal dimension $\tilde{d}_F \simeq \frac{1}{3}$. The detailed description of the algorithm and implementation of the CMC model can be found in [58, 67].

In Fig. 6.6, the open black circles show the second-order SFM as a function of the number of partitioned bins in a two-dimensional momentum space. The results are obtained for an ensemble of 600 critical events. In each event, the multiplicity distribution obeys a Poisson with the mean value $\langle n_B \rangle = 20$. The solid black line is a fitting according to Eq. (1.8). Its clearly seen that the SFMs follow a good power law behavior with the increasing number of bins. It confirms that the CMC model can well reproduce the self-similar correlations as shown in Eq. (1.5). The fitting slope, i.e. the second-order intermittency index ϕ_2, is found to be 0.834 ± 0.001, which is consistent with the theoretic expectation $\phi_2 = 5/6$ for a critical system with the fractal dimension $\tilde{d}_F \simeq \frac{1}{3}$ [58]. The open red triangles in the same figure are results from the UrQMD model, with the same mean multiplicity around 20. The SFMs of the UrQMD model are found to be nearly flat in various binning, with the intermittency index is around 0. This is due to no critical related self-similar fluctuations implemented in the transport model.

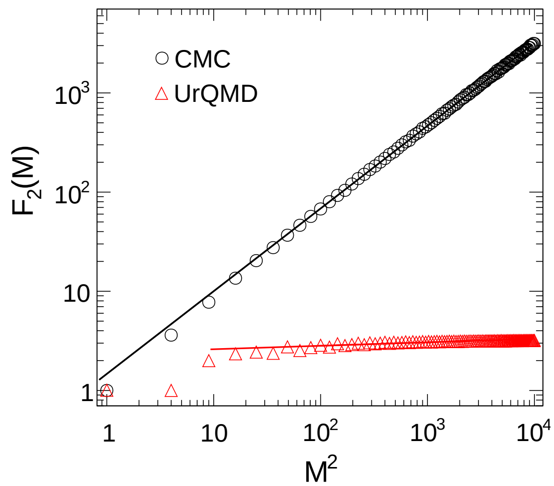

Figure 6.6: The second-order SFM as a function of number of partitioned bins in a double-logarithmic scale.

6.2.2 Baryon Density Fluctuations and Self-similar Correlations

In order to explore the baryon density fluctuations in the CMC model, we illustrate the density distribution in a 2D momentum space in the upper pad of Fig. 6.7. The lower pad shows the same plot with a contour view. From the figure, strong clustering effects in momentum space, which indicating giant phase-space density fluctuations are found. The observed large density fluctuations are probes of critical singularity of the system belong to the Ising universality class. These large local density fluctuations are suggested to be a manifestation of intermittency [58].

It is argued [62] that if intermittency occurs in particle production, large density fluctuations are not only expected, but should also exhibit a self-similarity behavior. In the current CMC model, the probability density distribution of two particles with distance p in momentum space is given by Eq. (6.1). It implies that two particle correlations are determined by the Levy distribution. The exponent of the Levy distribution is supposed to be related to the critical

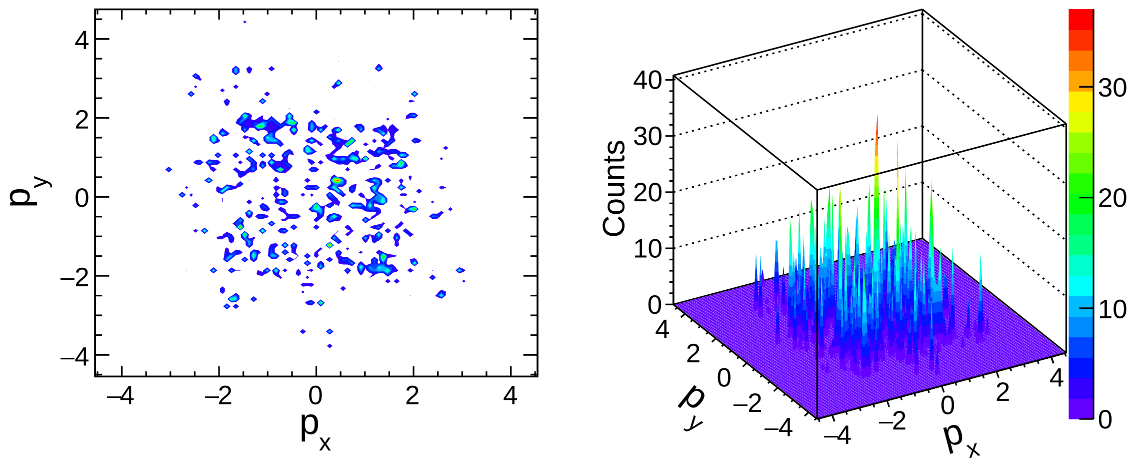

Figure 6.7: Baryon density fluctuations in a 2D momentum space.

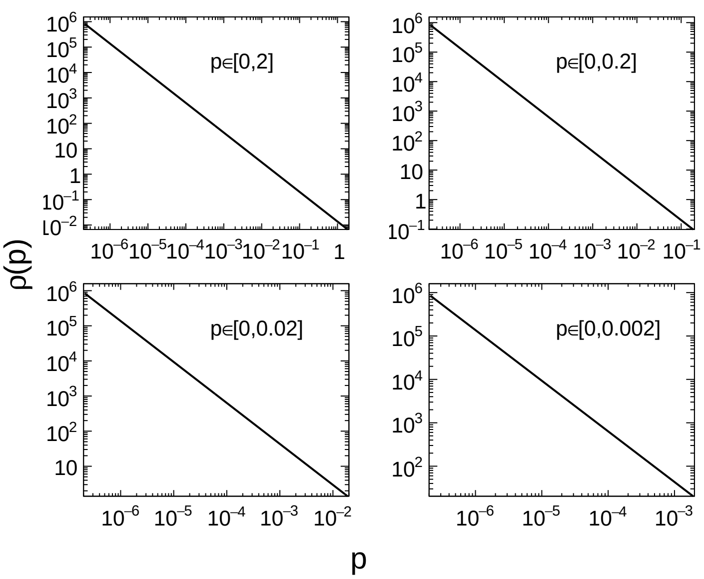

Figure 6.8: The baryon density probability distribution in four different magnification scales.

exponent of a system at a second-order phase transition. And it characterizes the power law structure of the particle correlation at the critical point [118].

Figure 6.8 presents the distributions of baryon density in four different magnification scales. We observe that the curves look the same at every level of magnification. They follow the same distribution in various momentum scales, i.e. scale invariant. Scale invariance is an exact form of self-similarity where at any magnification there is a smaller piece of the object that is similar to the whole. It is a typical character of a self-similar fractal system. The self-similar or intermittency nature of particle correlations in the CMC model is closely related to the large baryon density fluctuations which have been observed in Fig. 6.7, for a 3D Ising universality class system.

6.2.3 Relation between the Relative Density Fluctuation and Intermittency

In order to quantitatively describe density fluctuation, the relative density fluctuation of baryons Δn is defined as [54, 55]:

$$\Delta n = \frac{\langle(\delta n)^2\rangle}{\langle n\rangle^2} = \frac{\langle n^2\rangle - \langle n\rangle^2}{\langle n\rangle^2} \tag{6.2}$$

where the angle bracket means the average in the phase space of the whole produced event sample.

By using the above introduced CMC algorithm method, we perform an event-by-event analysis on the scaled factorial moments and fit the intermittency index according to Eq. (1.8). In the mean time, the baryon relative density fluctuations are also calculated from the produced baryons in the model. In Fig. 6.9, the solid black line shows the second-order intermittency index ϕ_2 as a function of Δn. The ϕ_2 is found to be monotonically increased with increasing relative density fluctuation Δn. Therefore, large intermittency is expected if giant baryon density fluctuations are developed near the QCD critical region. Furthermore, Once the relation between Δn and ϕ_2 is obtained one can get the density fluctuations by measuring intermittency

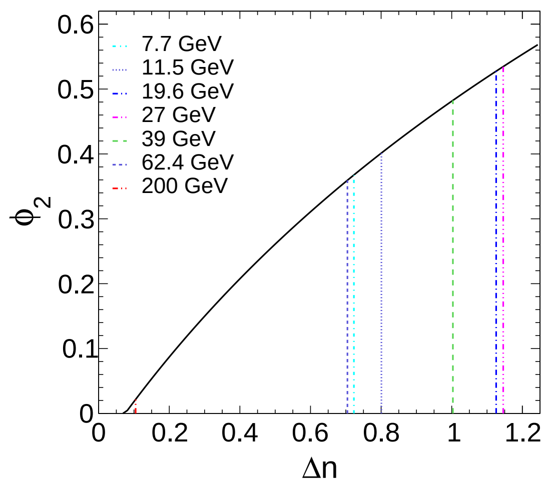

Figure 6.9: The second-order intermittency index as a function of baryon relative density fluctuation. The dash lines show the experimental measured density fluctuations at RHIC-STAR [50, 119].

index from the same event sample, or vice versa. Thus, it provides an experimentally measurable quantity to estimate the density fluctuations in addition to measuring the light nuclei productions based on a coalescence model calculation [54, 55]. The RHIC-STAR experiment has calculated relative density fluctuations through the measurement of the production yields of proton, deuteron, and triton in the central Au + Au collisions [50, 119]. The dash lines in Fig. 6.9 display the values of measured density fluctuations at $\sqrt{s_{NN}}$ = 7.7, 11.5, 19.6, 27, 39, 62.4 and 200 GeV, respectively.

6.2.4 Critical Intermittency for Charged Hadrons

In Fig. 6.10 (a), the red symbols show the $F_q(M)/M$ scaling from the CMC sample which incorporates the same statistics, mean multiplicity and p_T distributions as those in the UrQMD sample at $\sqrt{s_{\mathrm{NN}}}$= 19.6 GeV. $F_q(M)^{CMC}$ of all orders are found to rise with increasing M^2.

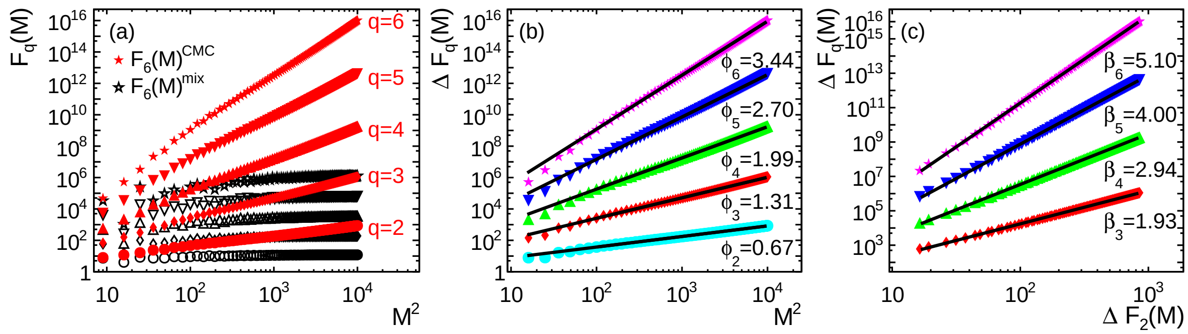

Figure 6.10: (a) The scaled factorial moments as a function of number of divided cells in the CMC (solid red symbols) and mixed event (open black ones) samples in a double-logarithmic scale. (b) The correlator $\Delta F_q(M)$ (q=2-6) as a function of M^2 from the CMC model. The solid black lines are the fitting according to the power-law relation of Eq. (1.8). (c) The higher-order $\Delta F_q(M)$ (q=3-6) as a function of $\Delta F_2(M)$. The solid black lines are the fitting according to Eq. (1.9).

The corresponding open black symbols are the results from the mixed events. we observe that $F_q(M)^{CMC}$ (q=2-6) are clearly larger than $F_q(M)^{mix}$, especially in large M^2 regions. After subtracting background by using the mixed event method, Fig. 6.10 (b) shows the correlator $\Delta F_q(M)$ as a function of M^2. A good scaling behavior is satisfied for each order of $\Delta F_q(M)$, i.e. $\Delta F_q(M)/M$ scaling is observed in the CMC model. Fig. 6.10 (c) presents $\Delta F_q(M)$ (q=3-6) as a function of $\Delta F_2(M)$. Its found that the correlators $\Delta F_q(M)$ follow strict $\Delta F_q(M)/\Delta F_2(M)$ scaling as illustrated in Eq. (1.9). Then we can fit the values of β_q and obtain the exponent ν by using Eq. (1.10). The value of ν is found to be around 1.03 ± 0.01, which is slightly larger than theoretical expectation, i.e. 1.0 in the Ising system [70, 75]. It is caused by the finite event statistics and momentum resolution. It will give an upper limit to the number of maximum division cells and maximum order in real calculations.

6.3 Results from the Hybrid UrQMD+CMC Model

In the mean time, various model studies have been conducted to try to understand the measured intermittency in experiments [76, 77, 120, 121, 122, 123]. An overview of the results can be found in Ref. [84]. However, none of the models in the market can describe the latest intermittency measurement in the STAR experiment and therefore warrants further investigations. Among these models, the UrQMD is the one that can well simulate the dynamics of evolution in $A + A$ collisions and successfully describes several experimental results [106, 108, 112, 124]. This cascade model has been proven to be appropriate for a background study in the intermittency analysis since no critical self-similar mechanism is implemented in it. On the other hand, a CMC model can easily simulate critical intermittency driven by self-similar density fluctuations [58, 65]. But it can only produce scale-invariant multiplicity distributions in momentum space and does not include evolution of the system or background effects in heavy-ion collisions. Therefore, it is meaningful to combine these two models together to get a hybrid UrQMD+CMC one. In the hybrid model, the self-similar density fluctuations generated by the CMC simulation are incorporated into the final-state multiplicity distributions in the UrQMD event sample [125]. We will use this hybrid model to study intermittency at RHIC beam energy scan (BES) energies and try to understand the STAR experimentally measured results.

6.3.1 The Hybrid UrQMD+CMC Model

In the previous sections, we have observed that the CMC model exhibits good intermittency behavior as expected. Nevertheless, it is a toy model which only produces momentum profiles of critically correlated particles and does not include the dynamical evolution in heavy-ion collisions. One straightforward approach is to combine the CMC model with the UrQMD model, which aims to realize the presence of intermittency in heavy-ion collisions.

To get the hybrid UrQMD+CMC model, part of the particles from the UrQMD model, which have already passed through the microscopic transport and final-state interactions, are substituted with those from the CMC simulation that have the same multiplicity and p_T distri-

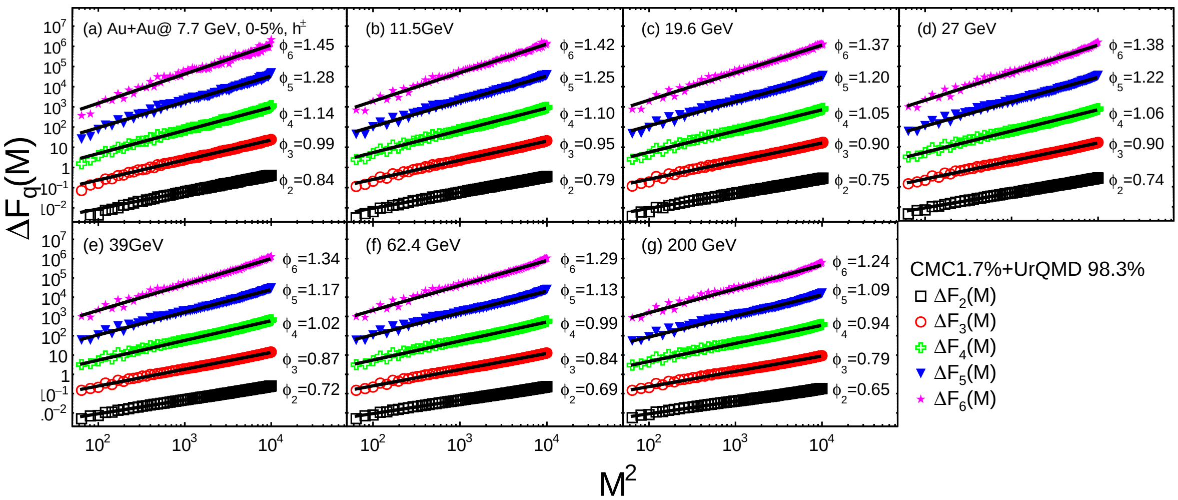

Figure 6.11: The $\Delta F_q(M)$ (q=2-6) of charged hadrons as a function of M^2 in the most central (0-5%) Au+Au collisions at $\sqrt{s_{\mathrm{NN}}}$ = 7.7-200 GeV from the UrQMD+CMC model with replacing fraction λ = 1.7%. The solid black lines represent the power-law fitting according to Eq. (1.8).

butions. The replacing fraction is defined as [126]:

$$\lambda = \frac{N_{\mathrm{CMC}}}{N_{\mathrm{UrQMD}}}, \tag{6.1}$$

where N_{CMC} is the number of CMC particles and N_{UrQMD} is the multiplicity in an original UrQMD event. To keep the p_T distribution of the new UrQMD+CMC sample to be the same as that of the original UrQMD sample, we require the replacement to take place when $|p_T(\mathrm{CMC}) - p_T(\mathrm{UrQMD})| < 0.2$ (GeV/c) is satisfied. For a system with weak signal but strong background noises, as in the NA49 Si+Si collision, λ is a small number.

6.3.2 Apparent Intermittency in the UrQMD+CMC Model

Figure 6.11 depicts $\Delta F_q(M)$ as a function of M^2 in the most central (0-5%) Au+Au collisions at $\sqrt{s_{\mathrm{NN}}}$ = 7.7-200 GeV from the UrQMD+CMC model with the replacing fraction

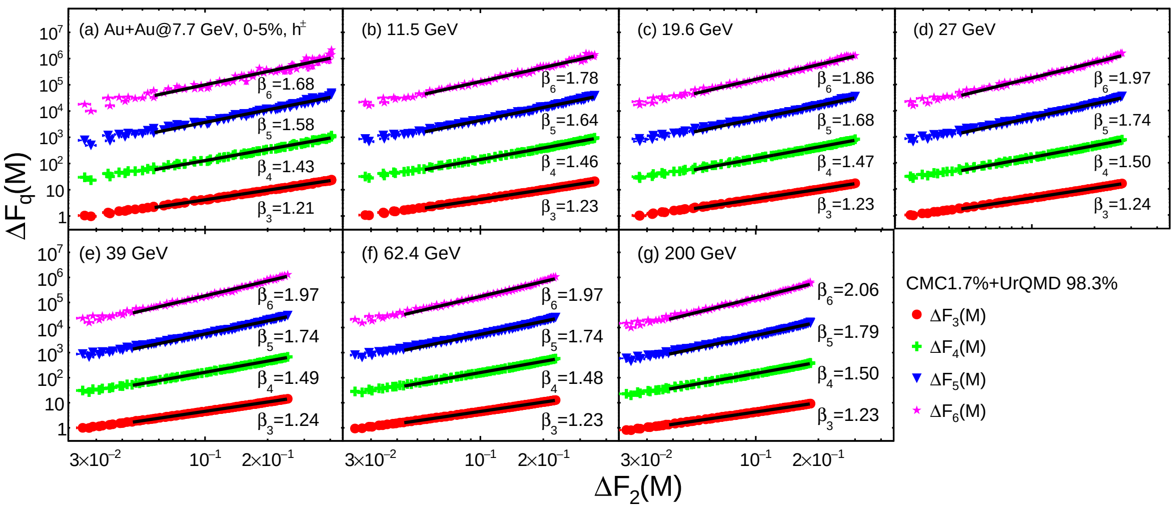

Figure 6.12: The higher-order $\Delta F_q(M)$ (q=3-6) as a function of $\Delta F_2(M)$ in the most central (0-5%) Au+Au collisions at $\sqrt{s_{\mathrm{NN}}}$ = 7.7-200 GeV from the UrQMD+CMC model with λ = 1.7%. The solid black lines represent the power-law fitting according to Eq. (1.9)

$\lambda = 1.7\%$. We observe that $\Delta F_q(M)$ (q=2-6) exhibit good power-law behaviors with increasing M^2 at various energies. It indicates that self-similar density fluctuations have been successfully incorporated into the UrQMD+CMC model. The solid black lines are the power-law fitting based on Eq. (1.8). Its found that the intermittency indices of higher order $\Delta F_q(M)$ are larger than those of lower ones at various energies.

The results from the STAR experiment, show that the $\Delta F_q(M)/\Delta F_2(M)$ scaling is found in the most central Au+Au collisions. And this observation can not be described by the cascade UrQMD model. In the following, we will check whether the hybrid UrQMD+CMC model could reproduce the experimental measured scaling-law.

In Fig. 6.12, we plot $\Delta F_q(M)$ (q=3-6) as a function of $\Delta F_2(M)$ calculated from UrQMD+CMC samples at seven RHIC BES-I energies with $\lambda = 1.7\%$. In this case, $\Delta F_q(M)$ are found to obey good power-law scaling behaviors with increasing $\Delta F_2(M)$ at various energies, which agrees with what observed in the STAR experimental data. The solid black lines are the fitting according to the $F_q(M)/F_2(M)$ scaling in Eq. (1.9). The fitting range is chosen to be $M \in [30, 100]$, which is the same as that used in the STAR experimental analysis. From these fitting, we can obtain β_q and the scaling exponent ν by Eq. (1.9) and (1.10), respectively.

6.3.3 Energy Dependence of Scaling Exponent from the Hybrid UrQMD+CMC Model

In experiments, a possible intermittency signal may be shaded behind large background effects or other noises. First, finite size effects [127], limited lifetime or critical slowing down of the system will restrict the growth of critical fluctuations in dynamic evolution of heavy-ion collision system [128]. Second, some trivial effects and experimental limitations, such as conservation law [129], resonance decay and hadronic rescattering [130], finite fluctuations inside the experimental acceptance [46, 131] as well as momentum resolution [115], will weak or smear critical fluctuations. Its found that the observed power-law behavior in the NA49 experiment in Si+Si collisions can be reproduced by mixing 1% of CMC particles with 99% of random (uncorrelated) ones, indicating that the noise or background is indeed dominant in the experimental measurement [65]. It is meaningful to see how many percentages of intermittency signal could be related to the scaling behavior observed in the STAR experiment.

Fig. 6.13 illustrates the energy dependence of the scaling exponent ν in the most central (0-5%) Au+Au collisions at $\sqrt{s_{\mathrm{NN}}}$ = 7.7-200 GeV from the UrQMD+CMC model with four different replacing fractions. We observe that all the ν calculated in the UrQMD+CMC model are smaller than 1.03, i.e. the value obtained in the pure CMC model. The reason is that large fraction of background particles from the UrQMD model fade the self-similar behavior. Furthermore, the values of ν get larger with higher replacing fractions. And they are found to monotonically increase with increasing $\sqrt{s_{\mathrm{NN}}}$ in all cases. This is due to more particles from the CMC model being included in the data samples with larger λ or higher energies. The increase of the UrQMD particles in the mean time with energy has little effects on ν because the uncorrelated background fluctuations have been subtracted by the mixed event method and the contribution to the value of ν is much smaller than that from the CMC particles. For

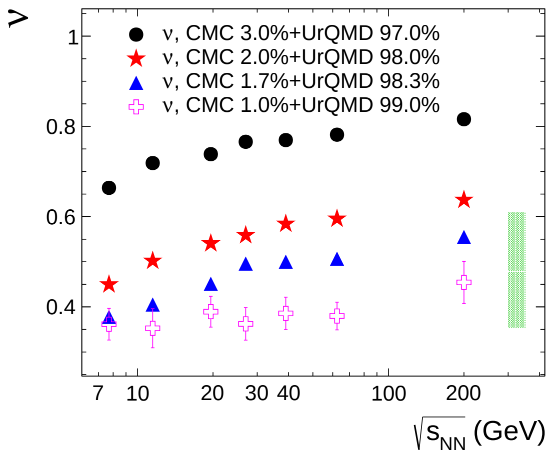

Figure 6.13: The energy dependence of the scaling exponent (ν) in the most central (0-5%) Au+Au collisions at $\sqrt{s_{\mathrm{NN}}}$ = 7.7-200 GeV from the UrQMD+CMC model with four selected replacing fractions. The green band illustrates the range of ν measured in the STAR experiment.

comparison, the green band in the same figure denotes the range of ν (0.35-0.6) measured in the most central (0-5%) Au+Au at $\sqrt{s_{\mathrm{NN}}}$ = 7.7-200 GeV from the STAR experiment. We find that the calculated ν in the UrQMD+CMC model, with λ chosen to be between 1% and 2%, fall in the experimentally measured range. Therefore, the UrQMD+CMC model can successfully reproduce the important scaling exponent measured by the STAR Collaboration. If infers that only 1-2 % signal of intermittency could be related to the data sets from the STAR experiment, which is similar to value of λ = 1% in Si+Si collisions from the NA49 experiment [65].

The experimentally measured scaling exponent ν exhibits a non-monotonic behavior on beam energy and reaches a minimum around $\sqrt{s_{\mathrm{NN}}}$ = 20-30 GeV from the STAR experiment. Our current hybrid UrQMD+CMC model cannot reproduce this non-monotonic energy dependence. It is due to a fixed replacing fraction λ being used for various energies in this work. In a real experiment, the fraction of critical particles over background ones could depend on collision energy. This issue should be carefully taken into account in further study to investigate and understand the observed non-monotonic behavior at STAR.

Chapter 7

Summary and Outlook

One of the major goals in heavy-ion collisions is to locate the critical point in the phase diagram of strongly interacting matter predicted by quantum chromodynamics (QCD). Near the QCD critical point, the collision system will develop large density fluctuations. Such fluctuations manifest itself as critical intermittency in heavy-ion collisions, and can be probed via the framework of intermittency analysis by utilizing the scaled factorial moments (SFMs). The intermittency index and scaling exponent, extracted from the power-law scaling of SFMs, characterize the strength the intermittency. The energy dependence of intermittency index and scaling exponent could be used to search for the QCD critical point. In this thesis, we have reported the intermittency analysis in heavy-ion collisions from the STAR experiment, as well as models.

We have presented the first measurement of intermittency in heavy-ion collisions at RHIC. The data presented here were obtained from Au+Au collisions at $\sqrt{s_{\mathrm{NN}}}$ = 7.7, 11.5, 14.5, 19.6, 27, 39, 54.4, 62.4, and 200 GeV, recorded by the Solenoidal Tracker at RHIC (STAR) experiment from 2010 to 2017. These energies correspond to μ_B values ranging from 20 to 420 MeV at chemical freeze-out in the QCD phase diagram. All data were obtained using the Time Projection Chamber (TPC) and the Time-of-Flight (TOF) detectors at STAR. Charged hadrons, including protons (p), antiprotons ($\bar{p}$), kaons ($K^{\pm}$), and pions ($\pi^{\pm}$), are identified using the TPC and TOF detectors. In experimental analysis, the mixed event method is applied to eliminate background contributions, and the cell-by-cell method is proposed and used for the application of efficiency corrections on SFMs.

In this data analysis, the transverse momentum space ($p_x - p_y$) SFMs of identified charged hadrons including p, $\bar{p}$, $K^{\pm}$ and $\pi^{\pm}$ within $|\eta| < 0.5$, have been analyzed and calculated up to the sixth order in Au$+$Au collisions at $\sqrt{s_{\mathrm{NN}}}$ = 7.7-200 GeV. With background subtraction, a distinct scaling behavior between the higher-order and second-order SFMs, $\Delta F_q(M)/\Delta F_2(M)$ scaling, is observed in Au$+$Au collisions at all energies. Based on the scaling behavior, the extracted scaling exponent ν monotonically from the peripheral to the central Au$+$Au collisions. Moreover, a non-monotonic energy dependence on collision energy is observed, and ν reaches a possible minimum around $\sqrt{s_{\mathrm{NN}}}$ = 27 GeV in the 0-5% most central collisions. However, a constant energy dependence is observed in the mid-central (10-40%) collisions. Whether the observed non-monotonic behavior is related to QCD critical point or not, detailed calculations from dynamical modelling of heavy-ion collisions with a realistic equation of state is needed. Note that a non-monotonic energy dependence of the fourth order net-proton cumulants ratios has been observed at a similar energy region, which is suggested as a signature of the QCD critical point [32, 46]. Understanding the non-monotonic behavior of the scaling exponent will help to locate the critical point in the QCD phase structure.

In the original cascade UrQMD model, both for protons and charged hadrons, the values of SFMs are observed to overlap with those from the mixed events, and $\Delta F_q(M)$ for all orders are around 0 at all collision centralities and energies. Neither $\Delta F_q(M)/M$ or $\Delta F_q(M)/\Delta F_2(M)$ scaling is observed when the background contributions from the mixed events are subtracted. Those results are consistent with the fact that the UrQMD model does not incorporate any density fluctuations.

In order to study the intermittency behavior in detail by using the SFM method, we generate critical events incorporating strong intermittency by a Critical Monte-Carlo (CMC) model. The SFMs obey a clear power-law scaling with M^2 and the extracted ϕ_q is consistent with the theoretic expectation, therefore the self-similar intermittent behavior can be well simulated in

Au+Au Collisions at RHIC

Collider Runs						Fixed-Target Runs					
	$\sqrt{s_{NN}}$ (GeV)	#Events	μ_B	y_{beam}	run		$\sqrt{s_{NN}}$ (GeV)	#Events	μ_B	y_{beam}	run
1	**200**	380 M	**25** MeV	5.3	Run-10, 19	1	13.7 (100)	50 M	280 MeV	-2.69	Run-21
2	62.4	46 M	75 MeV		Run-10	2	**11.5 (70)**	50 M	320 MeV	-2.51	Run-21
3	54.4	1200 M	85 MeV		Run-17	3	**9.2 (44.5)**	50 M	370 MeV	-2.28	Run-21
4	39	86 M	112 MeV		Run-10	4	**7.7 (31.2)**	260 M	420 MeV	-2.1	Run-18, 19, 20
5	27	585 M	156 MeV	3.36	Run-11, 18	5	7.2 (26.5)	470 M	440 MeV	-2.02	Run-18, 20
6	19.6	595 M	206 MeV	3.1	Run-11, 19	6	6.2 (19.5)	120 M	490 MeV	1.87	Run-20
7	17.3	256 M	230 MeV		Run-21	7	5.2 (13.5)	100 M	540 MeV	-1.68	Run-20
8	14.6	340 M	262 MeV		Run-14, 19	8	4.5 (9.8)	110 M	590 MeV	-1.52	Run-20
9	**11.5**	57 M	316 MeV		Run-10, 20	9	3.9 (7.3)	120 M	633 MeV	-1.37	Run-20
10	**9.2**	160 M	372 MeV		Run-10, 20	10	3.5 (5.75)	120 M	670 MeV	-1.2	Run-20
11	**7.7**	104 M	420 MeV		Run-21	11	3.2 (4.59)	200 M	699 MeV	-1.13	Run-19
						12	**3.0** (3.85)	2300 M	**760** MeV	-1.05	Run-18, 21

Figure 7.1: An overview of Beam Energy Scan Phase-II proposal at RHIC-STAR. The BES-II program combines collider and fixed-target configurations, and covers a range of beam collision energy $\sqrt{s_{\rm NN}}$ = 3-200 GeV [38].

.

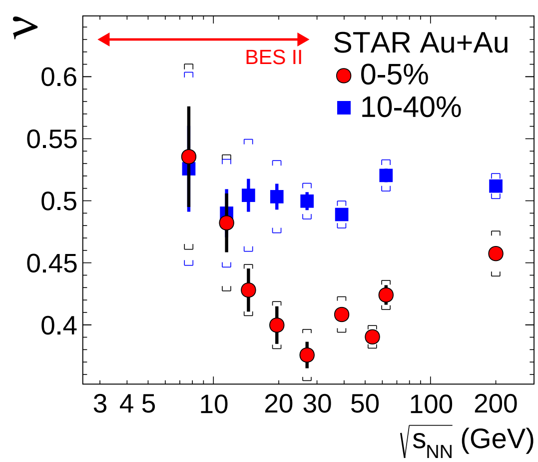

Figure 7.2: Energy dependence of scaling exponent, ν, of charged hadrons in Au + Au collisions at $\sqrt{s_{NN}}$ = 7.7-200 GeV. The red arrow represents the range of $\sqrt{s_{NN}}$ = 3-27 GeV in the BES-II program.

the CMC model. Based on the calculations from the CMC model, it is found that the self-similar or intermittency nature of particle correlations is closely related to the observed large baryon density fluctuations associated with the QCD critical point. Moreover, large intermittency is expected if giant baryon density fluctuations are developed near the QCD critical region since the intermittency index (ϕ_q) is found to be monotonically in-creased with increasing relative density fluctuation Δn. Furthermore, after including the same statistics, multiplicity, and transverse momentum distributions as those from the UrQMD samples, we found that the calculated SFM from the CMC model is larger than that from the mixed events. Both the $\Delta F_q(M)/M$ and the $\Delta F_q(M)/\Delta F_2(M)$ scaling are clearly observed in the CMC model.

To describe and understand the STAR experimentally measured results, we incorporate density fluctuations generated from the CMC model into the event samples from the UrQMD model. The hybrid UrQMD+CMC model does exhibit strict power-law dependence up to the sixth-order on the number of division cells in momentum space. The $\Delta F_q(M)/\Delta F_2(M)$ scaling is verified at all collision energies, which is consistent with the experimental results observed in the STAR data. As 1-2 % signal of critical fluctuations from the CMC model is embedded, the energy dependence of the extracted scaling exponents show that the values are well within the experimentally measured range. This result indicates that there only exists 1-2 % of intermittency signal in the central Au+Au collisions from the STAR experiment.

The RHIC-STAR experiment has finished operating the second phase of beam energy scan (BES-II) program in 2018–2021. Figure 7.1 shows the points of collision energy and corresponding event statistics in the BES-II program. Compared with the first program, the second BES-II program has more precise data with significant improved statistics. With data from the BES-II program, we will confirm the energy dependence of scaling exponent, and extend the collision energy to a lower energy ($\sqrt{s_{\mathrm{NN}}}$ = 3 GeV), as shown in Fig. 7.2. In upcoming work, more precise measurement of intermittency will further improve our understanding of the QCD phase diagram at finite baryon density.

References

[1] S. L. Glashow, Nucl. Phys. **22**, 579 (1961).

[2] A. Salam and J. C. Ward, Phys. Lett. **13**, 168 (1964).

[3] S. Weinberg, Phys. Rev. Lett. **19**, 1264 (1967).

[4] R. B. Mann, *An introduction to particle physics and the standard model* (CRC Press, Boca Raton, FL, 2010).

[5] G. Sterman, in *Encyclopedia of Mathematical Physics*, edited by J.-P. Françoise, G. L. Naber, and T. S. Tsun (Academic Press, Oxford, 2006) pp. 144–153.

[6] F. Gross *et al.*, (2022), arXiv:2212.11107 [hep-ph] .

[7] Z. P. Szadkowski, *Quantum Chromodynamic* (IntechOpen, Rijeka, 2021).

[8] M. Gell-Mann, Physics Letters **8**, 214 (1964).

[9] D. J. Gross and F. Wilczek, Phys. Rev. Lett. **30**, 1343 (1973).

[10] S. Bethke, Prog. Part. Nucl. Phys. **58**, 351 (2007), arXiv:hep-ex/0606035 .

[11] H. D. Politzer, Phys. Rev. Lett. **30**, 1346 (1973).

[12] P. A. Zyla *et al.* (Particle Data Group), PTEP **2020**, 083C01 (2020).

[13] H. Satz, Rept. Prog. Phys. **63**, 1511 (2000), arXiv:hep-ph/0007069 .

[14] P. Braun-Munzinger and J. Stachel, Nature **448**, 302 (2007).

[15] U. Heinz, Int. J. Mod. Phys. A **30**, 1530011 (2015).

[16] I. Arsene *et al.* (BRAHMS), Nucl. Phys. A **757**, 1 (2005), arXiv:nucl-ex/0410020 .

[17] B. B. Back *et al.* (PHOBOS), Nucl. Phys. A **757**, 28 (2005), arXiv:nucl-ex/0410022 .

[18] J. Adams *et al.* (STAR), Nucl. Phys. A **757**, 102 (2005), arXiv:nucl-ex/0501009 .

[19] S. Chatrchyan *et al.* (CMS), JHEP **05**, 063 (2012), arXiv:1201.5069 [nucl-ex] .

[20] B. Abelev *et al.* (ALICE), Phys. Rev. Lett. **109**, 072301 (2012), arXiv:1202.1383 [hep-ex] .

[21] K. H. Ackermann *et al.* (STAR), Phys. Rev. Lett. **86**, 402 (2001), arXiv:nucl-ex/0009011 .

[22] C. Adler *et al.* (STAR), Phys. Rev. Lett. **90**, 082302 (2003), arXiv:nucl-ex/0210033 .

[23] A. R. Timmins (STAR), J. Phys. G **36**, 064006 (2009), arXiv:0812.4080 [nucl-ex] .

[24] J. Adam *et al.* (ALICE), Nature Phys. **13**, 535 (2017), arXiv:1606.07424 [nucl-ex] .

[25] Available online. http://web.suda.edu.cn/xuxinping/index.html.

[26] C. Shen, Available online. https://u.osu.edu/vishnu/.

[27] R. Pasechnik and M. Sumbera, Universe **3**, 7 (2017), arXiv:1611.01533 [hep-ph] .

[28] P. Braun-Munzinger and J. Wambach, Rev. Mod. Phys. **81**, 1031 (2009), arXiv:0801.4256 [hep-ph] .

[29] X. Luo, S. Shi, N. Xu, and Y. Zhang, Particles **3**, 278 (2020), arXiv:2004.00789 [nucl-ex] .

[30] A. Bzdak, S. Esumi, V. Koch, J. Liao, M. Stephanov, and N. Xu, Phys. Rept. **853**, 1 (2020), 1906.00936 [nucl-th] .

[31] X. Luo, Q. Wang, N. Xu, and P. Zhuang, eds., *Properties of QCD Matter at High Baryon Density* (Springer, 2022).

[32] J. Adam *et al.* (STAR), Phys. Rev. Lett. **126**, 092301 (2021), arXiv:2001.02852 [nucl-ex] .

[33] X. Luo and N. Xu, Nucl. Sci. Tech. **28**, 112 (2017), arXiv:1701.02105 [nucl-ex] .

[34] Y. Aoki, G. Endrődi, Z. Fodor, S. D. Katz, and K. K. Szabo, Nature **443**, 675 (2006), arXiv:hep-lat/0611014 .

[35] S. Ejiri, Phys. Rev. D **78**, 074507 (2008), arXiv:0804.3227 [hep-lat] .

[36] Y. Hatta and M. A. Stephanov, Phys. Rev. Lett. **91**, 102003 (2003).

[37] E. S. Bowman and J. I. Kapusta, Phys. Rev. C **79**, 015202 (2009), arXiv:0810.0042 [nucl-th] .

[38] STAR Note 0598: BES-II whitepaper. https://drupal.star.bnl.gov/STAR/starnotes/public/sn0598.

[39] M. Maćkowiak-Pawłowska (NA61/SHINE), Nucl. Phys. A **1005**, 121753 (2021), arXiv:2002.04847 [nucl-ex] .

[40] T. Ablyazimov *et al.* (CBM), Eur. Phys. J. A **53**, 60 (2017), arXiv:1607.01487 [nucl-ex] .

[41] M. Gazdzicki and P. Seyboth, Acta Phys. Polon. B **47**, 1201 (2016), arXiv:1506.08141 [nucl-ex] .

[42] Available online. https://nica.jinr.ru/.

[43] Available online. http://hiaf.impcas.ac.cn/.

[44] M. A. Stephanov, Phys. Rev. Lett. **107**, 052301 (2011), arXiv:1104.1627 [hep-ph] .

[45] W. Fan, X. Luo, and H.-S. Zong, Int. J. Mod. Phys. A **32**, 1750061 (2017), arXiv:1608.07903 [hep-ph] .

[46] M. Abdallah *et al.* (STAR), Phys. Rev. C **104**, 024902 (2021), arXiv:2101.12413 [nucl-ex] .

[47] L. Adamczyk *et al.* (STAR), Phys. Rev. Lett. **112**, 162301 (2014), arXiv:1401.3043 [nucl-ex] .

[48] L. Adamczyk *et al.* (STAR), Phys. Rev. C **92**, 014904 (2015), arXiv:1403.4972 [nucl-ex] .

[49] R. A. Lacey, Phys. Rev. Lett. **114**, 142301 (2015), arXiv:1411.7931 [nucl-ex] .

[50] D. Zhang (STAR), Nucl. Phys. A **1005**, 121825 (2021), arXiv:2002.10677 [nucl-ex] .

[51] M. S. Abdallah *et al.* (STAR), Phys. Rev. Lett. **128**, 202303 (2022), arXiv:2112.00240 [nucl-ex] .

[52] R. V. Gavai and S. Gupta, Phys. Lett. B **696**, 459 (2011), arXiv:1001.3796 [hep-lat] .

[53] M. S. Abdallah *et al.* (STAR), (2022), arXiv:2209.08058 [nucl-ex] .

[54] K.-J. Sun, L.-W. Chen, C. M. Ko, and Z. Xu, Phys. Lett. B **774**, 103 (2017), arXiv:1702.07620 [nucl-th] .

[55] K.-J. Sun, L.-W. Chen, C. M. Ko, J. Pu, and Z. Xu, Phys. Lett. B **781**, 499 (2018), arXiv:1801.09382 [nucl-th] .

[56] N. G. Antoniou, Y. F. Contoyiannis, F. K. Diakonos, A. I. Karanikas, and C. N. Ktorides, Nucl. Phys. A **693**, 799 (2001), arXiv:hep-ph/0012164 .

[57] A. Bialas and R. B. Peschanski, Nucl. Phys. B **273**, 703 (1986).

[58] A. S. K. N. G. Antoniou, F. K. Diakonos and K. S. Kousouris, Phys. Rev. Lett. **97**, 032002 (2006).

[59] N. G. Antoniou, F. K. Diakonos, X. N. Maintas, and C. E. Tsagkarakis, Phys. Rev. D **97**, 034015 (2018), arXiv:1705.09124 [hep-ph] .

[60] T. Anticic *et al.* (NA49), Phys. Rev. C **81**, 064907 (2010), arXiv:0912.4198 [nucl-ex] .

[61] J. Wu, Y. Lin, and Y. W. Li, Zhiming, Phys. Lett. B **801**, 135186 (2020), arXiv:1901.11193 [nucl-th] .

[62] E. A. De Wolf, I. M. Dremin, and W. Kittel, Phys. Rept. **270**, 1 (1996).

[63] A. Bialas and R. C. Hwa, Phys. Lett. B **253**, 436 (1991).

[64] H. Satz, Nucl. Phys. B **326**, 613 (1989).

[65] T. Anticic *et al.* (NA49), Eur. Phys. J. C **75**, 587 (2015), arXiv:1208.5292 [nucl-ex] .

[66] A. Bialas and R. B. Peschanski, Nucl. Phys. B **308**, 857 (1988).

[67] N. G. Antoniou, Y. F. Contoyiannis, F. K. Diakonos, and G. Mavromanolakis, Nucl. Phys. A **761**, 149 (2005), arXiv:hep-ph/0505185 .

[68] N. G. Antoniou and F. K. Diakonos, J. Phys. G **46**, 035101 (2019), arXiv:1802.05857 [hep-ph] .

[69] R. C. Hwa and M. T. Nazirov, Phys. Rev. Lett. **69**, 741 (1992).

[70] R. C. Hwa, Phys. Rev. D **47**, 2773 (1993).

[71] W. Ochs and J. Wosiek, Phys. Lett. B **214**, 617 (1988).

[72] W. Ochs, Z. Phys. C **50**, 339 (1991).

[73] R. C. Hwa and C. B. Yang, Phys. Rev. C **85**, 044914 (2012), arXiv:1111.6651 [nucl-th] .

[74] A. Kamal, N. Ahmad, and M. M. Khan, Acta Phys. Polon. B **46**, 1549 (2015).

[75] Z. Cao, Y. Gao, and R. C. Hwa, Z. Phys. C **72**, 661 (1996), arXiv:nucl-th/9601011 .

[76] S. Bhattacharyya, Eur. Phys. J. Plus **136**, 471 (2021).

[77] Y.-L. Xie, G. Chen, J.-L. Wang, Z.-H. Liu, and M.-J. Wang, Nucl. Phys. A **920**, 33 (2013), arXiv:1303.2183 [nucl-th] .

[78] M. Maćkowiak-Pawłowska (for the NA61/SHINE Collaboration), Nucl. Phys. A **1005**, 121753 (2021), arXiv:2002.04847 [nucl-ex] .

[79] T. Czopowicz (NA61/SHINE), PoS **CPOD2021**, 039 (2022).

[80] M. Kuich (NA61/SHINE), EPJ Web Conf. **259**, 01001 (2022), arXiv:2112.07987 [nucl-ex] .

[81] P. Li *et al.*, Phys. Lett. B **818**, 136393 (2021), arXiv:2104.08483 [nucl-th] .

[82] Q. Li, M. Bleicher, and H. Stocker, Phys. Lett. B **659**, 525 (2008), arXiv:0709.1409 [nucl-th] .

[83] D. Prokhorova and N. Davis (NA61/SHINE), Universe **5**, 103 (2019).

[84] Z. Li, Mod. Phys. Lett. A **37**, 2230009 (2022), arXiv:2203.01490 [nucl-th] .

[85] S. Gope and B. Bhattacharjee, Eur. Phys. J. A **57**, 44 (2021), arXiv:2008.01943 [nucl-th] .

[86] H. Petersen, J. Steinheimer, G. Burau, M. Bleicher, and H. Stöcker, Phys. Rev. C **78**, 044901 (2008), arXiv:0806.1695 [nucl-th] .

[87] J. Wu, Y. Lin, Z. Li, X. Luo, and Y. Wu, Phys. Rev. C **104**, 034902 (2021), arXiv:2104.11524 [nucl-th] .

[88] W. Ochs, Z. Phys. C **50**, 339 (1991).

[89] A. Bialas and M. Gazdzicki, Phys. Lett. B **252**, 483 (1990).

[90] A. Bzdak and V. Koch, Phys. Rev. C **91**, 027901 (2015), arXiv:1312.4574 [nucl-th] .

[91] V. Vovchenko and V. Koch, Nucl. Phys. A **1010**, 122179 (2021), arXiv:2101.02182 [nucl-th] .

[92] M. Abdallah *et al.* (STAR), Phys. Rev. Lett. **127**, 262301 (2021), arXiv:2105.14698 [nucl-ex] .

[93] X. Luo, Phys. Rev. C **91**, 034907 (2015), arXiv:1410.3914 [physics.data-an] .

[94] J. Adamczewski-Musch *et al.* (HADES), Phys. Rev. C **102**, 024914 (2020), arXiv:2002.08701 [nucl-ex] .

[95] BNL Relativistic Heavy Ion Collider (RHIC). https://www.bnl.gov/rhic/.

[96] M. Harrison, T. Ludlam, and S. Ozaki, Nucl. Instrum. Meth. A **499**, 235 (2003).

[97] Picture of STAR detector. https://drupal.star.bnl.gov/STAR/public/img/.

[98] K. H. Ackermann *et al.* (STAR), Nucl. Instrum. Meth. A **499**, 624 (2003).

[99] M. Anderson *et al.*, Nucl. Instrum. Meth. A **499**, 659 (2003), arXiv:nucl-ex/0301015 .

[100] M. Shao, O. Y. Barannikova, X. Dong, Y. Fisyak, L. Ruan, P. Sorensen, and Z. Xu, Nucl. Instrum. Meth. A **558**, 419 (2006), arXiv:nucl-ex/0505026 .

[101] The STAR TOF Collaboration, proposal for a large area time of flight system for STAR, https://www.star.bnl.gov/public/tof/publications/TOF_20040524.pdf.

[102] Y. Zhang, Y. Huang, T. Nonaka, and X. Luo, Nucl. Instrum. Meth. A **1026**, 166246 (2022), arXiv:2108.10134 [physics.data-an] .

[103] M. L. Miller, K. Reygers, S. J. Sanders, and P. Steinberg, Ann. Rev. Nucl. Part. Sci. **57**, 205 (2007), arXiv:nucl-ex/0701025 .

[104] L. Adamczyk *et al.* (STAR), Phys. Rev. Lett. **113**, 092301 (2014), arXiv:1402.1558 [nucl-ex] .

[105] S. Bhattacharyya, Eur. Phys. J. Plus **136**, 471 (2021).

[106] M. Bleicher *et al.*, J. Phys. G **25**, 1859 (1999), arXiv:hep-ph/9909407 .

[107] S. A. Bass *et al.*, Prog. Part. Nucl. Phys. **41**, 255 (1998), arXiv:nucl-th/9803035 .

[108] H. Petersen, J. Steinheimer, G. Burau, M. Bleicher, and H. Stöcker, Phys. Rev. C **78**, 044901 (2008), arXiv:0806.1695 [nucl-th] .

[109] Q. Li and M. Bleicher, J. Phys. G **36**, 015111 (2009), arXiv:0808.3457 [nucl-th] .

[110] M. J. Bleicher, S. A. Bass, L. V. Bravina, W. Greiner, S. Soff, H. Stoecker, N. Xu, and E. E. Zabrodin, Phys. Rev. C **62**, 024904 (2000), arXiv:hep-ph/9911420 .

[111] G. Burau, G. Graf, H. Petersen, and M. Bleicher, EPJ Web Conf. **13**, 06002 (2011).

[112] E. L. Bratkovskaya, M. Bleicher, M. Reiter, S. Soff, H. Stoecker, M. van Leeuwen, S. A. Bass, and W. Cassing, Phys. Rev. C **69**, 054907 (2004), arXiv:nucl-th/0402026 .

[113] H. Petersen, M. Bleicher, S. A. Bass, and H. Stocker (2008) arXiv:0805.0567 [hep-ph] .

[114] B. Efron and R. Tibshirani, Statist. Sci. **1**, 54 (1986).

[115] S. Samanta, T. Czopowicz, and M. Gazdzicki, J. Phys. G **48**, 105106 (2021), arXiv:2105.01763 [nucl-th] .

[116] N. G. Antoniou *et al.*, Nucl. Phys. A **1003**, 122018 (2020), arXiv:2004.12133 [nucl-th] .

[117] P. A. Alemany and D. H. Zanette, Phys. Rev. E **49**, R956 (1994).

[118] A. Adare *et al.* (PHENIX), Phys. Rev. C **97**, 064911 (2018), arXiv:1709.05649 [nucl-ex] .

[119] D. Zhang (STAR), Nucl. Phys. A **1005**, 121825 (2021), arXiv:2002.10677 [nucl-ex] .

[120] P. Li, Y. Wang, J. Steinheimer, Q. Li, and H. Zhang, Phys. Lett. B **818**, 136393 (2021), arXiv:2104.08483 [nucl-th] .

[121] P. Sarma and B. Bhattacharjee, Phys. Rev. C **99**, 034901 (2019), arXiv:1902.09124 [hep-ph] .

[122] S. Gope and B. Bhattacharjee, Eur. Phys. J. A **57**, 44 (2021), arXiv:2008.01943 [nucl-th] .

[123] S. Ahmad, M. M. Khan, S. Khan, A. Khatun, and M. Irfan, Int. J. Mod. Phys. E **23**, 1450065 (2014), arXiv:1510.03176 [nucl-ex] .

[124] N. Hussain and B. Bhattacharjee, Phys. Rev. C **96**, 024903 (2017), arXiv:1709.02660 [nucl-th] .

[125] J. Wu, Z. Li, X. Luo, M. Xu, and Y. Wu, Phys. Rev. C **106**, 054905 (2022), arXiv:2209.07135 [nucl-th] .

[126] Y. Huang, L.-G. Pang, X. Luo, and X.-N. Wang, Phys. Lett. B **827**, 137001 (2022), arXiv:2107.11828 [nucl-th] .

[127] R. V. Poberezhnyuk, O. Savchuk, M. I. Gorenstein, V. Vovchenko, K. Taradiy, V. V. Begun, L. Satarov, J. Steinheimer, and H. Stoecker, Phys. Rev. C **102**, 024908 (2020), arXiv:2004.14358 [hep-ph] .

[128] B. Berdnikov and K. Rajagopal, Phys. Rev. D **61**, 105017 (2000), arXiv:hep-ph/9912274 .

[129] A. Bzdak, V. Koch, and V. Skokov, Phys. Rev. C **87**, 014901 (2013), arXiv:1203.4529 [hep-ph] .

[130] Y. Zhang, S. He, H. Liu, Z. Yang, and X. Luo, Phys. Rev. C **101**, 034909 (2020), arXiv:1905.01095 [nucl-ex] .

[131] B. Ling and M. A. Stephanov, Phys. Rev. C **93**, 034915 (2016), arXiv:1512.09125 [nucl-th] .

List of Figures

List of Tables

Appendix: 论文中文简介

QCD 相结构的研究是国际高能核物理领域的前沿和热门课题。量子色动力学 (Quantum Chromodynamics，QCD) 是描述夸克/胶子之间强相互作用的基本理论。QCD 理论预言, 在高温和高密度条件下，夸克和胶子将摆脱强相互作用力的束缚，解除禁闭，形成由自由夸克和胶子组成的新物质形态——夸克胶子等离子体（QGP）。现代物理学认为 QGP 广泛存在于宇宙的最早期，而在现今的世界中，科学家预期通过相对论重离子碰撞实验来产生 QGP。21 世纪初，BNL 相对论重离子对撞机（RHIC）和 CERN 大型强子对撞机（LHC）实验，都已经发现 QGP 物质存在的信号。随着 QGP 的发现，科学家一直在探索 QGP 新物质到普通强子物质的相变及其相结构。强相互作用物质的相图（QCD 相图），通常用温度（T）与重子化学势（μ_B）的二维图来描述。基于 QCD 理论的模型预测，在高重子化学势和低温条件下，QGP 相到强子相的转变属于一级相变，并且在一级相变边线存在一个终结点，即 QCD 临界点。目前，在全球范围内，多个重大科学实验都在研究 QCD 相结构和寻找可能存在的 QCD 临界点，特别是 RHIC-STAR 能量扫描实验。理论上认为，如果重离子碰撞系统在接近或者处于临界点时，将会出现很强的密度涨落，间歇分析是寻找和观察这种密度涨落的分析方法。Ising-QCD 理论认为，重离子碰撞系统达到临界条件时，将会在动量空间中出现很强的密度涨落。它表现为一种间歇现象，即在相空间小区域（单元）内，物质的密度分布出现大的起伏。因此间歇可以是寻找 QCD 临界点的特征信号之一。在实验上，我们可以用阶乘矩来测量碰撞系统产生的密度涨落，即它的表现形式——间歇。如果碰撞系统存在着间歇，得到的阶乘矩将表现出幂律行为，或者标度行为。从 2010 年以来，位于 CERN 的 NA49 和 NA61/SHINE 合作组已经开展不同能量以及不同种类的重离子碰撞实验，通过分析

重离子碰撞产生的间歇来寻找 QCD 临界点。同时，模型方面的分析也已经开展，比如，当把强子势机制加入到 UrQMD（超相对论量子动力学）模型后，该模型的 Ar+Sc 体系表现出间歇行为。

在本篇论文中，我们首次测量了 RHIC-STAR 重离子碰撞实验中的间歇，得到观测量和碰撞能量的依赖关系，尝试在实验上寻找到 QCD 临界点。同时，我们通过临界蒙特卡洛（CMC）模型研究重离子碰撞中的间歇的性质，和通过 UrQMD 模型来研究非临界现象所引起的涨落对间歇的影响。最后我们结合 UrQMD 和 CMC 两个模型来解释 RHIC-STAR 实验上测量到的结果。

该论文由以下 7 个章节构成：

第一章，我们介绍论文的研究背景、研究动机和分析方法，以及分析中用到的观测量。

研究背景和动机: 浩瀚的宇宙总是让人充满疑惑，对此，科学家们一直在探索宇宙的最基本组成和运行原理。目前，标准模型是最好描述构成物质世界的基本粒子和基本相互作用的理论。它囊括了三种基本相互作用：强相互作用，弱相互作用，电磁相互作用，以及基本粒子：传递相互作用的粒子，六种夸克，六种轻子，希格斯玻色子。夸克是目前所知的组成物质的最小单元，比如，两个上夸克和一个下夸克组成质子。量子色动力学（QCD）是描述夸克胶子之间强相互作用的标准动力学理论。在量子色动力学中，夸克具有三种不同的色荷，通常称为：红色、蓝色与绿色；反夸克亦具有三种不同颜色的反色荷。类似于带电粒子间的电磁相互作用是通过交换光子来实现，夸克之间的强相互作用是通过交换具有色荷的胶子来实现。

量子力学有两大主要特征：渐进自由和色禁闭。夸克-胶子之间的非阿尔法相互作用具有渐近自由的性质，即在能量尺度变得任意大的时候，或者夸克彼此很靠近时，它们之间的强相互作用非常弱，就像是自由粒子一样。反之，当夸克之间彼此分开时，强相互作用将迅速增强。色禁闭是指带不同颜色的夸克受到被称为色荷的强力的束缚，形成带色中性的强子，并且不能从核子中单独地剥离出来。由于色禁闭和渐进自由，夸克是被禁闭在粒子内部的，自然界中我们观测不到自由的夸克。然而，理论物理学家认为，在宇宙大爆炸的最初期，物质的温度和密度都很高，使得夸克和胶子处于解禁闭状态。此时，夸克和胶子在较大的尺度内自由运动，形成了一种新的物质形态，即夸

克-胶子等离子体 (QGP)。然而，这种状态只存在很短时间，随着宇宙体系迅速膨胀冷却，夸克在短时间内迅速结合形成强子，物质密度从密到稀地演化，最终形成如今的宇宙。

QCD 理论预言，在高温高密度的极端条件下，夸克和胶子将摆脱强相互作用力的束缚，从核子中脱离出来，形成由自由夸克和胶子组成的 QGP。上世纪 70 年代，李政道等科学家提出在实验室通过巨型粒子对撞机来产生 QGP。加速器将两束带电重离子（重于 α 能用来加速的原子核）加速到接近光速，之后发生碰撞，在极短的时间内创造出高温高密度的物理环境，改变真空的性质，从而形成 QGP。比如，本世纪初，美国布鲁克海文国家实验室上的相对论对撞机（RHIC）加速金元素离子到质心能量 $\sqrt{s_{\mathrm{NN}}}$ = 200 GeV 之后对撞，制造出温度高达 4 万亿摄氏度的火球，也称为小爆炸（Little Bang)。实验室中相对论重离子碰撞演化过程如图 1.4 所示，首先，我们加速两个背向运动的重离子，使它们接近光速。由于洛伦兹效应，这时的重离子会沿着运动方向收缩而变成一个圆盘状。之后，两个圆盘在极短时间内相互穿越，碰撞，产生的能量将在沉积在一个原子核大小的空间内，达到了高温高密的物理环境，形成火球，即 QGP。接着，由于存在动能和压力梯度，火球会迅速膨胀冷却。随着体系的温度降到临界温度以下，夸克和胶子会重新结合成强子，发生 QGP 相到强子相的相变。最后，强子将经历化学冻结和动力学冻结，且在电磁场作用下，飞向探测器。寿命较长且稳定的粒子将打到探测器上，它们的径迹将被记录。

自从发现 QGP 以来, 科学家一直在研究 QGP 相到强子物质相的相变，其中包括相变是如何进行的，什么条件下可以发生相变，该相变是否属于一级相变和是否存在临界点。如图 1.6 所示，QCD 的相结构图通常用温度（T）和重子化学势（μ_B）的二维图来表示, 改变重离子对撞能量相当于改变体系的 T 和 μ_B。在图 1.6 中，黄色区域表示 QGP 相，而蓝色区域表示强子相。基于第一性原理出发的格点 QCD 表明，在低重子化学式和高温度时，QGP 相和强子物质相的转变是平滑过渡。同时，基于 QCD 理论的模型预测，在高重子化学势和低温条件下，QGP 相到强子相的转变属于一级相变，如图中黑色的实线。该黑色实线存在一个终点，即一级相变边界的终结点，为 QCD 临界点。确认 QCD 临界点是探索核物质相结构的里程碑，具有重要科学意义。在世界范围内，很多重大科学实验都在寻找可能存在的 QCD 临界点，比如正在运行的美国 RHIC-STAR 实

验，欧洲核子中心 NA61/SHINE 实验，以及即将开始运行的德国 FAIR-CBM 实验，俄罗斯 NICA-MPD 实验和中国 CEE 实验。

当改变重离子碰撞能量，核-核碰撞实验形成的热核物质的化学冻结温度和重子化学势也将发生改变。对碰撞能量进行扫描，当碰撞体系穿过临界区域时，理论上认为临界点的一个特征信号是观测量的非单调能量依赖。比如，一个重要的观测量是守恒荷分布的高阶矩。在 QCD 临界点附近，体系的关联长度发散，而高阶累积矩对关联长度敏感。图 1.8 显示 RHIC-STAR 实验测量到的四阶高阶矩 $\kappa\sigma^2$ 和碰撞能量的依赖关系。我们可见，$\kappa\sigma^2$ 表现出明显的非单调能量依赖，并在 $\sqrt{s_{\rm NN}}$ = 19.6GeV 附近有一个最低点，暗示碰撞产生的系统可能穿过了临界区。另外一个重要的观测量是轻核的产额，当体系位于临界点时，它的核子数密度涨落会增大，轻核的产额随之受到影响。图 1.9 显示的是，来自 STAR 实验的，轻核产额比（$N_t \times N_p/N_d^2$）随着能量的变化关系。$N_t \times N_p/N_d^2$ 也显示出明显的非单调能量依赖，并且在 $\sqrt{s_{\rm NN}}$ = 20-27GeV 有一个峰。这一结果说明该区域的密度涨落可能收到临界区的影响，从而明显增强。在本论文的间歇分析中，我们将探讨间歇的观测量是否也表现出非单调能量依赖。

间歇分析和对应的观测量:

理论上认为，临界间歇是 QCD 临界点的特征信号之一。重离子碰撞系统在接近或者处于临界点时，将会出现很强的密度涨落。通过寻找和研究重离子碰撞产生的密度涨落，我们可以确定 QCD 相图上临界点的位置，而间歇分析是寻找和观察密度涨落的一种方法。基于三维 Ising-QCD 的理论，碰撞系统达到临界条件时，其动量空间中的密度-密度函数将具有一种幂律，或者自相似的结构，这使得动量空间里出现很强的密度涨落，如图 1.10所示。这种密度涨落表现为一种间歇现象，即在相空间小区域（单元）内，物质的密度分布出现大的起伏。实验上，我们可以用阶乘矩来测量碰撞系统产生的密度涨落，即它的表现形式-间歇。根据粒子多重数在相空间的分布，我们可以计算得到粒子的阶乘矩, SFM 或者 $F_q(M)$, 计算公式如下：

$$F_q(M) = \frac{\langle \frac{1}{M^D}\sum_{i=1}^{M^D} n_i(n_i-1)\cdots(n_i-q+1)\rangle}{\langle \frac{1}{M^D}\sum_{i=1}^{M^D} n_i\rangle^q}, \tag{7.1}$$

这里，D 维相空间的各个维度都均分成 M 个格子，M^D 则是整个相空间被均分的

格子数。n_i 是位于第 i 个格子的粒子多重数, $\langle\rangle$ 代表对所有事件的平均。例如，横动量空间（p_x, p_y）被分割成 M^2 个同等大小的格子，且阶数 $q = 2, F_q(M)$ 的计算公式则简写为：$F_2(M) = \frac{\langle \frac{1}{M^2}\sum_{i=1}^{M^2} n_i(n_i-1)\rangle}{\langle \frac{1}{M^2}\sum_{i=1}^{M^2} n_i\rangle^2}$。

如果碰撞体系存在着间歇，$F_q(M)$ 和 M^D 之间将满足幂律（标度）行为：$F_q(M) \propto (M^D)^{\phi_q}, M \gg 1$，也就是 $F_q(M)/M$ 标度。其中，ϕ_q 是间歇指数，它的值越大，间歇就越强。Ising-QCD 理论预言，对于处于临界点的体系，质子 (*p*) 的临界间歇指数为 $\phi_q^c = \frac{5\times(q-1)}{6}, \pi$ 介子的临界间歇指数为 $\phi_q^c = \frac{2\times(q-1)}{3}$。然而，$F_q(M)/M$ 标度行为，可能在体系的演化过程中被减弱，或者稀释掉，也就是在体系演化完成后，实验上不能观察到 $F_q(M)$ 和 M^2 之间的幂律关系。

另外一种，我们所期待的标度行为是：$F_q(M) \propto F_2(M)^{\beta_q}, M \gg 1$, 即高阶的 $F_q(M)$ 和二阶的 $F_2(M)$ 之间满足幂律行为。这种标度行为被称为 $F_q(M)/F_2(M)$ 标度。根据金兹堡-朗道理论，即使 $F_q(M)/M$ 标度行为在体系的演化过程中被稀释掉，$F_q(M)/F_2(M)$ 标度行为也能保留下来并且可以观察得到。最重要的是，我们可以通过标度指数（ν）：$\beta_q \propto (q-1)^\nu$，来衡量各阶的 $F_q(M)/F_2(M)$ 标度行为，表示间歇强度的大小。金兹堡-朗道理论预测，当体系处于 QCD 临界点时，标度指数的临界值等于 1.30，而二维 Ising 理论预测的临界值为 1.0。值得注意的是，这个数值是对整个相空间而言，然而，在实验中我们只能测量得到有限空间内的粒子多重数分布。

间歇指数和标度指数，它们和碰撞能量之间的依赖关系可以用来寻找 QCD 临界点。2010 年以来，位于 CERN 的 NA49 和 NA61/SHINE 合作组已经开展了不同能量以及不同种类的重离子碰撞实验，通过间歇分析的方法来寻找 QCD 临界点。在能量为 $\sqrt{s_{\rm NN}}$ = 17.3 GeV 的 Si+Si 重离子碰撞体系中，质子的 $F_2(M)$ 和 M 之间满足标度行为，并且 $\phi_2 = 0.96 \pm 0.16$, 说明该体系观察到很强的间歇现象。本论文将分析 RHIC-STAR 实验 Au+Au 碰撞中的间歇，通过寻找临界间歇来尝试确定 QCD 临界点的位置。

第二章，我们介绍间歇分析中扣除背景和效率修正的方法。

使用混合事件和累积变量的方法来扣除背景。碰撞产生的系统会存在大量的背景，即存在与临界点无关的非临界背景涨落。这些背景来自于重子数守恒、非平衡效应、体积涨落、末态强子衰变和强子散射、接收度等非临界物理。来自背景的贡献将在一定程度上改变 SFMs 的测量值，因此，在分析中，我们一定要扣除背景对 SFMs 的贡献，

而混合事件是扣除背景的一种有效的方法。为了构造混合事件，我们彻底打乱真实事件的粒子分布。混合事件的粒子多重数和真实事件的一样，但混合事件里的粒子来源于不同的真实事件，也就是混合事件中没有任何两个粒子来自于同一的真实事件。之后，我们计算出混合事件的 SFMs。那么扣除背景后的 SFMs 为真实事件的 SFMs 减去混合事件的 SFMs, 即：$\Delta F_q(M) = F_q^{data}(M) - F_q^{mix}(M)$。该方法已经使用在 NA49 和 NA61 实验的间歇分析，我们也将此方法运用到 STAR 实验数据的间歇分析。

另外一种扣除背景的方法是累积变量。累积变量 (X) 是对概率密度函数 $[\rho(x)]$ 进行积分，得到一个描述随机变量 x 概率分布的变量，即：$X = [\int_{x_{min}}^{x} \rho(x)dx]/[\int_{x_{min}}^{x_{max}} \rho(x)dx]$。为了验证累积变量方法也可以扣除背景，我们在具有临界涨落的事件中不断加入来自背景的涨落。这里的背景可由高斯分布来模拟。我们发现，当加入 95% 的背景时，也就是临界信号只有 5% 时，$F_q(M)/M$ 标度行为已不再存在。但是，运用累积变量方法之后，$F_q(M)/M$ 标度从新恢复，而且间歇指数几乎相等于原来的真实值，具体结果如图 2.3 所示。

使用逐格子的方法来效率修正。在高能物理实验中，探测器的效率是有限的，并不是 100%。由于有些粒子并不能被探测器记录到，探测到的粒子多重数要比真实的要少。然而，SFMs 是计算粒子的多重数分布得到，粒子多重数的丢失会导致测得的 SFMs 不同于真实的 SFMs。因此，在实验测量中，我们要使用适当的效率修正方法，对测量得到 SFMs 进行修正，得到 SFMs 的真实值。通常认为，探测器的效率（ε）是服从二项分布的，那么矩的效率修正的公式为：$f_q^{corrected} = f_q^{measured}/\epsilon^q = \langle n(n-1)...(n-q+1)\rangle/\epsilon^q$。将该公式运用到阶乘矩的计算中，即得到阶乘矩对效率的修正公式，即是公式 (2.3)。我们通过 UrQMD 模型来验证公式 (2.3)的有效性。我们根据 STAR 实验上 TPC 和 TOF 探测器的效率，随机丢掉 UrQMD 事件中的部分粒子，从而把探测器的效率加入到模型产生的事件中。我们发现，加入探测效率后，$F_q(M)$ 的数值发生了明显的变化。但是，采用公式 (2.3)进行效率修正后，修正的 $F_q(M)$ 和真实的 $F_q(M)$ 基本完全重合。这个结果说明了公式 (2.3)，即逐格子的方法，可以很好修正探测效率对 SFMs 的影响。

第三和第四章，我们主要介绍 RHIC-STAR 实验装置和对实验数据的筛选。

RHIC-STAR 相对论重离子对撞机：相对论重离子对撞机（Relativistic Heavy Ion Collider, RHIC) 位于美国长岛的布鲁克海文国家实验室 (BNL)。它的主体是周长为 3.8

km 的两个加速圆环，其中一束束流按顺时针方向进入“蓝环”，另一束束流按逆时针方向进入“黄环”。在圆环上有 4 个交汇点碰撞，这 4 个碰撞点上分别建造了 4 台复杂且精密的粒子探测器。STAR 探测器 (solenoidal tracker at RHIC) 位于 RHIC 圆环上的 6 点钟方向。目前，STAR 探测器是 RHIC 唯一仍在运行，并且专门用来研究 QGP 物质和 QCD 相变物理的探测器。STAR 探测器主要部件包括时间投影室（TPC）、硅顶点探测器（VPD）、飞行时间探测器（TOF）、电磁量能器（BEMC）等，其中，TPC 是 STAR 探测器的最主要的径迹探测器。TPC 是一个桶状结构的气体漂移室，长 4.2m, 直径为 4m。它的磁场强度为 $B = 0.5T$, 能够测量带电粒子的横动量（p_T）为 $0.15 < p_T < 30$ GeV/c, 而且它具有较大中心快度区间（$|\eta| < 1$）和全方位角接收度（2π）。TPC 记录了粒子的径迹，测量粒子的动量，并且通过测量粒子在 TPC 气体中的电离能损（dE/dx）对粒子进行鉴别。为了进一步提高 STAR 探测器的粒子鉴别能力，TOF 被安装在 TPC 的外围。TOF 主要由桶部的 TOF 板以及顶点位置探测器组成，它们分别测量粒子到达 TOF 探测器的时间和碰撞发生的时间。TOF 提供了粒子的飞行时间，再结合 TPC 提供的动量信息，可以得到粒子的速度和质量。通过粒子的质量，我们可以对粒子进行鉴别。结合 TPC 和 TOF，STAR 谱仪的 π 介子和 K 介子分辨达到到 1.8 GeV/c，质子的鉴别达到 3 GeV/c。

STAR 实验数据的筛选：在 2010—2017 年，RHIC 进行了第一阶段重离子碰撞能量扫描 (Beam Energy Scan-I, BES-I), 采集了 Au+Au 碰撞能量（$\sqrt{s_{\rm NN}}$）有 9 个：7.7，11.5, 14.5, 19.6, 27, 39, 54.4, 62.4, 200 GeV。在分析中，我们需要保证数据集的质量，把一些不好的数据筛选出去。首先，我们只选择距离中心碰撞顶点较近的事件。其次，我们排除掉堆积事件（Pile-up events），这些事件是两个或者多个碰撞事件被探测器当作成了一个事件来处理。最后，我们选择事件的常用物理量，比如 p_T, η, V_z, V_r, DCA 等，来挑选好的采集单元 (good run)。当某一单元的物理量远离所有单元的平均值 (大于 3 个 σ 的范围), 就被判断为坏的单元 (bad run), 它们将不用于数据的分析中。中心度的定义是通过测量末态带电粒子在中心赝快度区域 $0.5 < |\eta| < 1.0$ 的个数来确定的, 而 $|\eta| < 0.5$ 的带电粒子将用于 SFMs 的计算中，从而消除自关联对观测量的影响。经过筛选，9 个能量的事件统计量分别为：3.3, 6.8 13.1, 16.2, 32.2, 89.3, 441.7, 46.7, 236.0 $\times 10^6$。

第五和第六章是我们对 STAR 实验和模型结果的讨论。

STAR 实验中的间歇分析结果： 我们计算横动量空间（p_x, p_y）中, 中心赝快度区间（$|\eta| < 0.5$）下的带电强子的阶乘矩，其中，带电强子包括质子（p), 反质子（$\bar{p}$)，K 介子（$K^{\pm}$)，π 介子（$\pi^{\pm}$)，并且横动量空间的范围为 $[-2 < p_x < 2\text{GeV/c}] \otimes [-2 < p_y < 2\text{GeV/c}]$。在目前的统计量下, SFMs 的阶数可以计算到六阶 ($q = 2-6$), 格式数可以计算到 100 ($M = 1-100$)。图 5.3 显示的是, 最中心 Au+Au 碰撞 (0-5%) 下的, 经过效率修正的 $F_q^{data}(M)$ 和 $F_q^{mix}(M)$, 以及它们随着 M^2 变化的函数关系。可以看到，当 M^2 比较大时（$M^2 > 1000$)，$F_q^{data}(M)$ 明显大于 $F_q^{mix}(M)$，这说明 Au+Au 碰撞体系存在着密度涨落。图 5.6 中显示了, 扣除背景后的 SFMs, 即: $\Delta F_q(M) = F_q^{data}(M) - F_q^{mix}(M)$, 和 M^2 的函数关系。我们发现在最中心碰撞下，$\Delta F_q(M)$ 随着 M^2 的增大而增大，但是逐渐趋于饱和。因此，幂律：$\Delta F_q(M) \propto (M^2)^{\phi_q}$ 并不能满足，也就是体系不显示 $\Delta F_q(M)/M$ 标度行为，从而我们不能计算得到 ϕ_q。

虽然 Au+Au 碰撞体系不显示 $\Delta F_q(M)/M$ 标度行为, 但仍可能显示 $\Delta F_q(M)/\Delta F_2(M)$ 标度行为。图 5.15 显示的是，高阶的 $\Delta F_q(M)$ 和二阶的 $\Delta F_2(M)$ 的函数关系。我们发现 $\Delta F_q(M)$ 和 $\Delta F_2(M)$ 之间满足严格的幂律关系：$\Delta F_q(M) \propto F_2(M)^{\beta_q}$, 即我们所期待的 $\Delta F_q(M)/\Delta F_2(M)$ 标度。我们在所有能量，即 $\sqrt{s_{_{NN}}}$ = 7.7-200GeV，中都观察到 $\Delta F_q(M)/\Delta F_2(M)$ 标度，这是因为经历一级相变和平滑过渡的体系都演化出一定的密度涨落。由于体系表现出了 $\Delta F_q(M)/\Delta F_2(M)$ 标度，我们可以计算得到 β_q。在间歇分析中, 我们只考虑 M 比较大的 $\Delta F_q(M)$。因此，在计算 β_q 过程中，我们只拟合在 $M^2 \geq 900$ 区间的 $\Delta F_q(M)$。图 5.15 中的黑色斜线表示了拟合的结果，该斜线的斜率即为 β_q 的数值大小。此外，由于 $\Delta F_q(M)/\Delta F_2(M)$ 标度足够好，β_q 并不随着拟合区间的变化而明显变化。

在图 5.23(a) 中，我们显示了所有能量下，最中心碰撞（0-5%）中，β_q 和 q 的函数关系。β_q 和 q 之间满足严格的幂律关系：$\beta_q \propto (q-1)^{\nu}$，这符合理论的预测。接下来，我们可以计算得到 Au+Au 碰撞体系中的 ν。图 5.23(a) 中的斜线表示了拟合的结果，它的斜率即是 ν 值的大小。图 5.23(b) 显示的是 $\sqrt{s_{_{NN}}}$ = 19.6-200 GeV 下，ν 的中心度依赖关系。可以看到的是，从半中心 (30-40%) 到最中心碰撞（0-5%)，ν 的值一直在变小。此外，由于 $\sqrt{s_{_{NN}}}$ = 7.7-14.5 GeV 的统计量太小，我们不能计算这三个能量下的 ν 的中心度依赖关系。值得注意的是，ν 的值越大并不说明体系的间歇越强。STAR 实验中观

察到的 ν 的中心度依赖，还需要相关理论来解析。

图 5.25 显示我们最重要的结果，即不同中心度碰撞下，标度指数 (ν) 和碰撞能量 ($\sqrt{s_{\rm NN}}$) 的依赖关系。我们可以看到，在最中心（0-5%）的 Au+Au 碰撞中，标度指数表现出明显的非单调的能量依赖，并且在 $\sqrt{s_{\rm NN}}$ = 27 GeV 左右可能存在最小值。而在半中心（10-40%）碰撞中，ν 并没有随着能量的增大而变化，没有表现出非单调的能量依赖。这一结果说明能量在 $\sqrt{s_{\rm NN}}$ = 20-30 GeV 之间的 Au+Au 碰撞体系经历了特殊的物理机制，有可能是经历了临界区，但是依旧需要更多理论方面的研究来解释和证明。实验测量到的 ν 值要比理论预言的临界值要小，比如来自 2D Ising 理论预测的 1.0 和金兹堡-朗道理论预测的 1.3。这是因为理论预测是相对于整个相空间、所有粒子的 ν，而实验上我们只能测量到有限空间中的 ν，比如我们现在测量到的横动量空间中，接受度为 $|\eta| < 0.5$, $0.2 < p_T < 2.0$ 下的，带电强子的 ν。目前，其它观察量也显示非单调的能量依赖，比如净质子数的峰度（$\kappa\sigma^2$）和直接流（v_1），轻核的产额比（$N_t \times N_p/N_d^2$），ν 的非单调能量依赖类似于这些观测量的结果。由于 UrQMD 模型并没有显示出 $\Delta F_q(M)/\Delta F_2(M)$ 标度，即 UrQMD 模型不能计算得到扣除背景后的 ν。因此，我们还需要一个具有密度涨落的模型来计算出一个基准线，并且和实验的结果比较。

UrQMD 模型和 CMC 模型的间歇分析结果: 超相对论量子动力学 (UrMQD) 模型是一个广泛地用于模拟高能 p+p、p+A 和 A+A 碰撞的强子输运模型，它可以很好模拟 SIS（$\sqrt{s_{\rm NN}} \approx 2$ GeV）到 RHIC 最高能量（$\sqrt{s_{\rm NN}}$ = 200GeV）范围内的重离子碰撞。由于 UrQMD 模型没有包含 QGP 相到强子相的相变，它可以用来研究与临界点无关的背景涨落的干扰。我们使用 UrQMD 模型（3.4 版本）来产生 Au+Au 对撞的事件样本，碰撞的能量有 7 个：$\sqrt{s_{\rm NN}}$ = 7.7，11.5, 19.6, 27, 39, 62.4, 200 GeV，对应的事件统计量为：1.54、1.17、1.15、1.25、1.20、1.30、0.5×10^6。对于质子，所有能量和中心度下，$F_q(M)$ 随着 M^2 的增大而很缓慢地增长，而且没有满足幂律关系。对于带电强子，如图 6.4 所示，所有碰撞能量下，UrQMD 模型的 $F_q(M)^{data}$ 和 $F_q(M)^{mix}$ 基本重合，从而 $\Delta F_q(M)$ 的值基本为零。虽然，高阶的 $F_q(M)^{data}$ 和二阶的 $F_2(M)^{data}$ 之间满足幂律关系，但是使用混合事件方法扣除背景后，UrQMD 并不显示任何的 $\Delta F_q(M)/M$ 和 $\Delta F_q(M)/\Delta F_2(M)$ 标度行为。UrQMD 模型的结果中，没有发现任何的间歇，是由于该模型没有包含任何引起间歇的密度涨落。

我们通过于临界蒙特卡洛（CMC）模型来产生具有临界密度涨落的事件样本。CMC 事件的粒子动量分布由 Levy 函数产生，事件的粒子多重数分布和 UrQMD 事件的一样。如图 6.6 所示，CMC 模型的质子的 $F_q(M)$ 满足很好的幂律行为，而且计算得到的 ϕ_2 和理论预测的一样。图 6.10 显示的带电强子的 $F_q(M)$，可以看到 CMC 模型表现出很好的 $\Delta F_q(M)/M$ 和 $\Delta F_q(M)/\Delta F_2(M)$ 标度行为，而且 CMC 模型的 ν 值和理论预测的基本相等，说明 CMC 模型很好模拟了重离子碰撞中由临界涨落引起的临界间歇。在 CMC 模型中，我们发现粒子的动量关联函数具有自相似性，说明间歇的产生和体系的自相似结构紧密相关。此外，相对涨落系数（Δn）在实验上可通过轻核的产额比计算得到，我们计算 CMC 模型的 Δn，发现它随着 ϕ_q 的增大而明显增大，说明测量体系的密度涨落的两个物理量，Δn 和 ϕ_q，是正比例关系。然而，CMC 只是一个相对简单的模型，它只模拟临界事件的动量信息，而且没有包含重离子碰撞的演化过程和信息。

为了描述 STAR 实验 Au+Au 碰撞中的间歇结果，我们把 CMC 模型和 UrQMD 模型结合起来，即把 CMC 模型的临界密度涨落加入到 UrQMD 模型中，生成混合的 UrQMD+CMC 模型。为此，我们先产生 CMC 事件，这些事件和 UrQMD 事件具有同样的粒子多重数分布和横动量分布，再用 CMC 事件的粒子随机替换掉 UrQMD 的粒子。替换的粒子越多，UrQMD+CMC 事件中 CMC 粒子所占的比例就越大。如图 6.11 和 6.12 所示，UrQMD+CMC 模型表现出明显的 $\Delta F_q(M)/M$ 和 $\Delta F_q(M)/\Delta F_2(M)$ 标度行为。如图 6.13 所示，通过比较 UrQMD+CMC 模型的结果和 STAR 实验数据的结果，我们发现当 UrQMD 事件加入 CMC 模型中的 1-2% 临界涨落时，即信号比例为 1-2% 时，UrQMD+CMC 模型的标度指数的结果和实验测量得到的结果，两者在数值范围内相一致。这个结果和 NA49 合作组的 Si+Si 实验中的 1% 信号比例相符合。

总结和展望： 我们测量和分析了 RHIC 能区下 Au+Au 碰撞中的间歇，主要结论如前面章节所述。从 2019 年到 2021 年，RHIC 已经完成第二阶段的能量扫描，Au+Au 对撞能量点有 $\sqrt{s_{\mathrm{NN}}}$ = 7.7, 9.2, 11.5, 14.5,19.6, 27 GeV。RHIC 也已经采集了更多低能量点的固定靶实验数据，它们的质心能量在 3-7.2 GeV 之间。相比于第一期能量扫描（BSEI），STAR 实验在第二期能量扫描中（BES-II）增加了 iTPC、eTOF、EPD 探测器，探测器的粒子探测效率、粒子鉴别能力、接受度明显提高，事件统计量也比以前提高了 10 倍。这意味着，我们可以在低能、高重子密度区域对粒子的间歇进行高精度的测量，如图 7.2

中红色箭头的范围所示。此外，统计量的大幅提高将减小 $\sqrt{s_{_{\rm NN}}}$ = 7.7-27 GeV 能区内的 ν 的统计误差和系统误差。将来，更高精度的间歇测量将确定 ν 的非单调能量依赖和最低点的能量位置, 从而促进对 QCD 相变和临界点的研究。

Publications and Presentations

Publications:

1. Energy Dependence of Intermittency for Charged Hadrons in Au+Au Collisions at RHIC (STAR), submitted to Physics Letters B, *arXiv:2301.11062* (2023)

2. Probing QCD critical fluctuations from intermittency analysis in relativistic heavy-ion collisions.
   Jin Wu, Yufu Lin, Yuanfang Wu, Zhiming Li, *Physics Letters B* **801**, 135186 (2020)

3. Intermittency of charged particles in the hybrid UrQMD+CMC model at energies available at the BNL Relativistic Heavy Ion Collider.
   Jin Wu, Zhiming Li, Xiaofeng Luo, Mingmei Xu, Yuanfang Wu,
   PHYSICAL REVIEW C **106**, 054905 (2022)

4. Intermittency analysis of proton numbers in heavy-ion collisions at energies available at the BNL Relativistic Heavy Ion Collider.
   Jin Wu, Yufu Lin, Zhiming Li, Xiaofeng Luo, Yuanfang Wu,
   PHYSICAL REVIEW C **104**, 034902 (2021)

5. Measurement of intermittency for charged particlesn in Au+Au at $\sqrt{s_{\mathrm{NN}}}$ = 7.7-200 GeV from STAR.
   Jin Wu (for the STAR Collaboration), *SciPost Phys. Proc* **10**, 041 (2022)

Main Presentations:

1. Measurement of intermittency for charged particlesn in Au+Au at $\sqrt{s_{\rm NN}}$ = 7.7-200 GeV from STAR.
   50th International Symposium on Multiparticle Dynamics (ISMD2021), virtual conference, 12-16 July.

2. Energy Dependence of Intermittency for Charged Hadrons in Au+Au Collisions at RHIC-STAR.
   第十八届全国核物理大会 (2023), 中国. 湖州, 12-16 May.

3. Measurement of intermittency for charged particlesn in Au+Au at $\sqrt{s_{\rm NN}}$ = 7.7-200 GeV from STAR.
   The 14th workshop in the Series of Workshops on QCD Phase Transition and Relativistic Heavy-ion Physics (QPT 2021), 中国. 贵阳, 26-30 July.

致谢

时光匆匆，已经在桂子山求学七个年头了。博士毕业之际，谨以此文致谢所有帮助过我的人。

本篇论文是在吴元芳教授、罗晓峰教授、李治明副教授的指导下完成。

非常感谢我的恩师吴元芳教授、罗晓峰教授、李治明副教授。恩师于我，授我渔鱼，高山景行，师之范者。承蒙老师们的厚爱，我有幸在华中师大粒子所求学和求索，领略科学的魅力和奥妙，看到科学领域中美妙的风景。七年以来，三位导师授业传道，解惑，教导着我，策我前行。本人没有任何天份，读研期间，靠着导师们一直耐心的指导和大力支持，我从一个一无所知的科研小白到顺利博士毕业。读研期间，导师们一步步教我，如何开展课题和处理数据，如何去解决分析中遇到的问题，如何讲报告，如何看文章和写文章等等，做出一定的科研成果需要不少的付出和努力，而这个过程中的每一步，老师们都在支持和帮助着我。导师们对科学的兴趣和热忱，对知识和智慧的追求，一直感染着我。导师们的学识渊博、洞察敏锐、开阔的视野，是我终身奋斗的目标。学生我，衷心祝愿导师们身体健康，工作顺利，万事如意，桃李满天下。

感谢家人至亲，尤其是姐姐们和大哥，这么多年你们支撑着家，照顾着父母，负重前行，让我不必担心家里的事情，安心完成学业。

感谢华师的各位老师，感谢许明梅老师、刘峰老师、施梳苏老师、王亚平老师、庞龙刚老师，感谢他们在科研道路上的指导和帮助。感谢师兄师姐们，感谢赵烨印博士、林裕富博士、张东海博士、杨贞贞博士、兰少位博士，何澍博士、杨鹏博士，在我科研入门的时候，教会我很多知识，分享了很多实用的代码。特别感谢这些年一起经历风雨阳光的好哥们，感谢张定伟博士、张宇博士、兰少位博士、张彪博士、赵松林、刘利

柯。也特别感谢组里的搭档李笑冰博士，科研和工作中配合得默契。也感谢身边的同学们，韩庆飞、傅川博士、杨淑云博士、谢容容博士、刘慧等，一起在粒子所里共同求学、求索。也感谢组里和 427 实验室的小伙伴们，郭冉冉、刘康宁、米柯、綦猷全、沈乾达、周帅、刘佐文、方绍秋、白延欢、樊碧君等，大家一起度过了很多美好时光。

衷心感谢我的导师！感谢我的朋友！感谢组里的小伙伴！感谢我的家人！祝你们永远安康幸福！